

**LIGHT ENHANCEMENTS  
IN  
NANO-STRUCTURED SOLAR CELLS**

Francesco PASTORELLI

INSTITUT FRESNEL – CNRS UMR 7249

UNIVERSITÉ AIX-MARSEILLE

MARSEILLE, FRANCE 2013

ICFO – INSTITUTE DE CIÈNCIES FOTÒNIQUES

UNIVERSITAT POLITÈCNICA DE CATALUNYA

BARCELONA, ESPAÑA 2013





# LIGHT ENHANCEMENTS IN NANO-STRUCTURED SOLAR CELLS

Francesco PASTORELLI

Under the supervision of

Nicolas BONOD

And

Prof. Jordi MARTORELL

submitted this thesis in partial fulfilment

of the requirements for the degree of

DOCTOR

by the

UNIVERSITÉ AIX-MARSEILLE, 2013

and

UNIVERSITAT POLITÈCNICA DE CATALUNYA, 2013



UNIVERSITAT POLITÈCNICA  
DE CATALUNYA  
BARCELONATECH



**THÈSE** de Doctorat

Pour obtenir le grade de **Docteur en Sciences**  
de l'Université Aix-Marseille

**Discipline** : Optique, Photonique et Traitement d'Image

**LIGHT ENHANCEMENTS**  
**IN**  
**NANO-STRUCTURED SOLAR CELLS**

soutenue publiquement en 2013 par

Francesco PASTORELLI

**École Doctorale** : Physique & Sciences de la Matière

Rapporteurs : Prof. Jérôme PLAIN  
Dr. Monica LIRA

Examineurs : Dr. Riccardo SAPIENZA  
Dr. Guillaume DEMÉSY  
Dr. Alberto MARTÍNEZ-OTERO

Directeur de thèse : Dr. Nicolas BONOD

co-Directeur de thèse : Prof. Jordi MARTORELL



## Abstract

In this century some of our main issues are energy shortage and pollution. This work will briefly describe these problems, proposing a plan of action combining energy saving and different sustainable energy sources. Within different types of renewable energy sources, solar energy is the most abundant one. To make solar energy a more sustainable and cost effective technology we focus on enhancing the optical characteristics of thin film solar cells. In this category, organic solar cells are good options for their exiguous amount of material and the low energy needed for the fabrication process. This technology can be lightweight, transparent, flexible and conformal in order to be applied to and integrated in various architectural solutions and consumer electronics. After a study of the physics of such devices and on how to optically enhance their performances, we will show some examples where we theoretically and experimentally collect the solar radiation with optical antennas. We report, for the first time in literature, a nanogap antenna that efficiently couples the light in our active material thin film. Finally, we elaborate on the concept of building integrated photovoltaics introducing some examples of solar façades. Based on our research, we are able to design and fabricate an organic transparent solar cell with a visible transparency above 20% and an optically enhanced photon – electron conversion efficiency remarkably similar to its opaque equivalent.





## Resumen

En el presente siglo, algunas de las prioridades son la escasez de la energía y la contaminación. Este trabajo describirá brevemente estos problemas y propondrá un plan de acción que combina el ahorro energético con diferentes fuentes sostenibles de energía. Dentro de estas fuentes de energía renovables, la energía solar es la más abundante. Con el objetivo de hacer la tecnología solar más sostenible y eficiente económicamente nos concentramos en aumentar las características ópticas en celdas solares de película delgada. Dentro de esta categoría, las celdas solares orgánicas son una buena opción porque su desarrollo requiere bajas cantidades de materiales y su fabricación es de baja energía embebida. Adicionalmente, esta tecnología puede ser liviana, transparente, flexible mecánicamente y modular para ser aplicada e integrada en varias soluciones arquitectónicas y de electrónica de consumo. Luego de estudiar los procesos físicos en tales dispositivos y de determinar las metodologías para aumentar ópticamente sus desempeños, mostraremos algunos ejemplos donde teórica y experimentalmente se colecta la radiación solar mediante antenas ópticas. Se reporta por primera vez, una antena de nanogap que acopla eficientemente la luz en la capa activa de la celda solar. Finalmente, se desarrolla el concepto de tecnología fotovoltaica integrada en edificaciones tras introducir algunos ejemplos de fachadas solares. Basados en nuestra investigación, fue posible diseñar y fabricar una celda solar orgánica transparente cuya transparencia en el rango visible estuvo por encima del 20% y una eficiencia de conversión foton-electron aumentada ópticamente que resulto notoriamente similar a la celda solar orgánica opaca equivalente.



## Résumé

La rareté grandissante des ressources en énergie associée à une augmentation de la pollution font partie des enjeux plus importants de ce siècle. Cette thèse décrira brièvement ces deux problématiques et proposera un plan d'action combinant économie d'énergie et diversité des sources d'énergies renouvelables. Parmi les formes d'énergies renouvelables disponibles, l'énergie solaire est la plus abondante. Pour faire de l'énergie solaire une ressource plus durable et plus rentable économiquement, nous proposons d'amplifier les propriétés optiques de cellules solaires en couches minces. Dans cette catégorie, les cellules solaires organiques représentent un choix pertinent de part la faible quantité de matériau nécessaire ainsi que la faible énergie nécessaire au procédé de fabrication. Cette technologie peut être légère, transparente et flexible de sorte qu'elle peut être utilisée dans différentes solutions architecturales s'adaptant à des produits électroniques pour le grand public. Suivra la théorie sous jacente à ces dispositifs et l'explication de la manière dont leurs performances sont améliorées. Nous présenterons quelques exemples où l'on collecte la radiation solaire avec une antenne optique. Ainsi, nous faisons la toute première démonstration d'une antenne auto-assemblée qui couple efficacement la lumière dans le matériau constituant la couche mince que nous utilisons. Finalement, nous développons le concept de cellules photovoltaïques intégrées en présentant différents cas de façades solaires. Ces travaux nous ont permis de concevoir et de fabriquer une cellule solaire organique transparente avec une transparence dans le visible de 20% et une efficacité de conversion photon-électron améliorée, similaire à une cellule équivalente opaque.



## Riassunto

La difficile reperibilità di risorse energetiche e l'inquinamento sono alcuni dei problemi più importanti di questo secolo. In questo lavoro saranno presentati brevemente questi temi proponendo un piano d'azione che abbinì il risparmio energetico alle differenti fonti di energia rinnovabili. Nell'insieme delle fonti energetiche rinnovabili l'energia solare è senz'altro la più abbondante. Con l'obiettivo di rendere lo sfruttamento di tale energia più sostenibile ed economicamente vantaggioso, ci premuriamo di migliorare le caratteristiche ottiche di celle fotovoltaiche a film sottile. In questa categoria utilizziamo, tra le diverse opzioni, le celle solari organiche in quanto la loro fabbricazione richiede una quantità di materiale minimo e un basso consumo energetico. Inoltre questi tipi di dispositivi possono essere leggeri, trasparenti, flessibili e conformabili alle superfici su cui sono applicati. Questa è una tecnologia che potrebbe essere implementata e integrata in varie soluzioni architettoniche o nell'elettronica di consumo. Dopo aver presentato i principi fisici di tali dispositivi e determinato le metodologie ottiche per aumentarne le prestazioni, vengono illustrati alcuni esempi dove, teoricamente e sperimentalmente, riusciamo a intercettare la radiazione solare con antenne ottiche. Riportiamo, per la prima volta in letteratura, un'antenna ottica con nano-gap che accoppia efficacemente la luce solare nel nostro materiale attivo a film sottile. Nell'ultima parte sviluppiamo il concetto di tecnologia solare integrata negli edifici, introducendo alcuni esempi di facciate solari. Basando il design sulla nostra ricerca, è possibile realizzare una cella solare fotovoltaica organica trasparente, con una trasparenza superiore del 20% e un'efficienza di conversione fotone-elettrone migliorata grazie all'ottica, che risulta molto vicina all'equivalente cella fotovoltaica organica non trasparente.



## Acknowledgements

I want to thank the European Commission that supported my PhD studies at the Fresnel Institute in France and the Institute of Photonic Science in Spain. I would like to thank Dr. Nicolas Bonod and Prof. Jordi Martorell for allowing me to use their respective facilities, guiding me on the difficult path of a PhD in science.

Creating this work would be impossible without the personal and scientific support of many people around me. First of all my parents Angelo and Gabriella for supporting me through all my studies. My sister Laura and the rest of the family for always providing me with love and kind words. Old and new friends and colleagues that all helped me create this work: Fatma-Zohra, Nicolo', Michela, Brice, Soffia, Alberto, Camila, Rafa, Marina, Pablo, Paola, Xavi, Can, Francisco, Marc, Jan, Johann, Luis, Carme, Ramaiah, Enrique, Anshuman, Guillaume, Brian, Pascal, Alla, Julien, Alex, Victor, Muamer, Antonio, Serena, Vincenzo, Simona, Nadia, Heidbra, Jean-Christophe, Anna, Giorgio, Maria, Emanuele, Gianvito, Tieh-Ming, Alessio, Pietro, Simon, Thomas.

This thesis would not have happened without the collaboration of Dr. Sébastien Bidault and Prof. Niek van Hulst with all their inspiring comments and suggestions.

In the Fresnel Institute I would like to thank Prof. Sophie Brasselet who was always there when needed, as well as Evelyne, Nelly, Claire, Frederic, Christophe. I would like also to thank Prof. David Artigas and the ICFO units (NanoLab, Purchasing, Electric workshop, Administration, Frontdesk, ...).

The work described in this thesis was supported by the European Commission through the Erasmus Mundus Joint Doctorate Programme Europhotonics (Grant No.159224-1-2009-1-FR-ERA MUNDUSMJD).





## List of Publications

### During PhD:

1. F. Pastorelli, S. Bidault, J. Martorell and N. Bonod, “Self-assembled plasmonic oligomers for organic photovoltaics” submitted to *Advanced Optical Materials*, accepted, 2013.
2. N. Accanto, J. B. Nieder, L. Piatkowski, M. Castro-Lopez, F. Pastorelli, D. Brinks, N. F. van Hulst, “Universal Control of Femtosecond Pulses Using Second Harmonic Nano-Particles”, submitted to *Nature Light Science and Applications*, accepted, 2013.
3. F. Pastorelli, P. Romero Gomez, R. Betancur, A. Martínez-Otero, N. Bonod and J. Martorell, “Enhanced Light Harvesting in Semitransparent Organic Solar Cells Using an Optical Cavity Configuration”, in preparation, 2013.
4. J. Renger, R. Betancur, F. Pastorelli, N. Bonod, G. Demésy, J. Martorell, R. Quidant, “Plasmonic enhanced solar absorbers”, in preparation.

### Before PhD:

5. F. Pastorelli, et al. “Antireflection film, solar battery cell, method for manufacturing antireflection film, and method for manufacturing solar battery cell”, JP Patent 2,011,119,740, 2011.
6. F. Gesuele, A. Williams, F. Pastorelli, T. Gu, and C. W. Wong; “EFRC: transient pump-probe and photocurrent setups for multi-exciton generation and charge/energy transfer”, internal communication, Columbia University, New York City, U.S., 2010.
7. A. Higo, F. Pastorelli, K. Watanabe, M. Sugiyama, and Y. Nakano, “Design and fabrication of broadband anti-reflection sub-wavelength periodic structure for solar cells”, *Renewable energy 2010*, Yokoama, O-Pv-5-5, 2010.

### Recently accepted conferences:

Euromics Spring School (Barcelona 2012, Karlsruhe 2013), CEN2012 (Sevilla 2012, winner of the Phantoms Foundation grant), ICFO Annual Poster Session - CLP day (Barcelona 2012, poster finalist), Medinano5 (Barcelona 2012), Plasmonica2013 (Milano 2013), CLEO-Europe (Munich 2013), E-MRS (Strasbourg 2013), SSOP3 (Cargese 2013), Complex Nanophotonics (London 2013, winner of the nanophotonics for energy grant).



## Glossary

PV	–	photovoltaic.
Cell	–	the basic unit of a PV panel.
kW	–	kilowatt.
MW	–	megawatt.
GW	–	gigawatt.
$V_{oc}$	–	open circuit current.
$J_{sc}$	–	short circuit current.
$V_m$	–	voltage for the maximal solar cell power.
$J_m$	–	current for the maximal solar cell power.
Bulk heterojunction	–	in this type of photovoltaic cell, the electron donor and acceptor are mixed together, forming a polymer blend.
OPV	–	organic PV.
NP	–	nano particle.
L	–	longitudinal light polarization.
T	–	transversal light polarization.
k vector	–	light propagation vector.
AuNP	–	gold NP.
EQE	–	external quantum efficiency.
AFM	–	atomic force microscope.
SEM	–	scanning electron microscope.
FiT	–	feed-in tariff.
BIPV	–	build integrated PV.
BIOPV	–	build integrated organic PV.
STBIOPV	–	semi-transparent OPV.
D65	–	CIE standard illuminant D65.
$V(\lambda)$	–	human photopic spectral response.
ARC	–	antireflection coating.
IR	–	infrared.

MLD	–	dielectric multilayer.
STC	–	semi-transparent PV cell.
RoSH	–	directive on the restriction of the use of certain hazardous substances in electrical and electronic equipment.
CIGS	–	copper indium gallium selenide ( $\text{CuIn}_x\text{Ga}_{(1-x)}\text{Se}_2$ ).
CdTe	–	Cadmium telluride (CdTe).
D	–	diode.
I	–	photocurrent.
$R_p$	–	parallel resistance / shunt resistance.
$R_s$	–	series resistance.
V	–	voltage.
J	–	photocurrent normalized for 1 cm <sup>2</sup> PV cell.
$\eta$	–	efficiency.
$P_{\max}$	–	maximal electrical power.
FF	–	fill factor.
$P_{\text{light}}$	–	light power.
D-A	–	donor - acceptor.
HTL	–	hole transporting layer.
ETL	–	electron transporting layer.
$T(\lambda)$	–	transmission in function of the wavelength.
$\lambda$	–	wavelength.
DTT	–	dithiothreitol.
AM1.5G	–	standard sun radiation after passing the air mass of 1.5, useful to represent the overall yearly sun radiation average for mid-latitudes.
SSP	–	surface plasmon polariton.
LSPR	–	localized surface plasmon resonance.
NI	–	nano island.
UV	–	ultra violet.
VLT	–	visible light transmission.
L	–	luminosity.

Different materials are listed in appendix A.

## List of figures and tables

**Figure 1.1:** Solar irradiation (external yellow box) compared with established global energy resources (internal small boxes) and annual global energy consumption (smallest red box). Fossil fuels and uranium are expressed with their total reserves while renewable energies with their yearly potential.

**Figure 1.2:** A scheme for implementation of renewable energy for a sustainable future.

**Figure 1.3:** Evolution of global PV cumulative installed capacity 2000-2012 (MW) [1.12].

**Figure 1.4:** Historic summary of champion cell efficiencies for various photovoltaic technologies, adapted from [1.19].

**Figure 2.1:** Simplified schematic representation of a solar cell device, single diode equivalent circuit model with parallel and series resistances.

**Figure 2.2:** A typical Current/Voltage characteristic for a solar cell. “ $V_{OC}$ ” and “ $J_{SC}$ ” are the open circuit voltage and current, “ $V_m$ ” and “ $J_m$ ” are the voltage and the current at the point of maximal cell power.

**Figure 2.3:** Schematic Illustration light harvesting in a bilayer organic solar cell device, (a) the light is absorbed and an exciton is created, (b) the exciton moves in the material until finds an interlayer that separates the electron and the hole, at this point the charges can travel (c) and be collected (d) reaching the respective electrode.

**Figure 2.4:** (a) An idealized bulk heterojunction structure, (b) Mixture of two dissimilar molecules leading to recombination, (c) Mixture of two dissimilar molecules leading to efficient exciton diffusion [2.5].

**Figure 2.5:** Architecture types depending on the charges collected by the semi-transparent electrode through which the sunlight enters the cell.

**Figure 3.1:** Fresco of one of the first, documented, solar collector where the sun light is collected and redirected on a ship [3.3].

**Figure 4.1:** Optically enhanced OPVs schematic, (a) a surface plasmon resonance enhanced device with NPs located in a random configuration, (b) a surface plasmon polaritons enhanced device with a grating displaced in a periodic configuration.

**Figure 4.2:** Scattering cross-section of a 40 nm gold particle with respect to the incident wavelength when considering a monomer (black line) or a dimer when the incident electric field is polarized along (L, blue dashed line+circles) or perpendicular (T, red line+squares) to the axis of the dimer. The average over both polarizations is represented by the green line. In the case of a dimer, this ratio is averaged over

the incident polarization, the dimer is illuminated in normal incidence, i.e. the incident  $\mathbf{k}$  vector is normal to the dimer axis. These cross-sections are estimated per particle and normalized with respect to the particle surface area.

**Figure 4.3:** Electric field map for dimer and monomer for different wavelength, longitudinal and transversal polarizations.

**Figure 4.4:** (a) Schematic representation of the fabricated and characterized solar cells. It is composed of a 100 nm thick Ag layer, a 10 nm thick  $\text{MoO}_3$  layer, a 170 nm thick P3HT:PCBM layer, a 60 nm thick  $\text{TiO}_2$  layer and a 120 nm thick ITO layer covered by a thick glass layer. (b) Optical density of two solutions of colloidal gold particles (2nM concentration of AuNPs). Red line: monomers of 40 nm gold particles, green line: same solution after performing the self-assembly method. (c-d) Self-assembled oligomers on an ITO substrate imaged by scanning electron microscopy. c: monomer solution, d: oligomer solution composed of monomers (70%), dimers (23%) and trimers (7%). 49% of the particles are coupled in oligomers.

**Figure 4.5:** (a) Measurements of the External Quantum Efficiency with respect to the wavelength and (b) J-V curves for the three cells, standard (black line) and loaded with plasmonic monomers (monomers red line) and oligomers (green line). External quantum efficiency in %, wavelengths in nm, short circuit current  $J_{\text{SC}}$  in  $\text{mA}/\text{cm}^2$  and tension in V.

**Figure 4.6:** (Left scale) Relative difference in % of the EQE between the solar cells loaded with oligomers and monomers (green line) and between the pristine solar cells and the solar cells loaded with monomers (orange line) as a function of the wavelength. (Right scale, blue line) Normalized difference between the scattering cross-sections calculated with a dimer and a monomer. In the case of the dimer, the scattering cross-section is calculated per particle, and is averaged over both polarizations.

**Figure 4.7:** Schematic of the solar cell with nano-structuration: (a) 3D representation, (b) 2D representation with dimensions.

**Figure 4.8:** Electromagnetic field distribution and contribution of the individual layers to the absorption response. The comparison of the planar cell (dashed) to the nano-structured cell (solid) reveals that the reduced back reflection originates mainly from the enhanced absorption in the active blend layer.

**Figure 4.9:** The strong near-field interaction between the metallic particle and the substrate increases the electromagnetic field inside the active layer.

**Figure 4.10:** AFM image of the nano-structure.

**Figure 4.11:** The EQE is enhanced for the different nano-structures. The measured data (left) are in close agreement with the expected theoretical predictions (right). The SEM images shown as an inset in (b) and (d) have been taken after the lithography under 45-degree tilted angle-of incidence.

**Figure 5.1:** Schematic diagram of semi-transparent building-integrated organic photovoltaic (STBIOPV).

**Figure 5.2:** Human eye and illumination information for the analyzed semi-transparent devices: Illuminant D65 (solid orange line) and human photopic spectral response (black line).

**Figure 5.3:** Schematic illustration of the semi-transparent device cell architecture incorporating the MLD between the glass and the Au thin metal electrode and ARC above the Ag thin metal electrode. Near IR light is partially confined in the active layer (PTB7:PCBM) while the luminosity or visible transparency for the device is kept above 20 %.

**Figure 5.4:** Light transmission for STC1 (dotted line) and for STC2 (dashed grey line). Inset: Picture of STC1 (top image) and STC2 (bottom image).

**Figure 5.5:** Measured J-V curves for the semi-transparent device (STC1) shown in Figure 5.3 (solid green) for the STC2 (solid cyan), and for the opaque solar cell (solid black).

**Figure 5.6:** Experimentally measured (a) and Simulated (b) external quantum efficiencies for the semi-transparent device showed in the Figure 5.3 incorporating the MLD (in green) a semi-transparent solar cell without light trapping (in cyan) and the opaque solar cell (in black).

**Figure A.1:** Deposition methods diagrams employed (a) spincoating, (b) sputtering and (c) thermal evaporation

**Figure A.2:** Extinction spectra of mPEG stabilized single particles (red line) and electrophoretically optimized oligomer solution (green line) suspensions. Inset: left monomers, right oligomers.

Inset table from **Figure 1.3:** Evolution of global PV cumulative installed capacity 2000-2012 (MW) [1.12].

**Table 1.1:** Newly installed PVs capacity and total recycle collection points [1.12, 1.13].

**Table 4.1:** Solar cell characteristics measured from I-V solar simulator.

**Table 5.1:** Solar cell J-V characteristics.





# Contents

Abstract	ix
Resumen	xi
Résumé	xiii
Riassunto	xv
Acknowledgements	xvii
List of Publications	xix
Glossary	xxi
List of figures and tables	xxiii
Contents	xxvii
1. Renewable energies context	29
1.1 Energies global status	30
1.2 The special case of photovoltaics	34
2. Solar cells physics	39
2.1 I-V characteristics of a solar cell	40
2.2 Organic solar cell characteristics	44
3. Optical enhancements	51
3.1 Optimizations of solar cell	52
3.2 Optical enhancement for ultra-thin film solar cell	58

4. Optical nano-antenna improved OPVs	61
4.1 Optical antennas effects	62
4.2 Self-assembled plasmonic nanogap antennas for organic photovoltaics (random configuration)	65
4.3 Plasmonic enhanced solar absorbers (periodic configuration)	77
5. Semi-transparent and Optical cavity enhanced OPVs	85
4.1 Transparent solar facades	86
4.2 Enhanced Light Harvesting in Semi-transparent Organic Solar Cells using an Optical Cavity configuration	90
Conclusions and Remarks	101
Appendix A. Materials and methods	105
A.1 Deposition methods	105
A.2 Materials	107
A.2.1 Plasmonic materials	107
A.2.2 Active materials	109
A.2.3 Buffer layers	117
A.2.4 Electrodes	126
A.2.5 Other materials	133
References	135

# 1.

## **Renewable energies context**

This chapter contains an overview of the world current energy situation, with emphasis on renewable energies. We mention a few examples of new dynamics in energy planning and production. With the knowledge of how much energy the sun provides us with every year this paper focuses on photovoltaic technologies and on upcoming solutions that will accompany a whole new range of applications.

## 1.1 Energies global status

The year 2012 was characterized by a slow economical growth while global energy consumption grew by 1.8% with respect to the previous year. This growth was only due to emerging countries since all Western countries registered a minus sign. In Europe the total consumption decreased by -0.5% and in US by a significant -2.8% [1.1]. Looking at our consumption levels for the last two years for the different energy sources, we see that our annual consumption percentage of fossil fuels has been constant\*. While the production of nuclear energy was lowered from 4.9% in 2011 to 4.5%. Hydropower and other renewable energies increased their presence with a total percentage of 8.6% of the shared primary energy consumption.

Being optimistic, ideally assuming a 0% energy consumption growth, (and thereby denying pollution, CO<sub>2</sub> emissions and a reduction in quality of life) and considering the world proved fuel reserves, we can see that crude oil and natural gas will only last us for 50 years and coal for another 70 years. If we compare these total reserves with other energy sources [1.1-1.2] it is clear that it would be sensible to move towards a world more driven by renewable energies. Figure 1.1 (adapted from [1.2]) visualizes a comparison between the total proved reserves. Fossil fuels are represented in the middle, the yearly potential of renewable energies on the left and the small red box in the lower right corner represents the worlds annual energy consumption. The external yellow box represents the total amount of solar energy that reaches earth each year.

---

\* of the yearly energy consumption, oil represents 33.1%, gas 23.9% and coal 29.9%.

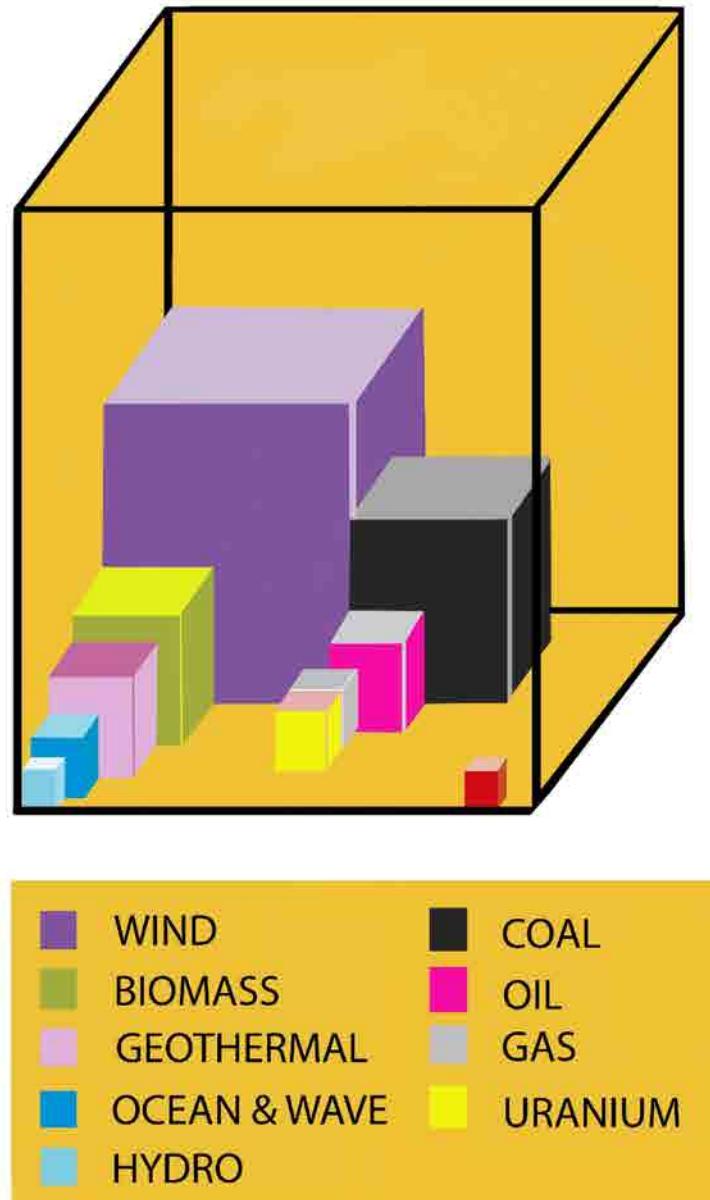


**Figure 1.1:** Solar irradiation (external yellow box) compared with established global energy resources (internal small boxes) and annual global energy consumption (smallest red box). Fossil fuels and uranium are expressed with their total reserves while renewable energies with their yearly potential.

Geographically speaking this scenario is very diverse accounting the different resources of each continent. Considering only Europe and applying the, above mentioned, 0% energy consumption growth, we see that oil and gas reserves will be finished within the next 10 years while coal has a bit of a longer span. Uranium has been

proven to be economically as well as health and environmentally unsustainable [1.3] and does not provide a significant improvement in the total amount of reserves. The prospect of lacking resources in a near future has motivated Europe to become the driving force within renewable energies developments. In 2013 12% of all energy consumption in Europe is coming exclusively from renewable energies. The goal<sup>†</sup> for 2020 is to reach a renewable energy coverage of 20% [1.4], and with the so called “rethinking 2050” project [1.5] they are gathering experts and collecting ideas to reach a 100% sustainable energy production within 2050.

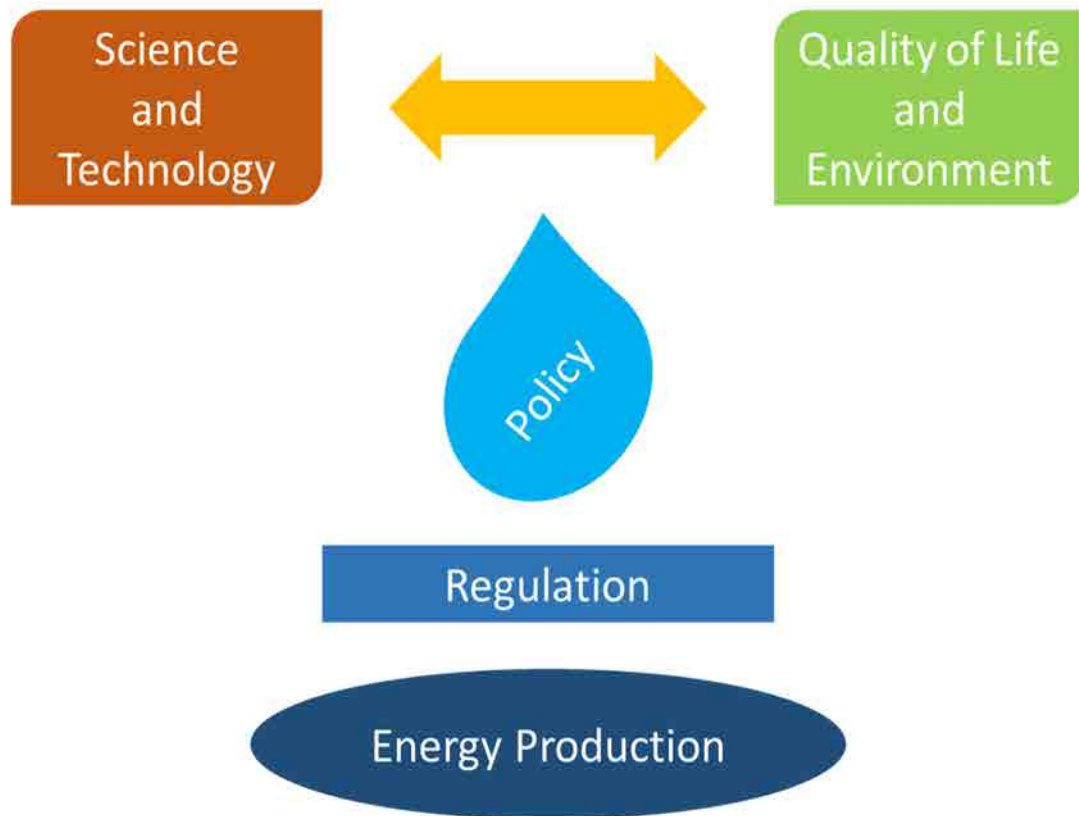


**Figure 1.2:** A scheme for implementation of renewable energy for a sustainable future.

<sup>†</sup> These targets, known as the "20-20-20" targets, set three key objectives for 2020:  
 A 20% reduction in EU greenhouse gas emissions from 1990 levels;  
 Raising the share of EU energy consumption produced from renewable resources to 20%;  
 A 20% improvement in the EU's energy efficiency.

In figure 1.2 is presented a simplified model of a sustainable energy production with the factors necessary for a successful outcome. It shows how we ought to create responsible policies based on dialog balancing “science and technology” and “quality of life and environment”. The reassessed policies will then be paired with a light set of regulations. The regulations are there to encourage the production of sustainable energy, without rushing technologies in development by placing them under not suitable circumstances.

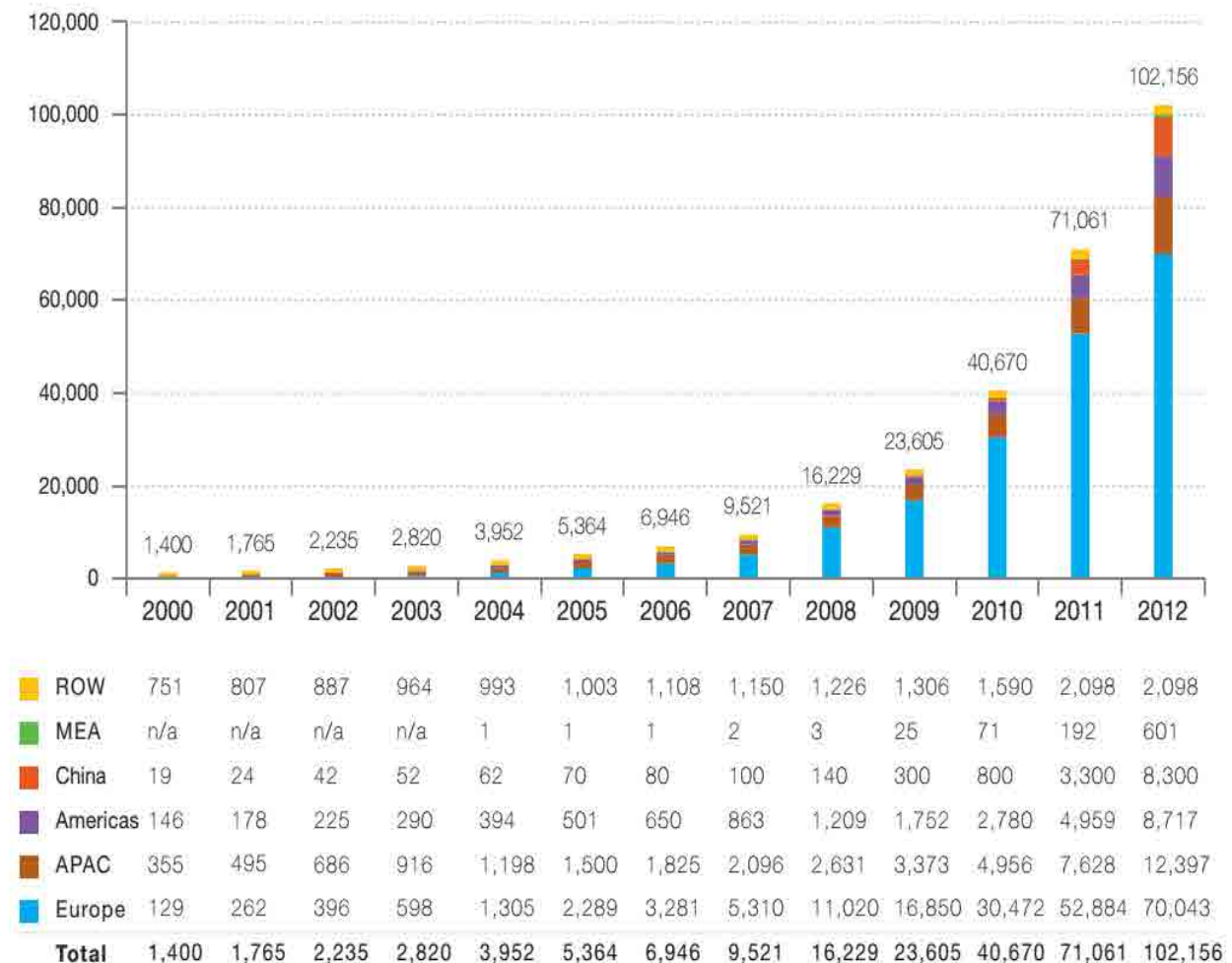
A sustainable energy production is possible, if the above-mentioned parameters are taken into account and if an advanced grid management [1.6-1.8] is implemented accordingly to ensure the de-localized and non-constant energy production and consumption. Specifically in Europe a welfare-enhancing business model [1.9] is possible considering the broad range of new technologies. Differentiating between the various energy sources is fundamental. Amongst all the sustainable energy sources, the sun is the most promising one due to its enormous yearly potential (see figure 1.1). Thermal solar energy is already economically favourable in sunny countries. In Barcelona [1.10] all new constructions need to have, amongst all of the energy saving parameters, a solar thermal system for heating and hot water. Besides solar thermal, thermal photovoltaic is getting increased attention, but thermal photovoltaic is unfortunately not suitable for rooftop applications.

Photovoltaic technology, which converts direct solar radiation into electricity, seems to be the most efficient way of exploiting the potential of the sun. This technology is growing every year and new solutions are emerging from research. In Japan for example, in July 2012, after the Fukushima Tsunami-Nuclear Disaster, a series of incentives were made for various energy resources and in particular to residential photovoltaic [1.11].

Because of the declining fossil fuel reserves, we aim in the near future to implement more renewable energies that will go hand in hand with a reduction of polluting energy productions. Based on the yearly solar potential, we will focus in this work on photovoltaics and in particular on ultra-thin film photovoltaics in order to broaden application possibilities and reduce production and installation costs.

## 1.2 The special case of photovoltaics

Solar cell technologies are each year becoming bigger contributors to the total yearly energy production. As shown in figure 1.3, the rapid growth in the last years achieved in 2011-12 a constant growth value of about 30 GW/year in newly installed PVs modules.



ROW: Rest of the World. MEA: Middle East and Africa. APAC: Asia Pacific.

**Figure 1.3:** Evolution of global PV cumulative installed capacity 2000-2012 (MW)

[1.12].



Together with the newly installed PV modules a development in solar cell recycling technologies is emerging. With a life span of 20 years for a silicon photovoltaic panel, the “PV cycle” association [1.13] is determined on developing knowledge on PV recycling processes and in increasing the number of collection points, see table 1.1. A side the gathering of old photovoltaics modules, reviewing the regulations schemes is important to keep the energy production at a real effectiveness rate.

**Table 1.1:** Newly installed PVs capacity and total recycle collection points [1.12, 1.13].

	<i>2011 newly installed capacity</i>	<i>2012 newly installed capacity</i>	<i>Recycle Collection points</i>
<i>Germany</i>	7.5 GW	7.6 GW	90
<i>China</i>	2.5 GW	5.0 GW	n.a.
<i>Italy</i>	9.5 GW	3.4 GW	77
<i>US</i>	1.9 GW	3.3 GW	n.a.
<i>Japan</i>	1.3 GW	2.0 GW	n.a.
<i>France</i>	1.8 GW	1.1 GW	41
<i>Spain</i>	0.5 GW	0.3 GW	9

Until now the PV market has been driven by financially motivated corporate companies more than environmental values, the pursuit of life quality and cost-benefits of the chosen technology. In Germany [1.14], there are positive examples of small producing and distributing companies that with a reasonable feed-in tariff (FiT) for building integrated photovoltaic (BIPV), are keeping up the market although solar radiation is not altogether favourable for the European climate. In Italy one can find a good balance between solar radiation and feed-in tariff [1.15-1.16] (funding finished the 6<sup>th</sup> of July 2013), despite the presence of big producing companies that speculated in PV ground installations in the previous years. Probably the worst scenario in this sense is yet to come in Spain where the amount of solar radiation can encourage the proliferation of BIPV, even without any feed-in tariff, in small communities or families. Here big corporate economic interests are acting against self-sufficient energy families and communities by suggesting an “energy self consumption” tax [1.17] on energy produced

by PV modules and home mini wind turbines. The 2012 PV market in Europe slightly decreased compared to the previous year as a result of the uncertain climate, see the table in figure 1.3.

An alternative way to improve the quality of the PV industry is to gradually introduce a specific RoHS directive [1.18] in this area where the threshold of economic advantage is already achieved (in the year 2000 the price of a 3kW household PV system was 20,000 euro while now the same system costs around 6,000 euro). Additionally it would be preferable to discourage ground plant installation in the non-desert areas and there focus the economical efforts in favouring the BIPV solutions.

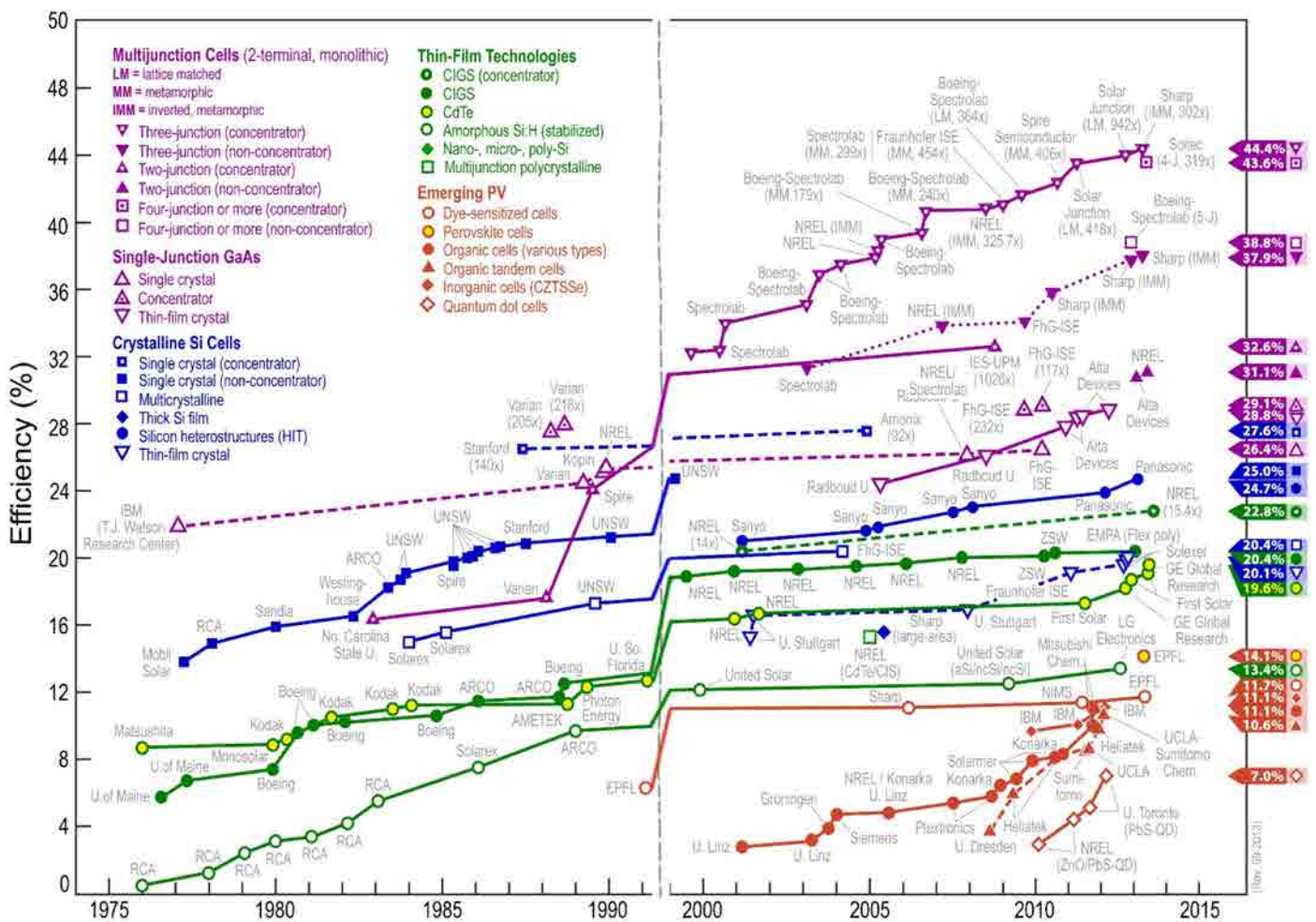


**Figure 1.4:** Historic<sup>‡</sup> summary of champion cell efficiencies for various photovoltaic technologies, adapted from [1.19].

<sup>‡</sup> Note how the graph starts after the 1973-74 oil crisis.

Within the field of building integrated photovoltaics, lightweight modules (capable of being transparent, flexible or conformal) are the high-end energy technologies to pursue. The biggest fundamental issue is how to develop a photovoltaics energy production that is affordable and low on pollution. In this field, a lot of research and development efforts are exploring different approaches as shown in figure 1.4.

The currently used technologies come, for the majority, from the central part of figure 1.4 where the solar cell efficiency is somewhere between 10 % and 25 % with a high installation cost. Taking into account their volume and weight, these technologies are, basically, only for rooftops and ground installations. The future possibilities for the photovoltaic technology are the introduction of highly performing solar cells combined with solar concentrators and antireflection coatings capable of an efficiency level of about 44% [1.20-1.22]. Many research groups are looking 10 years ahead trying to achieve a 50 % efficiency level [1.23]. In this case, the cost can be kept reasonable by reducing the size of solar cell devices thanks to the solar concentrator design (which can reach a magnification of up to a 1000x).

The lower part of figure 1.4 is dedicated to thin film technologies, which can more easily be installed because of their lightweight. Additionally some upcoming technologies will be transparent, flexible and usable in completely new applications like window energy generation or direct power source for consumer electronics.

Summarizing, for reducing costs in the production of photovoltaics energy, there are two strategies: the first one is to enhance the efficiency and concentrating the light, allowing for less material and space consumption. The second one is applying cheap, lightweight and transparent materials in order to broaden the installation possibilities. This work is dedicated to finding a general solution for optimizing the light inside a solar cell, and in particular in ultra-thin solar cells that have an active material with a thickness below 200 nm. In the next chapter, the physics of a solar cell is presented, introducing the optical enhancement overview in chapter 3. In chapter 4, we show theoretically and experimentally some optically enhanced designs, while in chapter 5 we will show theoretically and experimentally a transparent solar cell that performs closely to its opaque correspondent.



# 2.

## **Solar cells physics**

Solar cell devices can be schematized and solved as a simple electrical circuit. The external observables like current and voltage can be measured and compared in the same way for all the different technologies. On the other hand, the intrinsic characteristics of the device and its physics depend on each particular case. Special attention is devoted to organic photovoltaics and its light – electron conversion scheme. We present the morphology characteristics of the absorbing material and we analyze the architecture of two different devices.

## 2.1 I-V characteristics of a solar cell.

The study of the electrical characteristics of photovoltaic devices is generally common to all the different technologies and it could be represented as a basic electrical circuit. A solar cell in the dark state is schematized like a diode “D” and when irradiated by light it can be schematized as a current generator “ $I_L$ ”. **Figure 2.1** represents the electric behaviour of a such system [2.1]. The parallel resistance “ $R_P$ ” is commonly also called shunt resistance (or  $R_{Sh}$ ) and takes in account all the current losses in the solar cell. The series resistance “ $R_S$ ” takes into account all the electric connection.

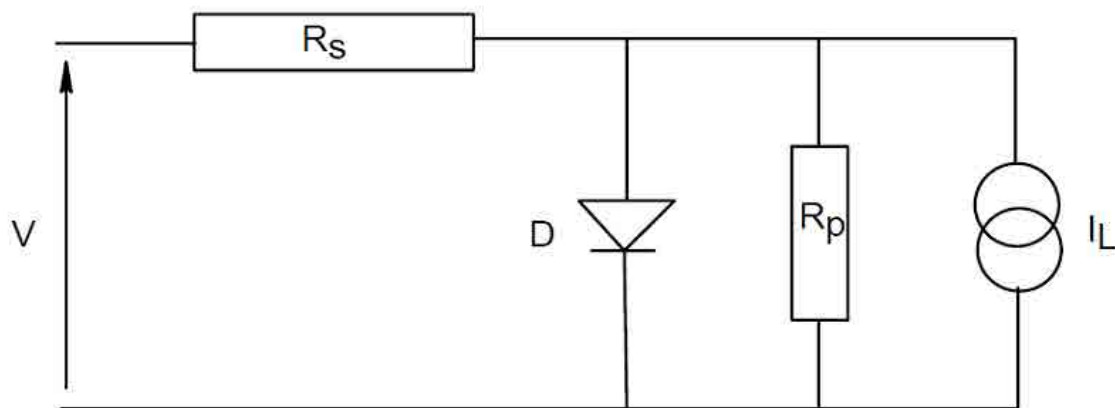


**Figure 2.1:** Simplified schematic representation of a solar cell device, single diode equivalent circuit model with parallel and series resistances.

The most widely used method for solar cell characterization is the current-voltage characteristic of the cells, i.e. I/V measurement [2.1, 2.2]. It provides very important electrical properties of the cell, from which one can judge how the cell parameters have to be further changed, in order to achieve a higher efficiency in sun-light harvesting. The I/V characteristic is influenced by the conductivity of materials and interfaces, exciton or charge carrier diffusion lengths, traps and recombination. Those parasitic

resistances can also be modelled as before, see figure 2.1, with a  $R_P$  and  $R_S$ . Ideally,  $R_P$  would be infinite and would not provide an alternate path for current to flow, while  $R_S$  would be zero, resulting in no further voltage drop before the load.

Solving the circuit, using the Shockley equation for an ideal diode where “ $V_D$ ” is the diode voltage and “ $I_D$ ” is the diode current, we obtain the observables used in evaluating the performances of any solar cell device:

$$I = I_L - I_D - \frac{V_D}{R_P} \quad (2.1)$$

$$V_D = V + IR_S \quad (2.2)$$

$$I_D = I_S \left( e^{\frac{qV_D}{nkT}} - 1 \right) \quad (2.3)$$

where “ $n$ ” is the ideality factor, that represents how closely the diode follows the ideal diode equation, and “ $I_S$ ” is the saturation current of the diode.

Then:

$$I = I_L - I_S \left( e^{\frac{qV_D}{nkT}} - 1 \right) - \frac{V_D}{R_P} \quad (2.4)$$

Further on, we can calculate the most important parameter for evaluating performance of a solar cell: the efficiency “ $\eta$ ”. This value expresses how much of the incident light power on the photovoltaic cell “ $P_{\text{light}}$ ” is converted into electric power “ $P_{\text{max}}$ ”:

$$\eta = \frac{P_{max}}{P_{light}} \quad (2.5)$$

The measurement of the I/V characteristics is done in the following way: during illumination, a voltage is applied to the electrodes of the cell and the flowing current is measured. The current is divided by the exact cell surface, thus normalized to  $1 \text{ cm}^2$ . From now on, we will indicate “I” as a general current while “J” represents the current normalized and consequently they became equivalent for a  $1 \text{ cm}^2$  solar cell. In **Figure 2.2** we can observe a typical J/V curve.

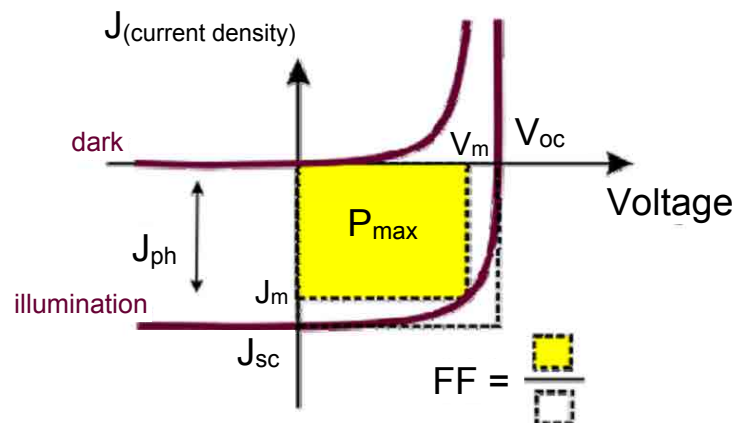


**Figure 2.2:** A typical Current/Voltage characteristic for a solar cell. “ $V_{oc}$ ” and “ $J_{sc}$ ” are the open circuit voltage and current, “ $V_m$ ” and “ $J_m$ ” are the voltage and the current at the point of maximal cell power.

As known, the electrical power of a device is the product of current and voltage. The electrical power has a maximum at one point of the J/V curve. This is the point where current and voltage is marked as  $J_m$  and  $V_m$ , respectively. Exactly their product gives  $P_{max}$  of the solar cell. On the J/V curve there are two other important points,  $V_{oc}$  and  $J_{sc}$ , that we can directly measure in our experiments. The short circuit current is



called  $J_{SC}$  and is the point where the curve cuts the Y-axis (or current density axis). There the applied external voltage goes to zero. This is the point where the measured current is exactly the current yielded by the solar cell if its electrodes were short-circuited (from there “sc”). The open circuit voltage ( $V_{OC}$ ) is the intersection of the J/V curve with the X-axis (or voltage axis). There the applied external voltage is exactly equal to the internal voltage of the cell, so no current will flow. These points are respectively the maximal current, and the maximum voltage that the cell can deliver. In case of the ideal diode their product would give the maximal power of the cell, but in reality one more fundamental factor is induced, the fill factor (FF):

$$FF = \frac{J_m \cdot V_m}{J_{SC} \cdot V_{OC}} \quad (2.6)$$

The fill factor shows how strong the form of the J/V curve deflects from the curve form of an ideal diode. Consequently, the power conversion efficiency of the solar cell is being calculated using the following equation:

$$\eta = \frac{J_m \cdot V_m}{P_{light}} = \frac{FF \cdot J_{SC} \cdot V_{OC}}{P_{light}} \quad (2.7)$$

Therefore, the J/V measurement of a photovoltaic device gives us some very useful information about the device and its internal contact interfaces. A more accurate study can be done looking closer into the physics of a specific solar cell technology. In this work we focus on organic devices as they represent a suitable technology for BIPV and consumer electronics as mentioned in Chapter 1.

## 2.2 Organic solar cell characteristics

The organic photovoltaic technology is a special case where all the electrical I-V characteristics are the same as other photovoltaic technologies, but the device physics is different. When light hits the active material, a photon is absorbed and one electron-hole pair (exciton) is generated. In the case of silicon, this exciton is automatically dissociated in a hole and an electron thereby generating electrical current, while in an organic material the exciton is tightly bound and has a limited lifetime before it recombines [2.3]. This translates into a diffusion length of about 10nm in the organic material. In order to dissociate, the exciton has to reach a donor-acceptor interface (D-A) facilitating the generation of electrical current. This D-A consists of different charge carrier semiconducting material, one having good transport properties for holes (donor) and the other favouring the transport of electrons (acceptor).

In this section, for the sake of simplification we schematize the device as a two layer material. Later in this work we present the use of a bulk heterojunction consisting of a blend of the two materials in order to minimize the bottleneck of the exciton diffusion length [2.4] (we bring the interface as close as possible to the area where the exciton is generated). Assuming that the light is absorbed in the material creating an exciton, **Figure 2.3** (a), this exciton has to travel until it finds an interface, **Figure 2.3** (b), that allows an easier charge separation. At the interface point, both the electron and the hole are free to move, **Figure 2.3** (c), in the direction of the electrode that will collect the carriers, **Figure 2.3** (d).

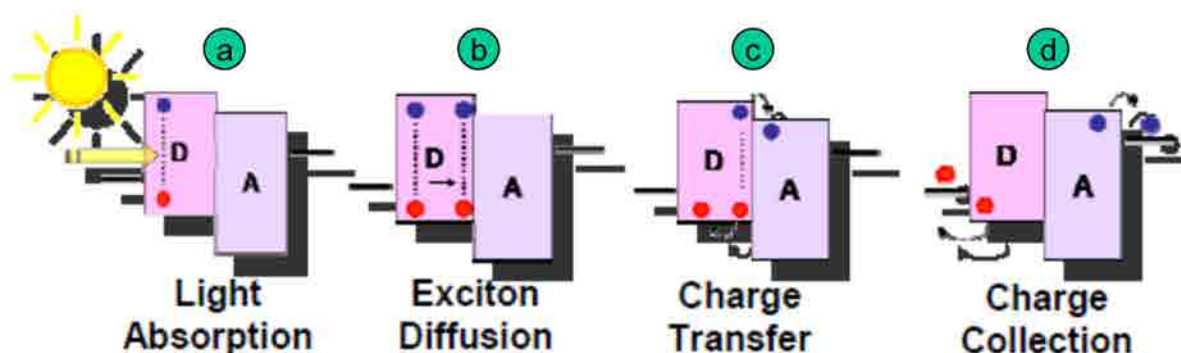


**Figure 2.3:** Schematic illustration of light harvesting in a bilayer organic solar cell device, (a) the light is absorbed and an exciton is created, (b) the exciton moves in the material until finds an interlayer that separates the electron and the hole, at this point the charges can travel (c) and be collected (d) reaching the respective electrode.

In the steps of Figure 2.3 we encounter a quenching mechanism that recombines the excitons or carriers and consequently reduces the overall efficiency. In the light absorption process, depending on the material characteristic and thickness, we are typically able to absorb about  $2/3$  of the incident light in the working spectra of the specific material. This is translated in the photon absorption efficiency “ $\eta_{\text{abs}}(\lambda)$ ”, figure 2.3a. We are not able to absorb the remaining  $1/3$  of the photons because we are limited by the exciton diffusion length. This limitation leads to a typical organic solar cell active material not being thicker than 200 nm. The absorption efficiency is also strongly depending on the incident wavelength for two reasons: First of all the wave profile for each wavelength inside the active material has to be related to the volume of interaction in the active material<sup>§</sup>. Secondly, independent of its size the active material has a different wavelength response (refractive index). Analysing the other steps in light harvesting in a bilayer organic solar cell, we realize that they are wavelength independent. After the absorption step a photon is converted into an exciton and we can represent the efficiency of the exciton diffusion, figure 2.3b, as “ $\eta_{\text{ed}}$ ”. Once the exciton reaches the interface we can assign a charge separation efficiency “ $\eta_{\text{cs}}$ ” quantifying the

<sup>§</sup> integrating the active layer volume and the field intensity distribution in the active layer will give the photon absorption value

number of excitons over the total amount dissociated. The charge transfer efficiency “ $\eta_{ct}$ ” identifies the number of charges, which can effectively go from the interface of the bilayer material to the edge of the active layer itself, figure 2.3c. At the end of the process the charges need to be collected from the electrodes to create current and generate power, and this charge collection efficiency can be expressed as “ $\eta_{cc}$ ”. Now we can take into account all the different efficiencies to obtain a general expression for the number of photons arriving on the device that are converted into electrons; this defines the external quantum efficiency (EQE):

$$EQE(\lambda) = \eta_{abs}(\lambda)\eta_{ed}\eta_{cs}\eta_{ct}\eta_{cc} \quad (2.8)$$

As observed before, the only efficiency parameter dependent on the wavelength is the absorption efficiency, all the other parameters are wavelength independent since they represent an intrinsic characteristic of the system. Performances are related to the devices architecture and materials, a preference is reserved for an active material with a high ability of forming excitons that can travel efficiently and dissociate into their constituent electron-hole pairs, and reach the cell electrodes. Different strategies were implemented from the first bi-layer donor-acceptor solar cell. A mix of the two materials were introduced to compensate for the poor exciton diffusion length. Some of the proposed nano-geometries are reported in **Figure 2.4**.

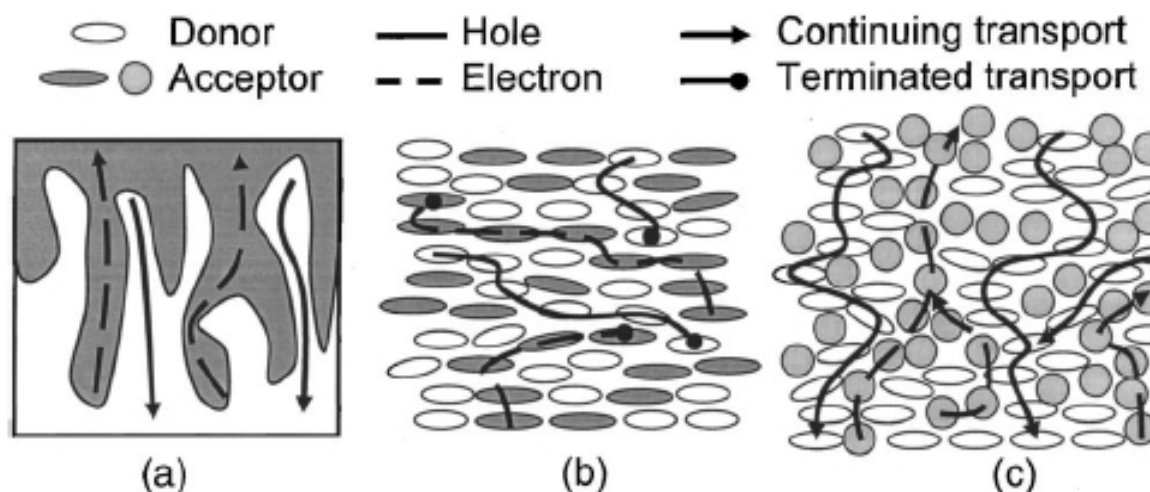


**Figure 2.4:** (a) An idealized bulk heterojunction structure, (b) Mixture of two dissimilar molecules leading to recombination, (c) Mixture of two dissimilar molecules leading to efficient exciton diffusion [2.5].

In Figure 2.4 (a), an idealized bulk heterojunction structure is represented. The segregation of D-A molecules (or polymers) leads to an “interdigitated” structure with lateral feature sizes no larger than the exciton diffusion lengths. Figure 2.4 (b) shows a mixture of two dissimilar molecules, planar stacked, where disruption of the molecular stacks leads to charge trapping and ultimately recombination. While in Figure 2.4 (c) percolating paths are formed across the film consisting of a mixture of a planar stacking and spherically symmetric molecule. The nano-structured, spatially distributed D-A interface is responsible for efficient exciton diffusion in the mixture. This active materials nano-structuration is often associated with the morphology of the blend and could principally be improved by chemical or physical treatments. This improvement can for example be obtained by annealing in different ambient conditions, by having a different concentration in the mixture of the two materials or by physical nano-structuration [2.5].

It is hard to achieve the control of excitons in nanoscale systems [2.6] and this requires novel approaches. Nowadays the problem of exciton diffusion is readdressed

as “quantum coherence” [2.7]. It is possible to modify the internal resistance of the device by playing with the blend morphology [2.8].

A widely used donor material was Poly3-hexylthiophene (P3HT), which has intrinsically a 20 nm of exciton diffusion length [2.9-2.12]. This material has reached an efficiency between 2 and 5% depending on the device structure and the conditions of fabrication. Recently progress was made in obtaining “low bandgap” materials pushing the solar cell efficiencies above 8%. As acceptor materials the fullerene (PCBM) and fullerene derivatives are still considered the most efficient solution. A more extensive listing of active materials is reported in Appendix A.

To complete an organic solar cell device, other layers are added around the active layer to efficiently collect the carriers and ensure correct functioning of the device. Two electrodes are needed, one of them transparent in order to let the light transmit to the active layer. In between the active material and the electrodes a transporting layer is needed to optimize the efficiency and to electrically stabilize the device itself. A schematic of such multilayer device is shown in **Figure 2.5** where (a) represents a direct configuration and (b) an inverted configuration.

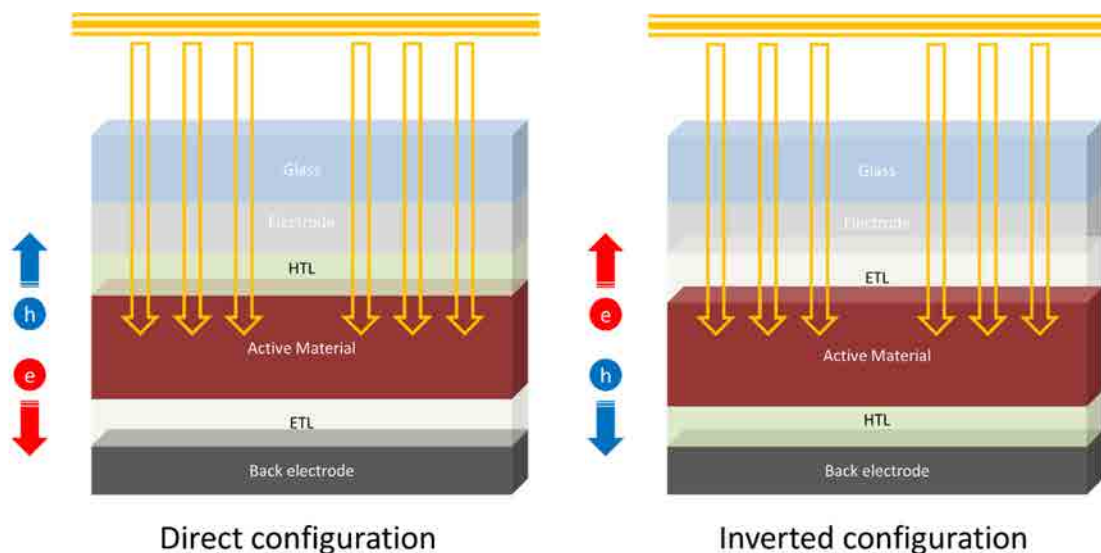


**Figure 2.5:** Architecture types depending on the charges collected by the semi-transparent electrode through which the sunlight enters the cell.

A direct configuration is when the light passes through the transparent electrode hitting the hole transporting layer\*\* (HTL), then the active layer, followed by the electron transporting layer†† (ETL) and at the end it encounters the back electrode. The holes travel to the transparent electrode while the electrons go to the back electrode. In the inverted structure the light first comes to the ETL and then the HTL. Therefore the electrons are travelling to the transparent electrode while the holes are travelling to the back electrode. In the way these devices are fabricated a typical material for HTL in direct configuration is PEDOT while in indirect configuration is MoO<sub>3</sub>. For the ETL a thin layer of LiF is used in direct configuration while ZnO is a promising alternative in an inverted device. An ITO layer is typically used as transparent electrode, but any material with good transparency and good carrier mobility can be used. For a more descriptive list of materials see Appendix A.

More structures were fabricated using the above mentioned structure as building blocks. Semi-transparent devices can for example be obtained simply by having a transparent electrode in both sides of the solar cell. A more advanced use of direct and inverted solar cells has been made by implementing tandem configurations. Recently these configurations have shown their potential even in the case of transparent devices [2.13-2.17]. As the word tandem suggests, we are in presence of piled up devices. For example a Series Tandem Solar Cell is the superposition of two direct or inverted solar cells, here the voltage sums up taking advantage of the double device structure. Opposed to this is the case of Parallel Tandem Solar Cells where a direct device is connected with an inverted one (or vice versa) and the two active layers absorption causes an incensement of the current.

An inverted configuration remarkably results in a more stable device that exhibits a longer life span [2.18-2.23]. Considering that our structure responds better in such configuration we will from now on in the experiment within this work consider only inverted organic solar cell devices.

---

\*\* HTL has also the function of electron blocking layer

†† ETL has also the function of hole blocking layer

In conclusion, there are many ways to improve the photon-electron conversion efficiency: we can modify the morphology of the active material, we can implement new and more promising low band gap materials capable of absorbing a wider spectrum of light. Basically these methods influence internal factors while we foresee great improvements within optical enhancements of organic solar cells. Because of standard devices geometry and materials thickness the blend cannot absorb  $1/3$  of the incident light in the range of the blend absorption spectrum. When we include the limitation of the active material band gap,  $2/3$  of the overall solar spectrum is currently not used.



# 3.

## **Optical enhancements**

This chapter will briefly treat the optimization of a solar cell. In particular we will describe how to enhance the photon flux in order to achieve the maximum efficiency and photocurrent generation. Then a more extensive treatment will be dedicated to sub wavelength devices optimization.

## 3.1 Optimizations of a solar cell

There are many approaches to enhance the performance of a solar cell. The internal factors<sup>‡‡</sup> of the performance are not directly treated in this work, we focus specifically on the external factors that influence the efficiency. These external factors are related to light management. Indeed photocurrent generation in a solar cell can be increased if the photon flux increases. The total photon flux used in the photocurrent generation process consists of the flux density incident on the solar cell minus the fraction reflected  $R(\lambda)$  and transmitted  $T(\lambda)$  in the case of transparent photovoltaics. There are different solutions valid for mostly all the PVs technologies that could be used to manage the light collection and its enhancement inside the active layer. We briefly summarize the main ones:

1) Solar collector: it is a system commonly based on reflective optics or Fresnel lenses, which increases the intake of photon flux in the solar cell. The main motivation is the reduction in system cost due to the reduction of the material used for the solar cell itself. In theory, concentration ratios of over 46000 are possible, but in practice the temperature increase and the resistance losses are limiting this theoretical ratio to few hundreds “sun” [3.1]. If we apply this system in “high junction”<sup>§§</sup> limit remarkably it could increase the efficiency of all the system to over 44% [1.9]. The idea behind this method for light control is very old [3.2], having been used by the ancient Greek scientist Archimedes, in the famous fight against the roman military ships as shown in the fresco [3.3] of **figure 3.1**.

---

<sup>‡‡</sup> Like charge recombination, crystallinity or temperature.

<sup>§§</sup> Where the sun light is absorbed typically by 3 or 4 junctions - each of them dedicated to different parts of the solar spectrum.



**Figure 3.1:** Fresco of one of the first, documented, solar collector where the sun light is collected and redirected on a ship [3.3].

2) Anti reflection coating (ARC): it is used to reduce the reflectivity of the solar cell (for an uncoated silicium R is about 30% in the visible range) to less than a few percent [3.4-3.8]. Commonly, ARCs are optimized for the absorption wavelength range of a specific solar cell. They are important also in transparent photovoltaics since they allow a higher amount of light to pass in the device.

3) Back side reflector: it consists of a mirror and/or diffractive element placed on the bottom side of the solar cell that allows light trapping inside the cell itself [3.9]. Light transmitted through the solar cell is reflected back by this mirror therefore increasing the total photon flux increasing the number of additional passes of light inside the active material. Internally reflected rays often increase the photon flux density.

4) Photon recycling: it is used in materials where the radiative recombination is an important loss mechanism. That is the case, for example, of

light trapping structure. Here the reabsorption of the emitted photon can enhance the photon density itself [3.10-3.11].

5) Up/down conversion: it consists in adding an extra layer of material that up/down converts (through absorption and re-emission of photons) a part of the incident radiation into different wavelength ranges. It is used for converting parts of the incident spectrum that normally are lost into wavelength ranges that can be absorbed by the solar cell. Until now a fabrication of a real device that exploits this possibility is far from being readily available, mainly due to the instability of the materials involved in the conversion. However, there is nowadays a big interest in this field [3.12].

For thin devices, where the lightweight and cost effectiveness is important [3.13], none of the optical management scheme described above can be implemented unless they demonstrate simplicity in the fabrication process and compatibility with the existing technologies. As an example a self-assembled technique could be one of the tools that could be implemented. We mainly focus on solutions 2, 3, 4 that we consider to be more suitable for thin films technologies. Moreover, we want in this work to enhance the photon flux in maximum 200 nm of active layer, which makes things far more problematic as described in the next paragraph.

We will describe here the principles of operation of an ARC. In an ARC, the first layer that accommodates the sun light into the device has a fundamental importance in light management. This part can indeed be used to enhance the light passing through the device. The reflectivity at the interface between two media is determined by their refractive indices, for instance air with refractive index  $n_0$  and a substrate with refractive index  $n_{AL}$ . In the simplest case of planar surfaces, at normal incidence, the light is reflected with probability:

$$R = \left( \frac{n_0 - n_{AL}}{n_0 + n_{AL}} \right)^2 \quad (3.1)$$

For air we can consider  $n_0=1$ , and since most materials used in photovoltaics have indices  $n_{AL}$  of 3 - 4 (2 for organic materials) at visible wavelengths, around 30-40% of the incident light is reflected at the interface. To reduce reflection, a thin layer of dielectric film with refractive index  $n_l$  satisfying  $n_0 < n_l < n_{AL}$ , can be applied to the surface of a device and serves as an ARC [3.1].

To achieve minimum reflection losses at a certain incident wavelength  $\lambda_0$ , the ARC should have an index  $n_l$  satisfying

$$n_l = \sqrt{n_0 \cdot n_{AL}} \quad (3.2)$$

and the thickness  $t$  determined by

$$t = \frac{\lambda_0}{4n_l} \quad (3.3)$$

However, although  $n_0=1$  is constant across the full solar spectrum, the refractive index  $n_{AL}$  typically varies significantly in this wavelength range. Therefore, index match at one wavelength does not mean high light admission over the entire solar spectrum. At the same time, the well-admitted light needs to be well absorbed by the active material. Keeping all the internal device parameters constant we are enhancing the EQE by allowing more photons to effectively reach the active photo conversion layer. This relation can best be seen with the following expression for short-circuit current density:

$$J_{SC} = q \cdot \int_{\lambda_{min}}^{\lambda_{max}} N_{ph}(\lambda) \cdot EQE(\lambda) d\lambda \quad (3.4)$$

where  $N_{ph}(\lambda)$  is the incident solar photon flux at that wavelength and  $q$  is the electron charge. Clearly,  $J_{SC}$  is influenced by an integrated effect of ARC and the active layer absorption over the whole solar spectrum.

We can further improve the ARC by adding one or more additional layers. The layer indices should increase consecutively from air ( $n_0$ ) to first coating ( $n_1$ ) to second coating ( $n_2$ ) and to active layer ( $n_{AL}$ ) [3.1], i.e.

$$n_0 < n_1 < n_2 < n_{AL} \quad (3.5)$$

For single incident wavelength, zero reflectivity is achieved when both films have quarter-wave thickness and satisfies:

$$\left(\frac{n_2}{n_1}\right)^2 = \left(\frac{n_{AL}}{n_0}\right) \quad (3.6)$$

More specific studies are needed to improve each of the PVs technology. Basically both an ARC and a back reflector solution are aimed at enhancing the light path inside the active material, while the photon recycling concept is more connected to the creation of an optical cavity that will keep photons inside the active material layer as much as possible. All these methods are studied to enhance the photon – electron

conversion efficiency by increasing the amount, and the permanence, of photons inside the active layer.

From now on we will focus on the special case of ultra-thin photovoltaics that have active layers lower than 200 nm and that consequently require special attention for the light management in the device.

## 3.2 Optical enhancements for ultra-thin film solar cells

We refer here to ultrathin film solar cell technologies, characterized by an active layer of thickness lower than 200 nm. This is due to intrinsic material properties, as in the case of organic materials [3.14-3.16]. However, thicknesses well below the diffraction limit imply only little absorption of the incident light that greatly limits the efficiency of the solar cell. In such devices the light management or photon control is fundamental to restore higher efficiencies. In such thin systems one can take advantage of different properties of light. Considering that the sun light has an optical coherence of about 1  $\mu\text{m}$  we can design our device to exploit optical interference effects. Knowing the electric field “E” and taking into account both real “n” and imaginary “k” refractive index of our materials we can calculate the light absorbed in any layer from its material properties and equation (3.7). Our final objective will be to calculate the light absorbed in the active layer in order to determine the total  $J_{SC}$ :

$$\eta_{ABS} = 2\pi c \int_{\lambda_{min}}^{\lambda_{max}} \int_V \frac{n(\lambda)k(\lambda)\epsilon_0}{\lambda} |E(r, \lambda)|^2 dV d\lambda. \quad (3.7)$$

Considering the photon flux and that the EQE has only the light absorption efficiency that depends on the wavelength we can rewrite the shot circuit current equation from equation (3.4) to equation (3.8):



$$J_{SC} = q \cdot \varphi \cdot 2\pi c \int_{\lambda_{min}}^{\lambda_{max}} \int_V N_{ph}(\lambda) \cdot \frac{n(\lambda)k(\lambda)\epsilon_0}{\lambda} |E(r, \lambda)|^2 dV d\lambda, \quad (3.8)$$

where  $\varphi$  is the part of the EQE, see equation 2.8, which does not depend on the wavelength. Equation (3.8) is important not only for the correct design of a photovoltaic solar cell, but also for testing the effective validity of an optical design. This allows us to have a direct comparison between the theory and the experimental data. For example with an EQE measurement setup, for testing the wavelength dependence validity, we can retrieve, point by point, all the current generated by our device at each wavelength. Alternatively, with the  $J/V$  characteristic, we can compare the measured total short circuit current, that in this case represents our evaluation parameter, with the one calculated using the equation 3.8.

Looking more in details at the light matter interaction we would like that all the photons were absorbed in the active layer material, but this is not possible intrinsically because the material thickness is much smaller than the incident wavelength and this mismatch, as observed before, is one of the causes of a not optimal photon-carrier conversion. To overcome this problem one might introduce a cavity resonator that enhances the probability of a photon to be absorbed in the active material. In this way a photon will stay “longer” in the active material volume (longer optical path) and the overall wave could fit in a more optimal way the volume of the active material. Typically optical cavities are designed for a specific wavelength and therefore for having high quality factor  $Q$ . This means that a beam will reflect a large number of times with little attenuation<sup>\*\*\*</sup>. In our case we are interested in low quality resonator that allows a broad spectrum of interaction, with the solar spectrum. Additionally our target would be to

---

<sup>\*\*\*</sup> the  $Q$  factor is, in the bandwidth formulation, the ratio between the resonance frequency  $\nu_0$  and the full width at half-maximum bandwidth  $\Delta\nu$  of the resonance:  $Q = \nu_0 / \Delta\nu$

confine [3.17] the electromagnetic field in a volume of the same order of magnitude as our active layer volume.

Many methods can be used to create a cavity [3.17], from simply having two mirrors or Bragg mirrors to the whispery gallery modes of a sphere or toroid. Photonic crystal cavities are also a good candidate thanks to their potentially reduced modal volume, but as drawback they work mostly for specific wavelength range. In chapter 5 we show how the combination of an ARC, an a-periodic 1D photonic crystal (multilayer, in order to have a broadband response) and two semi-transparent metal mirror, used also as electrodes, can enhance an OPV semi-transparent device to achieve a  $J_{SC}$  near to a non-transparent (opaque) device.

Moreover we could imagine how the confinement of light in a small volume could be associated, in a bigger scale, to the problem of coupling efficiently the radio frequencies to electric circuits. As we know this problem was solved by introducing the concept of antenna. In our case to be able to implement an optical antenna we need to scale down the problem by million times [3.18, 3.19], considering the size difference between optical and radio wavelengths<sup>†††</sup>. With optical antennas we would like to manipulate the sun light, by efficiently trap the light (far field, see chapter 4) in our thin film device, in order to maximize the number of photons, and their permanence, inside the active material. Such a system could also be associated with an optical resonator with a poor quality factor but with an incredibly small volume of interaction and relatively broad spectrum. An antenna can be designed for this scope and, as an example, placed in the upper layers, the ones that first accommodate the sun light. In this case we would like to maximize the light scattered into the active material. This is possible, in theory, because the scattering is connected with the antenna geometry. In the following Chapter 4 we will go deeper into this topic and we show how to effectively couple the light in an OPV device by manipulating the antenna design.

---

<sup>†††</sup> Radio wavelengths are in the range between 10 cm and 10 m, depending on the technology, while we harness the sun's energy mostly between 300 nm and 1800 nm.

# 4.

## **Optical nano-antenna improved OPVs**

Introducing plasmonic resonant scatterers in photovoltaic devices is a promising way to increase energy conversion efficiencies by trapping incoming light in ultra-thin solar cells. Colloidal plasmonic oligomers are obtained following a cost-effective self-assembly strategy and incorporated in organic-based cells produced using spin-coating techniques in ambient air conditions. We report an interesting increase of both external quantum efficiency and short circuit current for solar cells loaded with plasmonic oligomers compared with reference organic cells with and without isolated gold nanoparticles. Theoretical calculations demonstrate that the wavelength dependent EQE enhancement is a resonant process due to the increased scattering efficiency in plasmonic antennas allowed by a chemically controlled 1 nm nanogap. This method opens the way towards roll-to-roll fabrication of efficient plasmonic ultra-thin photovoltaic devices.

## 4.1 Optical antennas effects

The optical enhancement of a thin film is a critical factor knowing that typically the light that can be effectively absorbed is in the range between 400 nm and 600 nm, but, in order to achieve a good light harvesting device, we need to absorb light in the 300 nm - 1100 nm band interval. Violet and UV light is typically in the first few nm of the thin film while red and IR radiations pass through the device without being effectively absorbed. In the field of thin film photovoltaics, as mentioned in the first chapter, OPVs are promising opto-electronic devices to produce electricity because they are cost effective, possibly transparent and flexible [4.1–4.3]. Indeed they still suffer from weak electro-optical performances compared with inorganic thicker cells and thus require considerable efforts to increase their efficiency. Enhanced light matter interaction has been also the focus of many investigations over the last year, because it may solve severe challenges, such as the miniaturization of detectors thereby reducing the response time and space needed, increase their sensitivity, or, indeed, for more efficient and cheaper thin-film solar cells [4.1-4.5].

Increased power conversion can be obtained by enhancing light matter-interactions in the active material [4.4, 4.5]. In this context, optical antennas have attracted keen interest because the resonances supported either by nanoparticles or nano-structured electrodes are broadband and match well with the solar spectrum [4.6–4.8]. Most of the experimental work in organic cells shows evidence of indirect effects like exciton lifetime reduction [4.9], electrical device improvement [4.10–4.12], blend morphology modifications [4.13, 4.14], refractive index modification and other side effects like blend stabilization [4.15]. These effects produce mostly a spectral invariant enhancement contrary to what happens when direct resonant plasmonic effects are involved such as enhanced near-field and far-field scattering [4.16-4.20]. However, the efficiency of metallic particles in solar cells is hindered by the inherent ohmic losses of noble metals in the visible range. Large dielectric particles supporting lossless Mie

resonances are also promising for optimizing forward scattering processes [4.21, 4.22], but their diameters are typically of the order of  $\lambda/2$ . They are thus incompatible with organic solar cells requiring thin film geometries to avoid charge recombination.

In this chapter we will focus on designs that place the metallic optical antennas not in a direct contact with the blend but with the transporting layer. These designs limit the parasitic losses and the electrical performance deterioration. The design here presented is schematized in **Figure 4.1**: image (a) shows how placing the nano-antennas in the ETL (in the indirect configuration) could enhance the light path inside the device and the possibility, for the light itself, to be absorbed by the active material; image (b) shows how the light can excite a mode at the back electrode interface in order to enhance the light localization.

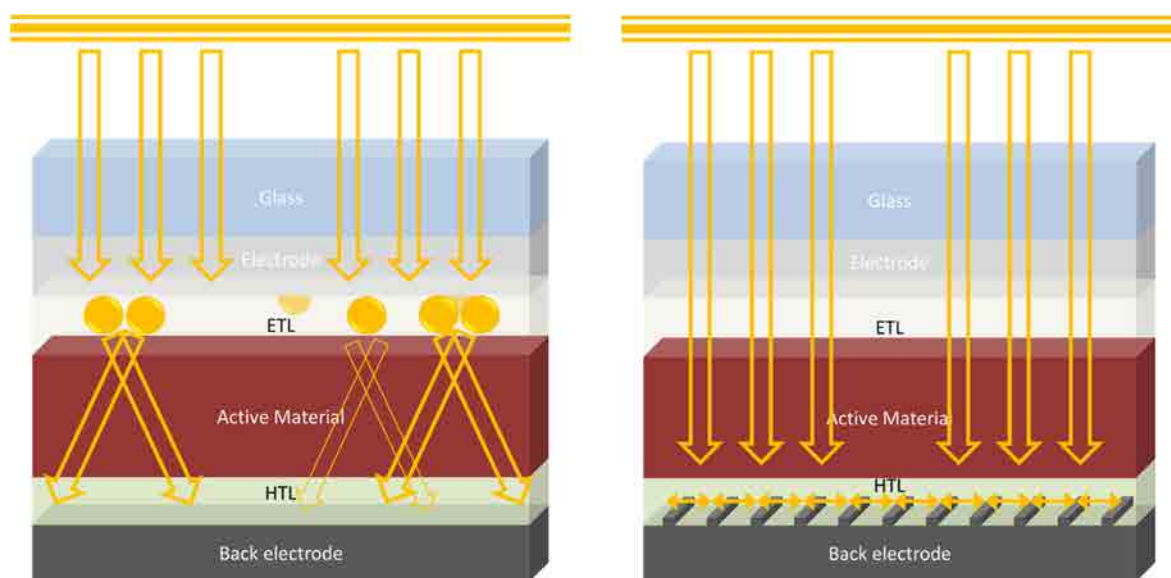


**Figure 4.1:** Optically enhanced OPVs schematic, (a) a surface plasmon resonance enhanced device with NPs located in a random configuration, (b) a surface plasmon polaritons enhanced device with a grating displaced in a periodic configuration.

In Figure 4.1 (a) we enhance and tune the absorption of the thin film containing organic molecules by the coupling to surface plasmon resonance. Here part of the light, from the

far field, is converted to the near field at a nanometer scale and then re-emitted again in the designed direction. In this case the nanoparticles are randomly deposited on the transparent electrode and are discussed in the next paragraph where, also, a new geometry is presented. In Figure 4.1 (b) we enhance and tune the active layer absorption by using the surface plasmon polaritons existing at metallic interfaces. This case is discussed in the last paragraph of this chapter (chapter 4, paragraph 3). Another option would be to cover the metallic nanoparticles with a dielectric material and then embed them in the active material, but this has the disadvantage of reducing the volume of the blend itself while it could directly harvest the near field. We also discuss the near field enhancement in more detail in the last paragraph of this chapter using an innovative design.

## 4.2. Self-assembled plasmonic nanogap antennas for organic photovoltaics (random configuration)

In this paragraph we focus on the scattering properties of nano-antennas and we introduce, for the first time, the design of a compact and highly performing solution. The scattering efficiencies of metallic nanoparticles can be improved by tuning their shape and size [4.23, 4.24] or by modifying their surrounding environment [4.25]. Because of the geometry constraints in thin film solar cells, we follow a scalable self-assembly method to form plasmonic oligomers that feature increased scattering cross-sections per particle in the visible range. We show that those antennas with a chemically controlled  $\sim 1$  nm gap can be introduced in organic based thin solar cells to enhance both the external quantum efficiency and short-circuit current. Cost-effective fabrication strategies are used for both the antennas and the ultra-thin film cells obtained using standard spin-coating techniques in ambient-air conditions. We underline the role played by the efficient light scattering of nanogap antennas compared to isolated nanoparticles, by comparing theoretical calculations to wavelength dependent EQE measurements.

### 4.2.1 Scattering efficiency

Metallic particles are resonant scatterers that are generally characterized by their extinction and scattering cross-sections [4.26, 4.27]. Such quantities are not intrinsic properties of particles and depend on the surrounding environment [4.25]. It is actually possible to increase the scattering and decrease the absorption of metallic nanoparticles by engineering their local environment, and more precisely by increasing the electric local density of states. In this section, we propose to modify the electromagnetic environment of a particle by simply approaching a second particle to form a dimer

antenna. Metallic nanogap antennas are very interesting plasmonic devices for increasing, in a very small volume confined in the nanogap, the electric local density of states allowing the fabrication of very fast single photon sources [4.28]. The coupling between the two particles has been well theorized by the quasi-static hybridization model and recently extended to non quasi-static dipolar cases [4.29, 4.30]. Depending on the conditions of illumination, the scattering efficiency can be either red- or blue-shifted [4.31].

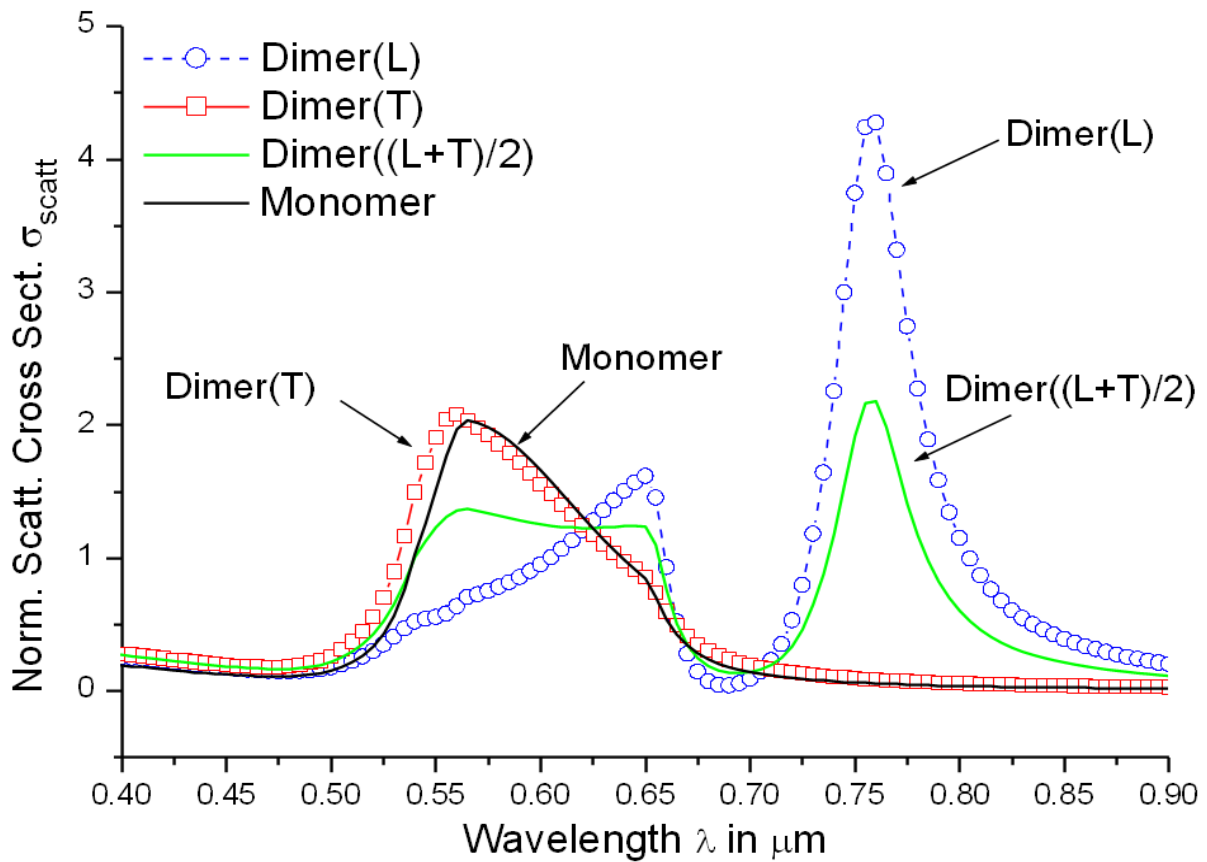


**Figure 4.2:** Scattering cross-section of a 40 nm gold particle with respect to the incident wavelength when considering a monomer (black line) or a dimer when the incident electric field is polarized along (L, blue dashed line+circles) or perpendicular (T, red line+squares) to the axis of the dimer. The average over both polarizations is represented by the green line. In the case of a dimer, this ratio is averaged over the incident polarization, the dimer is illuminated in normal incidence, i.e. the incident  $\mathbf{k}$  vector is normal to the dimer axis. These cross-sections are estimated per particle and normalized with respect to the particle surface area.



In this section, emphasis is placed on the increase of the scattering efficiency of a particle when coupled in a dimer. In order to quantify the increase of the scattering efficiency of particles when strongly coupled in a dimer, we plot in **Figure 4.2** the scattering cross-section of a particle either isolated (monomer) or assembled in a dimer surrounded by a homogeneous medium made of spin-coated TiO<sub>2</sub> anatase nanocrystals whose dispersive refractive index was measured by ellipsometry. The dimer is illuminated in normal incidence, i.e. the incident  $\mathbf{k}$  vector is normal to the dimer axis, with an incident electric field parallel or perpendicular to the axis. The refractive index of metal is taken from Palik [4.32]. The scattering efficiency of the monomer exhibits a resonant peak due to the excitation of the dipolar plasmonic mode on the particle around 560 nm. In the case of the dimer, the scattering efficiency strongly depends on the incident polarization. When the incident electric field is parallel to the dimer axis (T), the spectral feature of the scattering efficiency is very similar to the monomer while, when the incident electric field is normal to the dimer axis (L), the scattering efficiency features two strongly red-shifted peaks. The first peak around 770 nm is linked to the dipolar longitudinal bright mode and the second is a hybridized mode of quadrupolar order. The two peaks are separated by a well pronounced dip that is characteristic of the very small gap [4.33]. We can observe that, over a broad spectral range, the scattering efficiency of a particle can be strongly enhanced when coupled in a dimer. Figure 4.2 shows how small gold particles coupled in nanogap antennas in a high index medium, exhibit higher scattering than isolated AuNPs.

Additionally, plotting the field map in **Figure 4.3**, we can observe how the dimer is enhancing the electric field inside the active material and how the light is scattered in the forward and lateral direction. For the red part of the spectrum, right images, we observe how a monomer is ineffective while a dimer is exhibiting its maximum interaction with light.

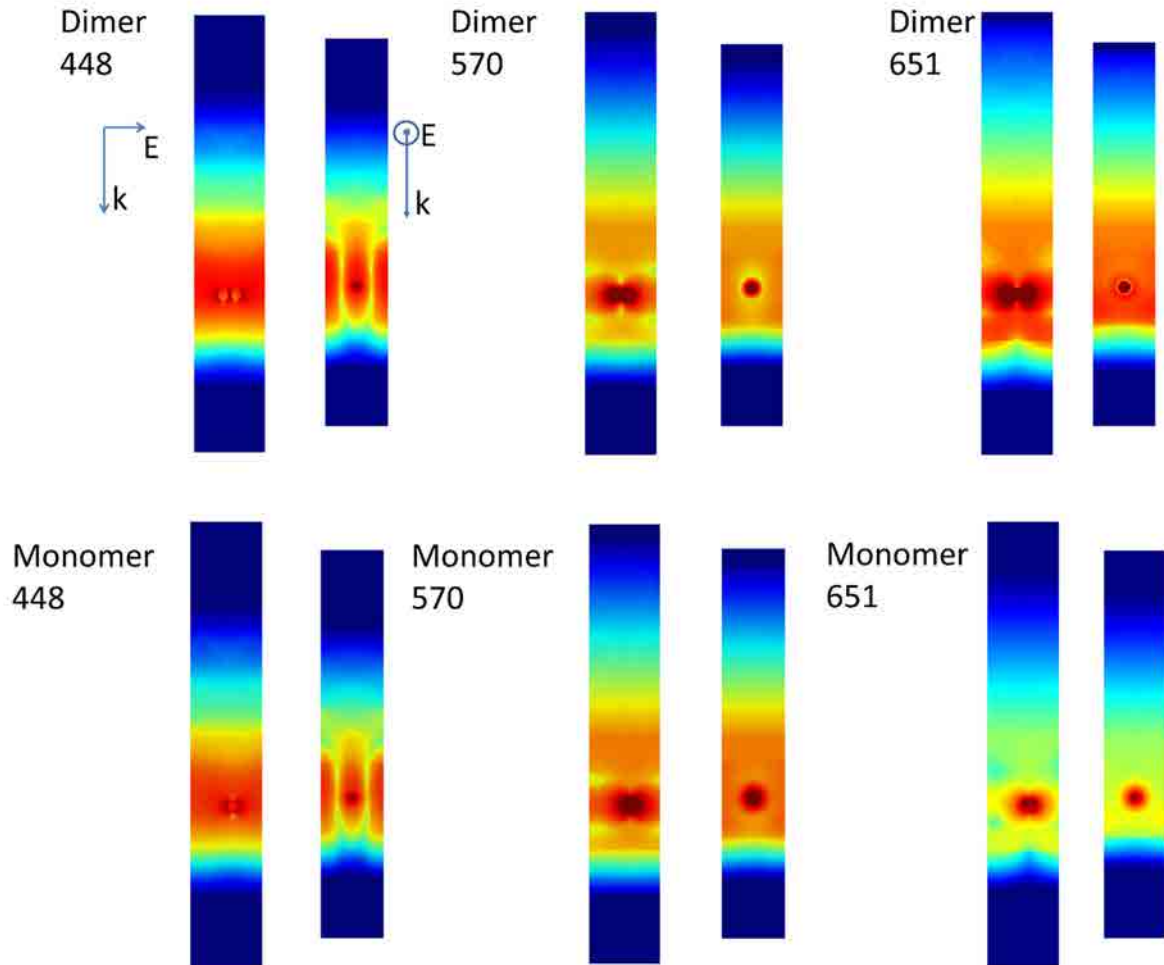


**Figure 4.3:** Electric field map for dimer and monomer for different wavelength, longitudinal and transversal polarizations.

## 4.2.2 Fabrication

Self-assembly strategies for plasmonic solar cells are attractive because they are cost-effective and lead to a random structuring that allows efficient light trapping effects over a large spectral range. All the processes used in this study are based on bottom-up approaches in air and at low temperatures (between 15 °C and 150 °C). Because of their low oxidation, we use gold nanoparticles [4.34–4.36] even if other materials like silver [4.13, 4.14, 4.37] should offer lower ohmic losses.

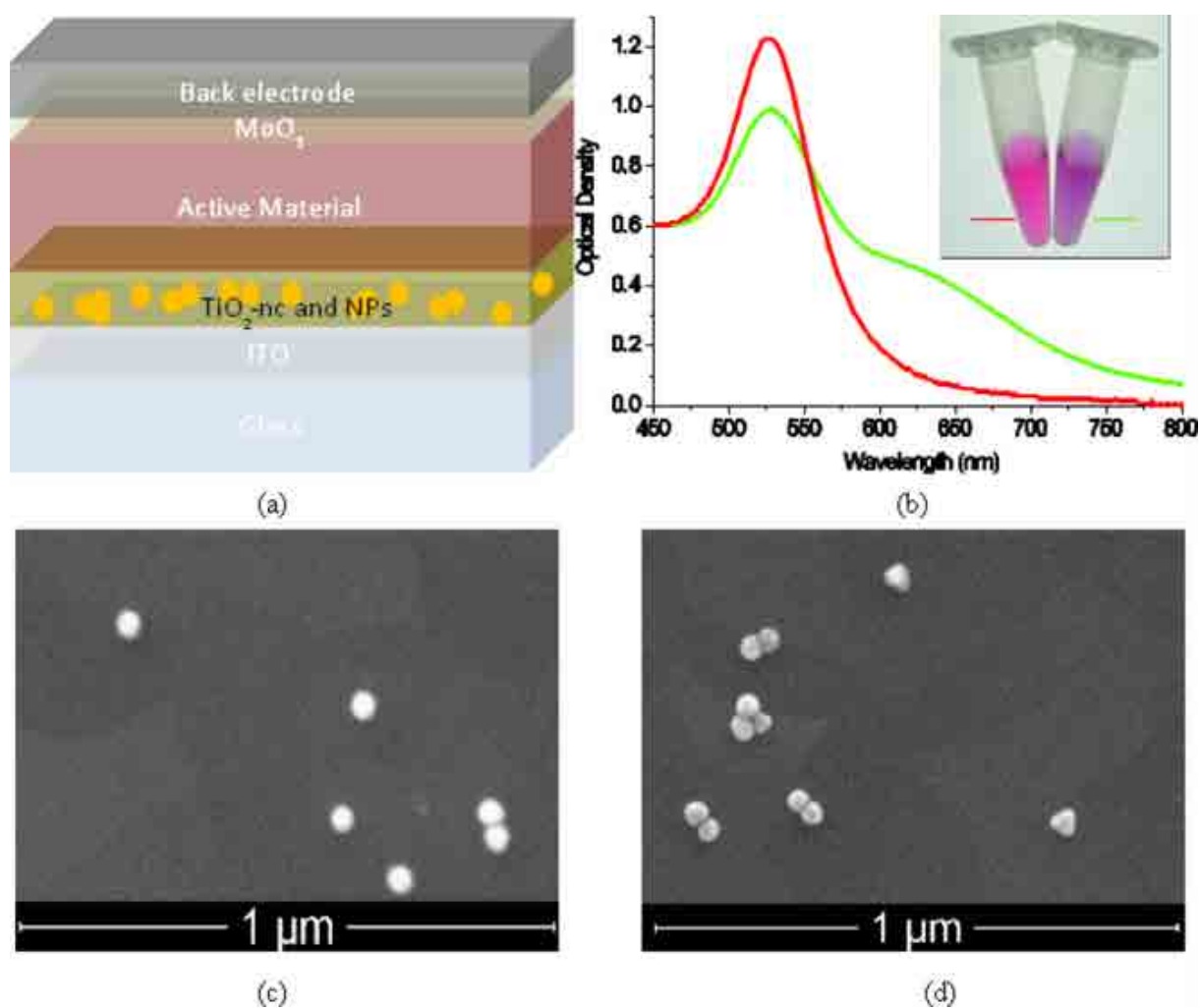


**Figure 4.4:** (a) Schematic representation of the fabricated and characterized solar cells. It is composed of a 100 nm thick Ag layer, a 10 nm thick MoO<sub>3</sub> layer, a 170 nm thick P3HT:PCBM layer, a 60 nm thick TiO<sub>2</sub> layer and a 120 nm thick ITO layer covered by a thick glass layer. (b) Optical density of two solutions of colloidal gold particles (2nM concentration of AuNPs). Red line: monomers of 40 nm gold particles, green line: same solution after performing the self-assembly method. (c-d) Self-assembled oligomers on an ITO substrate imaged by scanning electron microscopy. c: monomer solution, d: oligomer solution composed of monomers (70%), dimers (23%) and trimers (7%). 49% of the particles are coupled in oligomers.

The geometry of the organic solar cells is schematically depicted in **Figure 4.4a**. The self-assembly method is based on two ligand exchange steps in water: phosphine coated AuNPs are aggregated in dimers and trimers by adding small amounts of

dithiothreitol (DTT, to crosslink the particles) and sodium chloride (to screen electrostatic repulsion between particles) before the nanogap antennas are stabilized by adding an excess of thiolated ethylene glycol oligomers (to avoid the formation of larger groupings) [4.38]. The overall reaction process takes less than ten minutes and these small groupings are compatible with a thin film solar cell without modifying the device functionality. In order to evidence that self-assembly occurs, we measured the extinction spectra of two suspensions of 40 nm gold particles (2 nM concentrations), with and without the self-assembly process (see Figure 4.4b). The spectral features show the appearance of a second peak at 630 nm for the solution with DTT corresponding to the excitation of longitudinally coupled modes in dimers and trimers. The self-assembly process is also associated with a decrease of the main peak at 520 nm, corresponding to the dipolar plasmonic mode of the monomers and transverse modes in the oligomers. The difference between the extinction spectra of the 2 solutions can also be observed in the picture of the 2 samples (inset). Longitudinal resonances at 630 nm for dimers in water correspond to an interparticle gap of the order of 1-1.5 nm as estimated in Mie theory, in good agreement with the length of the molecular DTT linkers. We use a stable suspension containing gold nanoparticle (AuNP) monomers (70%), dimers (23%) and trimers (7%) meaning that 49% of the particles are coupled (as estimated in scanning electron microscopy, see Figure 4.4c and 4.3d). The particle density is estimated to be 12 NPs per  $\text{mm}^2$ .

Solar cell devices are fabricated using a glass substrate coated by a 120 nm thick layer of ITO. The gold nanoparticles are spin coated in 2 steps after UVO activation process and  $\text{N}_2$  gun cleaning. Both procedures are fundamental to link the plasmonic nanogap antennas to the ITO layer, as displayed in Figure 4.4 (c-d) obtained with a scanning electron microscope. Then a solution of anatase  $\text{TiO}_2$  nanocrystals is spincoated on top of the ITO and gold antennas, as a 60 nm ETL. The SEM images show that after the spin-coating process, the oligomers are horizontal with respect to the ITO surface. The thickness of the  $\text{TiO}_2$  layer being 50% larger than the diameter of the particles, the AuNPs will not be in direct contact with the active layer [4.39]. This high refractive index interlayer is aimed at scattering the incident light in the forward direction, but also at transporting the generated electrons to the ITO electrode. It typically provides higher

cell performances than sol-gel TiO<sub>2</sub> layers [4.40]. A 170 nm thick active layer made by a 1:1 P3HT:PCBM solution is spin coated on top of the TiO<sub>2</sub> layer. A 10 nm thin layer of MoO<sub>3</sub> is finally evaporated on the blend as HTL and a silver electrode is thermally deposited to complete the device.

### 4.2.3 Electro-optical characterization

The solar cell efficiencies are measured with a solar simulator implemented with an EQE measurement set-up. We can observe in **Figure 4.5** a broadband effect of the plasmonic nanogap antennas on the efficiency of the solar cell compared to a standard organic cell, and, more importantly, compared to the cell loaded with isolated AuNPs. This graph highlights the interest of plasmonic nanogap antennas for photovoltaic applications. However, the gain in EQE between cells loaded with monomers and oligomers solutions is more visible in the blue-green part of the spectrum ( $\lambda < 550\text{nm}$ ). The interest of oligomers over monomers almost disappears in the 525 nm - 600 nm range.

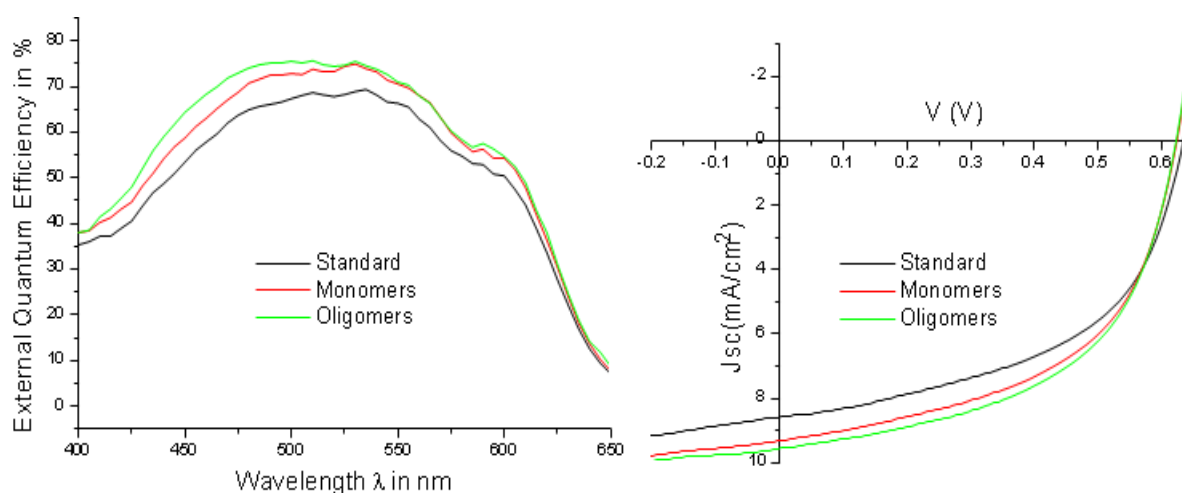


**Figure 4.5:** (a) Measurements of the External Quantum Efficiency with respect to the wavelength and (b) J-V curves for the three cells, standard (black line) and loaded with plasmonic monomers (red line) and oligomers (green line). External quantum efficiency in %, wavelength in nm, short circuit current  $J_{sc}$  in mA/cm<sup>2</sup> and tension in V.

The increased performance of the plasmonic cells, especially doped with oligomers, is further demonstrated in the I-V solar simulator measurements (see Figure 4.5b). The efficiencies of the three solar cell geometries are summarized in **Table 4.1**. Comparing the solar cell without nanoparticles and the one loaded with the plasmonic oligomers, we are able to reach an overall 11% increase in short circuit current, while for the monomers, the increase in short circuit current is only 8%. Overall, the solar cell efficiency goes from 2.8% with the standard organic cell to 3.2% with plasmonic oligomers.

**Table 4.1:** Solar cell characteristics measured from I-V solar simulator.

Solar cell device	FF [%]	V <sub>OC</sub> [mV]	J <sub>SC</sub> [mA/cm <sup>2</sup> ]	Eff [%]
Standard	51.8	632.8	8.58	2.8
Adding Single Au 40 nm NPs	52.8	622.3	9.29	3.0
Adding nanogap antennas	53.5	621.2	9.52	3.2

The efficiency of the pristine solar cells results from a thorough optimization process for devices fabricated in an ambient air environment and at room temperature (23 °C), compatible with roll-to-roll applications [4.40]. Let us stress that we used an inverted configuration that brings more stability compared with a direct solar cell device.

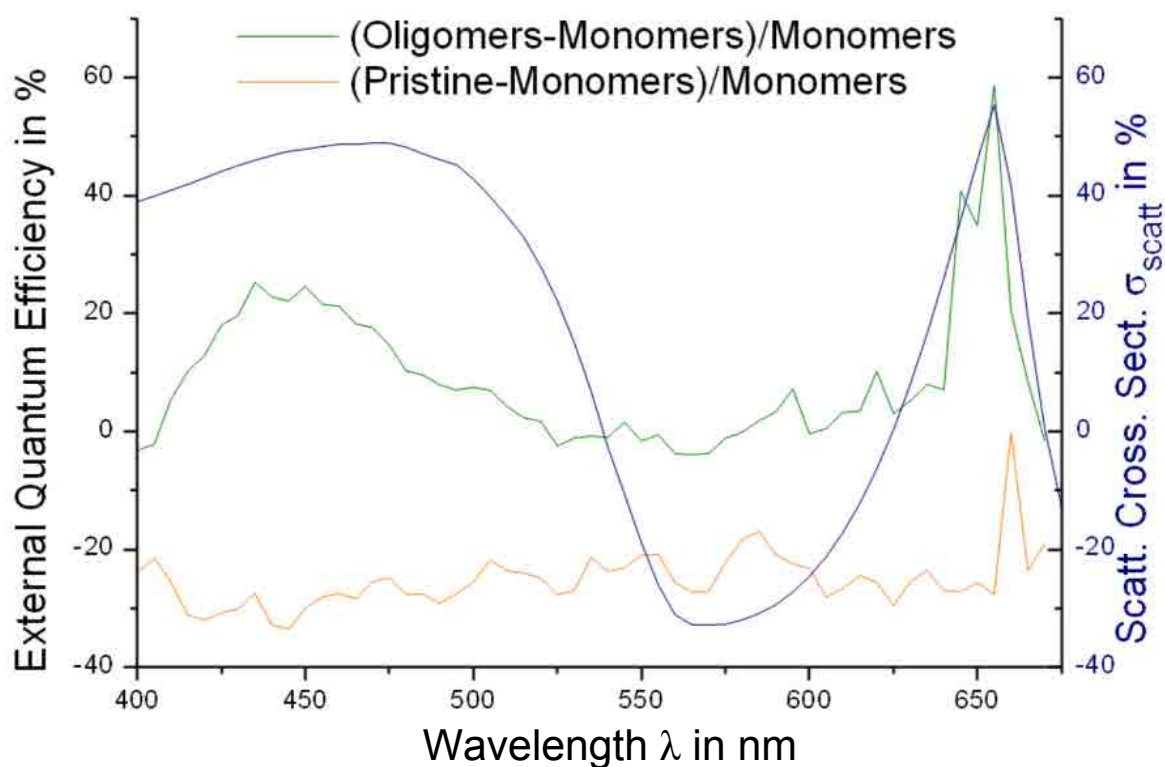


**Figure 4.6:** (Left scale) Relative difference in % of the EQE between the solar cells loaded with oligomers and monomers (green line) and between the pristine solar cells and the solar cells loaded with monomers (orange line) as a function of the wavelength. (Right scale, blue line) Normalized difference between the scattering cross-sections calculated with a dimer and a monomer. In the case of the dimer, the scattering cross-section is calculated per particle, and is averaged over both polarizations.

In order to better visualize the increased performance offered by plasmonic nanogap antennas compared with monomers, we plot in **Figure 4.6** the relative difference of EQE between cells loaded with oligomers and monomers as a function of the wavelength. This graph shows the large enhancement of the EQE function offered by plasmonic nanogap antennas. We report on the same graph the difference between the scattering cross-sections calculated with a dimer (averaged over the incident polarization) and a monomer. Very interestingly, we see that the two peaks and the dip in relative EQE are related respectively to an increase and a decrease of the scattering efficiency. In the 400 nm - 525 nm range, the increased performance is very broadband as it comes from

improved scattering from many high order multipolar modes in oligomers compared to monomers. The peak around 650 nm is narrow as it comes specifically from one quadrupolar mode observed on Figure 4.2. Around 550 nm, monomers are as efficient as oligomers as this frequency range corresponds both to the dipolar resonance of isolated AuNPs and to the transverse dipolar modes of coupled AuNPs. In this wavelength range the main effect is due to indirect plasmonic enhancements and the scattering efficiency is not high enough to be visualized in the EQE graph.

We also report in Figure 4.6 the relative difference of EQE between a pristine cell and one loaded with monomers as a function of the wavelength. In this case, the performance improvement of the cell containing AuNPs is due to indirect effects that have already been observed in the literature for similar device geometries [4.9-4.15]. It is important to note that these wavelength independent processes will be of comparable magnitude in cells containing isolated and self-assembled AuNPs, thanks to equivalent particle concentrations, and they cannot account for the wavelength dependent EQE improvement reported on Figure 4.6 for cells containing oligomers.

The results confirm the significant EQE improvement offered by oligomers in the spectral range where the EQE of the blend is maximal (450 nm - 550 nm) and indicates that they will be of high interest for lower bandgap materials thanks to their quadrupolar and dipolar longitudinal modes around 650 nm and 775 nm, respectively.

#### 4.2.4 Conclusion

In this section we demonstrated how coupled plasmonic scatterers can be incorporated in organic solar cells to improve their short circuit current by more than 12% [4.55] using low-tech, scalable approaches (colloidal self-assembly and standard spin-coating). Furthermore, by comparing theoretical calculations and EQE measurements, we demonstrate that coupling processes in nanogap antennas induce a wavelength specific enhancement linked to improved scattering. This allows us to circumvent the inherently weak scattering cross-sections of small AuNPs while staying compatible with thin film solar cell geometries. This approach, which is compatible with



roll-to-roll processing, could also be applied to lower bandgap active polymers by exploiting resonant longitudinal modes, in order to cover a broader part of the solar spectrum.

#### 4.2.5 Experimental Section

##### *Plasmonic oligomers assembly:*

The self-assembly of AuNP oligomers is described in detail elsewhere [4.38]. In brief, commercial citrate coated 40 nm AuNPs (BBInternational) are stabilized with bis (p - sulfonatophenyl) phenylphosphine (BSPP, Strem Chemicals), concentrated by centrifugation and stored at 4 °C for up to one year. A typical oligomer synthesis is performed using 1 pmol AuNPs in a 1mM DTT, 50 mM NaCl solution with a 100 mL reaction volume (milliQ water). After a 5 min incubation time, an excess (1 nmol) of thiolated, methyl-terminated ethylene glycol oligomer (Polypure) is added to stop the cross-linking effect of DTT by passivating the AuNPs. The NaCl concentration is reduced by adding water to a final volume of 1 mL before storing the oligomer suspension for several months. Electrophoresis can be used to separate dimers and trimers from isolated particles [4.38] but this purification step requires up to one hour and reduces considerably the yield and scalability of the fabrication process.

##### *Synthesis of TiO<sub>2</sub> nanoparticles:*

Nanocrystalline TiO<sub>2</sub> particles were synthesized using a procedure previously reported [4.42] and based on a sol-gel technique followed by growth under hydrothermal conditions [4.43]. This recipe was slightly modified in order to obtain a really fine particle size suspension (6 nm in average), which allowed forming very uniform TiO<sub>2</sub> films (that will cover completely the gold NPs and the ITO layer) [4.44].

*Solar cell fabrication:*

The fabrication of the devices, except for the last two steps which involve high vacuum deposition, was performed in ambient air conditions. A TiO<sub>2</sub> nanocrystalline film was deposited by spin-coating on top of ITO covered fused silica substrate and thermally annealed on a hotplate in air (150 °C 10 min) resulting in a 60 nm layer with a wide-band-gap of 3.2 eV [4.45] and a 4.1 eV work function. The active P3HT:PCBM (1:1 wt in oDCB) layer was deposited by spin-coating at room temperature (23 °C) and treated by solvent annealing during 5 min to obtain a 170 nm layer. Finally a 10 nm MoO<sub>3</sub> and 100 nm Ag layers were thermally evaporated to complete the devices. This is in an optically optimized inverted configuration for more stable and reliable measurements [4.42].

*Electro-Optical characterization:*

Electrical characterization (J-V measurements) was done employing an ABET technologies Sun 3000 solar simulator under AM1.5G conditions and a Keithley 2420 sourcemeter. The external quantum efficiency was measured with a solar cell spectral response measurement system from PC measurements, inc. model QEX10. The integration of the EQE spectra under the AM1.5G solar spectrum yields J<sub>SC</sub> values that are consistent with the ones obtained from the J-V measurements (reported in Table 4.1). Three different devices were tested for each configuration with comparable EQE and J-V behavior (the differences between the same configuration are below 2%).

*Numerical simulations:*

The scattering efficiencies were calculated with an in-house numerical code based on the Generalized Mie Theory [4.46]. Calculations were all performed with a multipole order N=30. The refractive index of gold was tabulated in published data [4.32]. The surrounding medium made of TiO<sub>2</sub> is considered as infinite and homogeneous. The refractive index was taken from ellipsometry measurements performed in ICFO on anatase TiO<sub>2</sub>.

## 4.3 Plasmonic enhanced solar absorbers (periodic configuration)

In the present paragraph we show that the absorption of a thin layer containing organic molecules can be enhanced and spectrally tuned by the coupling of surface plasmon resonances of metallic particles and surface plasmon polaritons existing at metallic interfaces. In this section we try to combine the two effects by implementing a plasmonic periodic structure just above the back electrode. We enhance light trapping and photocurrent by placing these properly designed nano-structures in a new low band gap active layer made of PBDTTT:PC71BM.

### 4.3.1 Electric field enhancements

Localized surface plasmon resonances (LSPR) of metallic particles turned out to be useful because of their sub-wavelength sized localization of light which creates hot-spots where the intensity is enhanced up to several orders of magnitude as well as because of their spectral tunability from the visible to the near infrared spectral range [4.47-4.49].

Additionally at metal-dielectric interfaces, surface plasmon polaritons (SPPs) feature a very strong confinement of the light perpendicular to the interface. These evanescent waves enhance the electromagnetic fields close to the surface which enables for (bio-) chemical sensing, enhances the nonlinear optical response, or increases the interaction of light with molecules. Recently, periodically nano-patterned metallic surfaces have been used to combine extended SPPs and LSPRs to improve the light extraction through metal films [4.50]. Hence, controlling the structure at the nanoscale can be used to tailor the optical response spectrally.

In this paragraph we combine those two effects and we demonstrate the potential of this approach to increase the light collection efficiency and their spectrally tunability in combination with a thin active layer made of PBDTTT: PC71BM. The latter one has been chosen because of its practical importance as a low bandgap blend layer in highly efficient organic solar cells. Its optimal thickness is about 90nm and it needs a strong light confinement scheme to fully express its photon harnessing capability. Furthermore, we analyzed the changes in the light absorption by measuring the generated photocurrent. Hence, such an analysis includes both, once again, the changes in the optical device properties as well as its consequences to the overall (electrical) device performance. To ensure the electrical operation, additional buffer layers on both sides of the active layer had to be included to facilitate the charge carrier separation as depicted in **Figure 4.7**. As electric field enhancement structure we use gold disks or islands (NIs) that are separated by a dielectric layer of SiO<sub>2</sub> from the Au surface to facilitate a strong light trapping inside the active layer. To avoid charge recombination and trapping we embed the structure in a thin layer of ZnO (ETL).

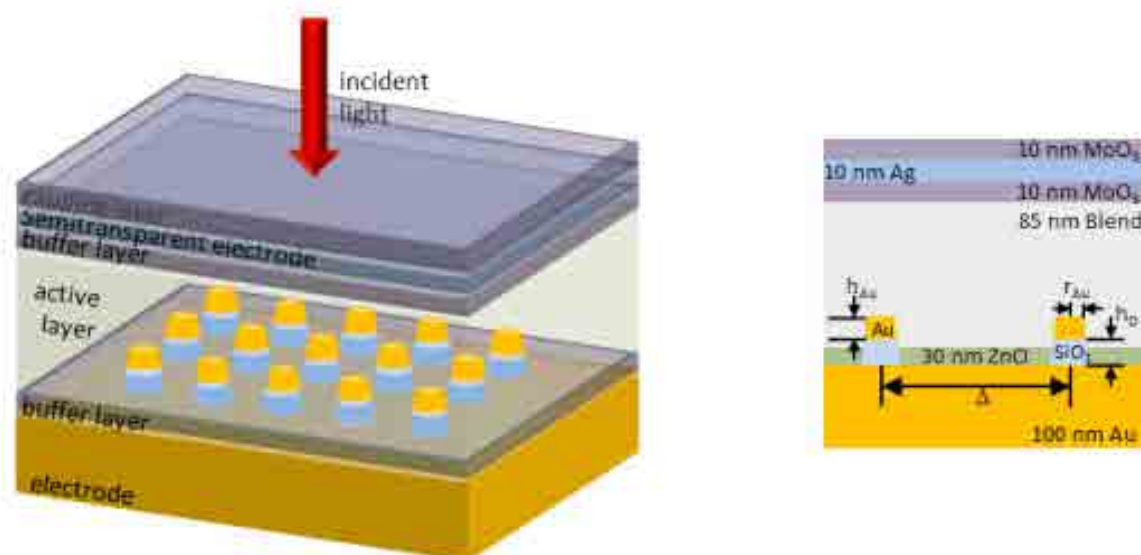


**Figure 4.7:** Schematic of the solar cell with nano-structuration: (a) 3D representation, (b) 2D representation with dimensions.

### 4.3.2 Theoretical analysis

The absorption of molecules in the active layer defines the device performance but the other materials used in the device also play an important role. The buffer layers or the semi-transparent electrode have their characteristic optical properties and together with the layer's thicknesses and textures may cause a strongly wavelength dependent response due to (guided) modes or, more generally, the local density of states [4.51]. This has been revealed by simulating the device performance with a commercial software and by taking the absorption in all the absorbing materials accordingly with equation 3.7. By plotting the absorption curves, **Figure 4.8**, we observe how the absorption in the blend and in the other materials is enhanced by the presence of the grating. We observe a good enhancement between 450 nm and 770 nm with a peak in the red part of the solar spectrum.

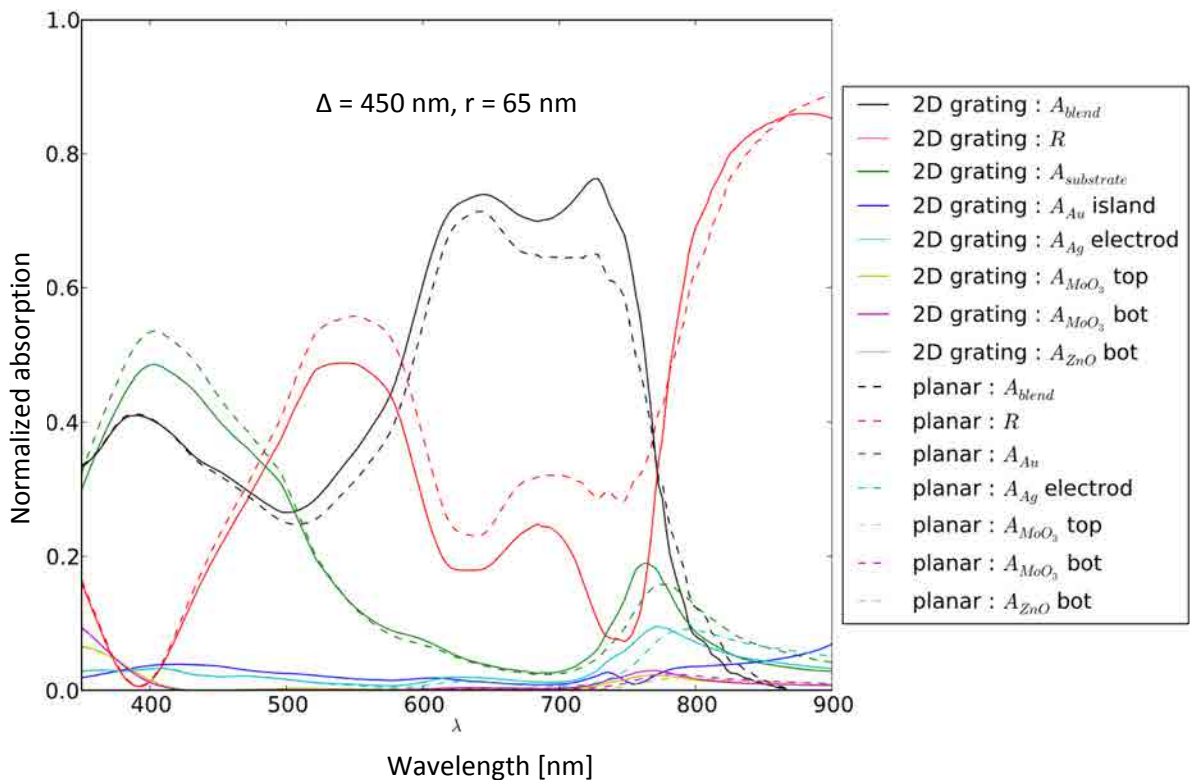


**Figure 4.8:** Electromagnetic field distribution and contribution of the individual layers to the absorption response. The comparison of the planar cell (dashed) to the nano-structured cell (solid) reveals that the reduced back reflection originates mainly from the enhanced absorption in the active blend layer.

A plot of the electric field map around the gold nano-island clarifies the light path in the device in **Figure 4.9**. We can observe how at 755 nm the light path is strongly modified by the presence of the NIs. The Pointing vector indicates that the light is scattered in the forward and laterally diffused while the colour map shows the electric field enhancement around the island.

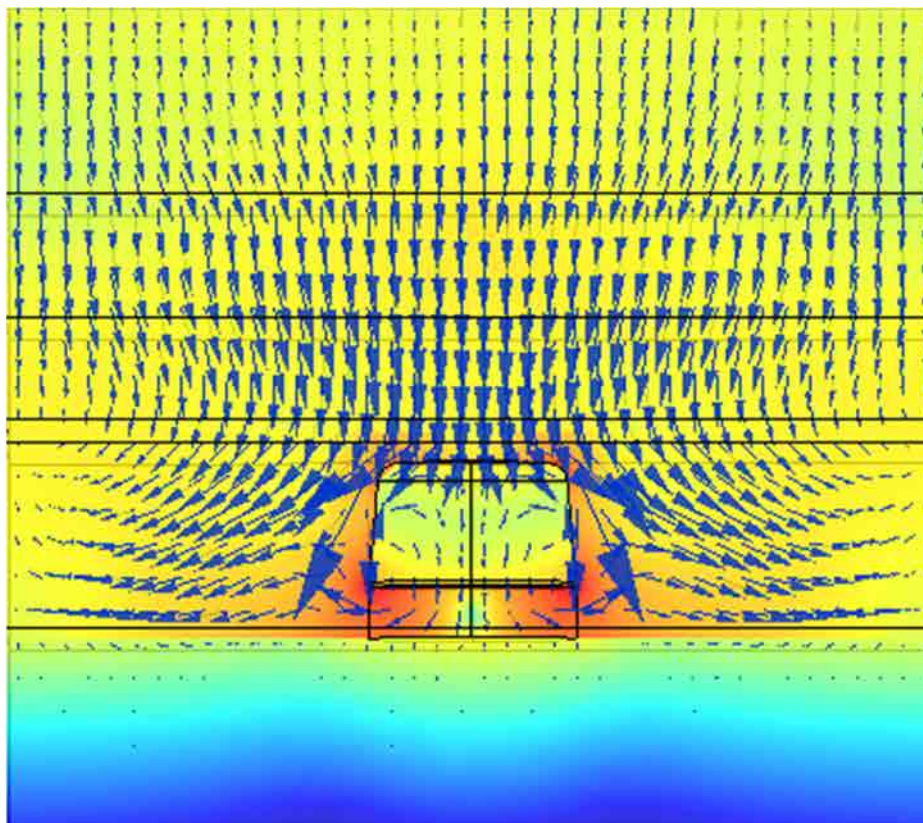


**Figure 4.9:** The strong near-field interaction between the metallic particle and the substrate increases the electromagnetic field inside the active layer.

As shown in Figure 4.8, the plasmon resonance is located near 750 nm. Here we observe that the difference between  $A_{\text{blend}}$  of the grating and  $A_{\text{blend}}$  of the planar is maximal. This resonance is influenced from the other layers and depending on the NIs geometry the absorptions of such layers are modified. Two cases were demonstrated experimentally for gold NIs of 30 nm height on a SiO<sub>2</sub> spacer of 25 nm. The first structure was

developed with a period ( $\Delta$ ) of 450 nm and 65 nm NIs radius ( $r$ ). The second had a period of 550 nm and 95 nm NIs radius. As mentioned, the geometry of the nano-island enhances the absorption of the active layer in this region but also the parasitic absorption of the other layers. However, the consequent high scattering produced by the nano-structure, especially in the blue, added to the relatively low parasitic absorption enabled an important enhancement in the photon absorption by the active layer.

### 4.3.3 Device fabrication

The devices were experimentally implemented in the inverted structure Au/nano-structure/ZnO/PBDTTT-C:PC<sub>71</sub>BM/MoO<sub>3</sub>(I)/Ag/MoO<sub>3</sub>(II) on top of fused silica substrates as sketched in Fig 4.6. The back electrode was a 100 nm thick Au layer deposited on a previously cleaned fused silica substrate followed by the evaporation of a 1-nm-thin Ti layer to facilitate the adhesion of 40 nm thick SiO<sub>2</sub>, followed by a second 1-nm-thin Ti layer to facilitate the adhesion of 30-nm-thick Au layer. The gold-silica NIs have been fabricated using negative-tone electron beam sensitive resist to structure 9 mm<sup>2</sup> sized areas. After the selectively etching of the unprotected gold and silica using an argon-plasma all the way down till reaching the bottom gold electrode, the resist was removed using oxygen plasma. The nano-structured surface was inspected using secondary electron microscopy to measure the device dimensions. If the nanostructure is too dense this process can last several hours and can give a substrate with poor wettability compromising the correct functioning of a device.

On top of the combined electrode Au+NIs the rest of the photovoltaic device was developed. That included a 30 nm thick ZnO used as electron transporting layer and obtained by sol-gel [4.52], a 85 nm active layer of PBDTTT:PC<sub>71</sub>BM processed according to the reference [4.53] in an inert atmosphere, a 10 nm MoO<sub>3</sub> deposited by thermal evaporation at 1 Å s<sup>-1</sup>, a 10 nm top semi-transparent Ag electrode deposited at 6 Å s<sup>-1</sup> and -15 °C and a final 10 nm MoO<sub>3</sub> used as a protection for the Ag layer. The high quality of the electrode, made at low temperature to avoid atoms diffusion in the other layers [4.54], guarantee a free post-thermal annealing device. All the thickness of

the layers were measured by tapping AFM and the shape of the NIs was transferred into the whole device as shown by the AFM profile in **Figure 4.10**.

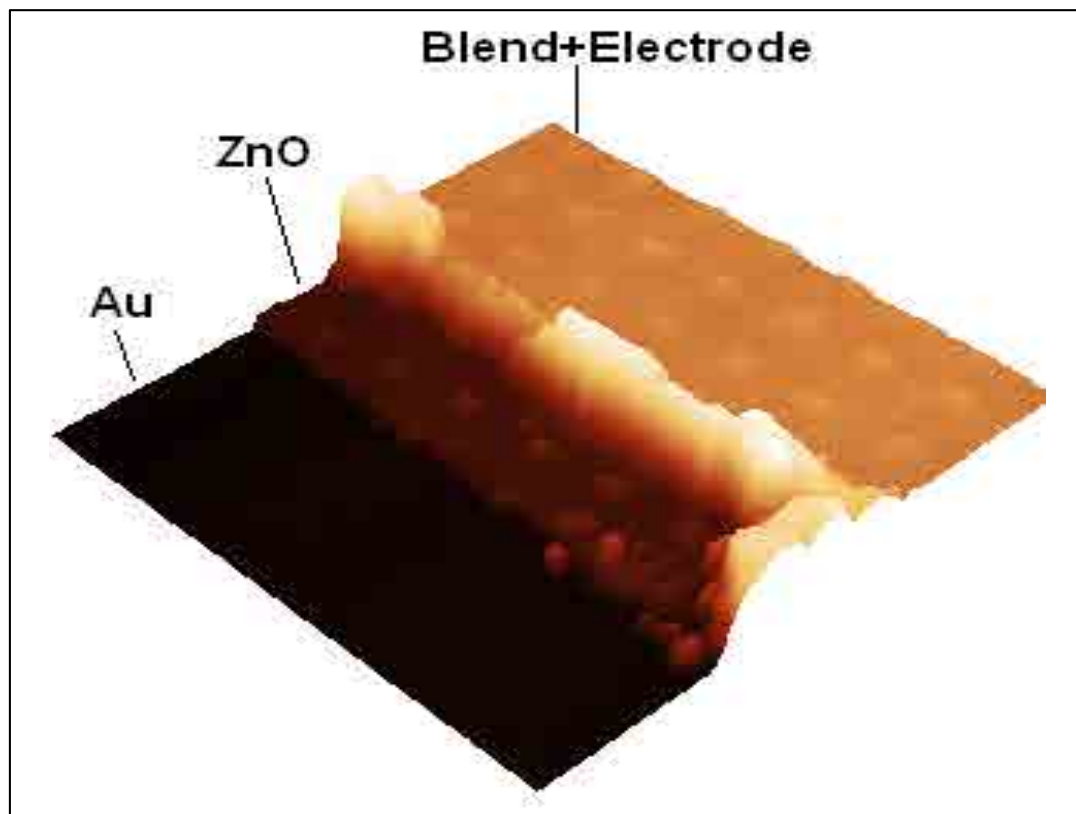


**Figure 4.10:** AFM image of the nano-structure.

#### 4.3.4 Results and discussion

The fabricated devices were electrically characterized immediately after fabrication by determining the external quantum efficiency as a function of the incident wavelength by using a solar cell spectral response measurement system with a 10 nm step resolution. The resulting measurements are presented in **Figure 4.11** (a) and (c). As predicted by the numerical analysis<sup>†††</sup> shown in Figure 4.11 (b) and (d), the enhancement was found mainly in the visible spectral range peaking around the orange-red spectral range from 580 nm to 720 nm.

---

<sup>†††</sup> We use equation (3.8) for this scope.



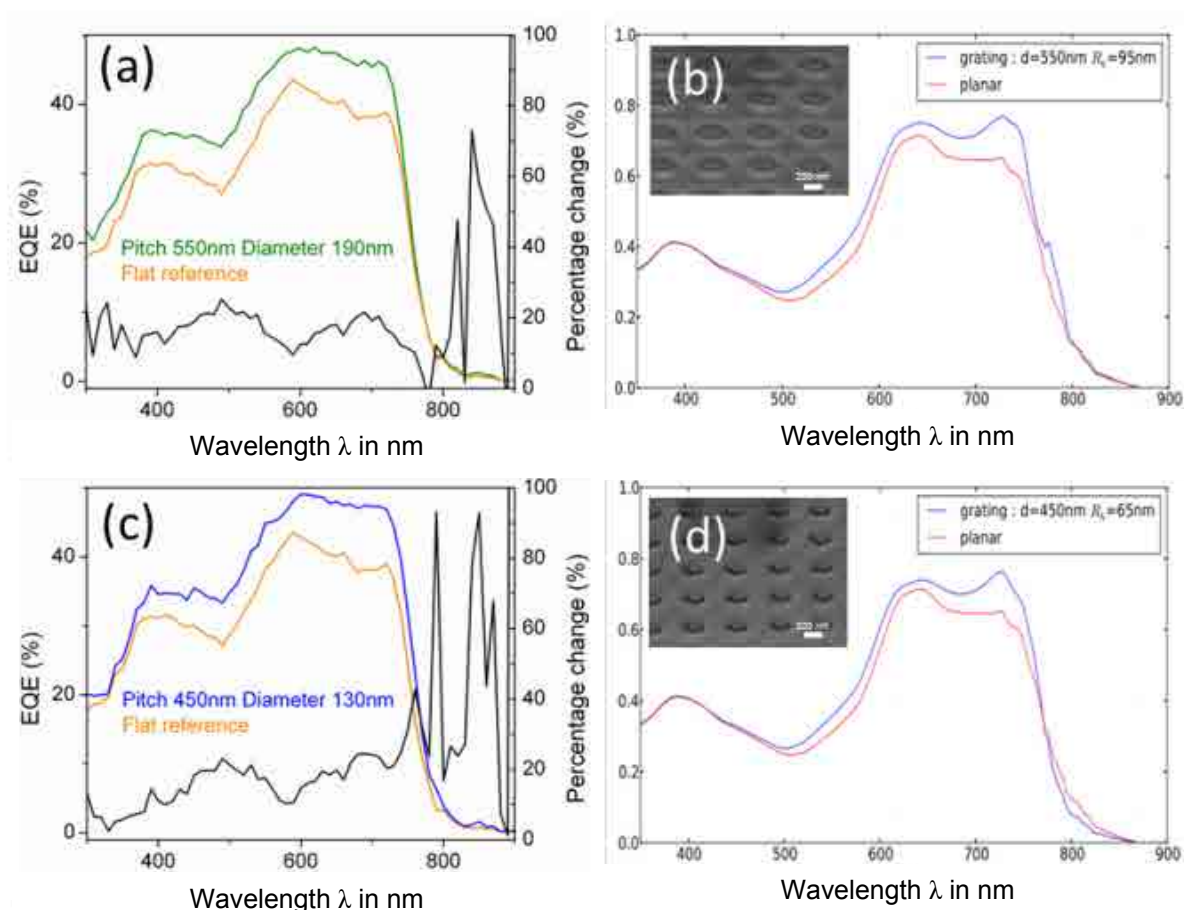


**Figure 4.11:** The EQE is enhanced for the different nano-structures. The measured data (left) are in close agreement with the expected theoretical predictions (right). The SEM images shown as an inset in (b) and (d) have been taken after the lithography under 45-degree tilted angle-of incidence.

The black curves in Figure 4.11 (a) and (c) represent the relative increase of the EQE. Besides the overall increase in the visible spectral region, strongly increased values of the EQE in the near-infrared spectral range have been found. Their electrical response of the nano-structured device is increased up to 20% which was expected in the case of  $r = 65$  and  $\Delta = 450$  nm. This fact is in good agreement with the theory which demonstrates that the near (hot spots) and far field (scattering) effects of the nano-islands are improving the device spectral response. In the case of  $r = 95$  and  $\Delta = 550$  nm we observe an overall enhancement in the order of 10%, but we can not observe the plasmonic resonance peak as expected from the theory. This can be due to an inhomogeneous grating or to a plasmonic resonance more redshifted than expected.

In conclusion, we demonstrated that the coupling of localized surface plasmon resonance of metallic particles to surface plasmon polaritons at metallic interfaces can be used to increase the light absorption and conversion to electrical charges. The coupling can be controlled and tuned with the lateral and out of plane separation and the size of the nanoparticles and allows for a spectral tuning of the active layer absorption, thereby increasing the efficiency within certain wavelength range in thin-film devices.

# 5.

## **Semi-transparent and Optical cavity enhanced OPVs**

Transparency is a key factor for BIPV solutions, because solar facades are commonly used in solar architecture or bioclimatic architecture for reducing energy consumption. In this work we present a qualitative method to evaluate the visible transparency. We then apply the method to our new concept of optically enhanced multilayer transparent organic solar cell.

## 5.1 Transparent solar facades

A growing number of systems need the sun radiation as a fundamental component. From agriculture to water management we need to accurately use the sun energy and part of its spectrum. In for example agriculture we are able to trap solar radiation in order to make the plants grow in a controlled environment. In water management we can block solar radiation that will compromise [5.1] the drinkability of the water, as well as use a part of the solar energy to sterilize water. Throughout history glass has been used as an universal solar façade because it is transparent over the entire solar spectrum, blocking only UV radiation as well as heat. Ergo glass is an ideal material for creating an artificial greenhouse effect in a building, and for further benefit, the part of the solar spectrum that is not visible and has a weak heat power can be used to produce electricity.

### 5.1.1 Transparent solutions

One of the biggest step towards reducing the consumption of fossil fuels is the introduction of a series of promising designs for increasing energy efficiency in buildings. Historically one of the most used system is the solar façade. To effectively use such solution it is fundamental to take into account the buildings orientation and sun inclination. With recent technological developments it is possible to use solar energy also in areas where the solar radiation is not optimal or where buildings are not correctly orientated. There are studies on opaque solar facades [5.2], but this kind of system cannot directly transform the solar radiation into heat gain in buildings, whereas transparent, semi-transparent and translucent solar facade systems are able to do so [5.3]. Those systems fall into two categories: passive and active solar facades. They are commonly considered building integratable and often combine thermal and photovoltaic effects.

In the passive systems we find the naturally ventilated transparent façade that uses wind pressure and/or natural convection to heat or cool down the building. The design phase is essential in the passive systems. To be fully efficient they need to be planned with the construction of the building. Trying to implement them in already built constructions will rarely reach maximum potential.

In the active solar façade systems we can find mechanically ventilated solutions that can heat or cool the environment suiting the users needs. Amongst active systems are semi-transparent building integrated photovoltaic (STBIPV) that allows the sun to pass through the façade utilizing a part of the solar spectrum for electricity production via photovoltaic effect. This production of electricity can be obtained by using a semi-transparent OPV (STBIOPV) device, see **figure 5.1**, which allows an appropriate amount of visible light into the building. It is fundamental for a healthy work environment and basic life quality to have visible light entering. The different perceptions of “life quality” have in relation to colour theory led to different points of view on how to implement “visible transparency”. In this work we will present what we think is the most suitable system for visible transparency or luminosity quantification [5.4] that fits the photovoltaic design procedure.

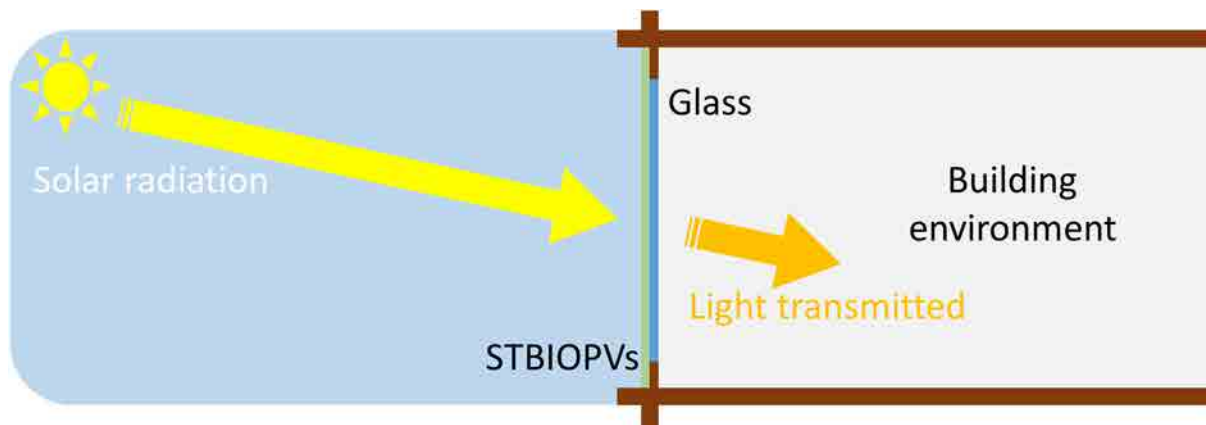


**Figure 5.1:** Schematic diagram of semi-transparent building-integrated organic photovoltaic (STBIOPV).

## 5.1.2 Visible transparency

The brightness of an object, as perceived by the human eye, is quantified by the luminosity  $L$ . It is also called “visible light transmission” (VLT) or “photopic transmission” and corresponds to the integrated transmission spectrum of an object or device  $T(\lambda)$  over the whole visible spectrum, weighted by the photopic spectral response of a typical human eye  $V(\lambda)$  and the spectrum of the illuminant. For daylight illumination, the CIE D65( $\lambda$ ) is used as the illuminant. The spectrum of such illuminant, shown in figure 5.1, is very close to the black-body radiation with a color temperature of 6500K.

To calculate the luminosity of a solar device, which in application on a transparent window can be thought of as filter, one simply calculates the area under the transmission spectrum curve weighted by the Photopic Curve  $V(\lambda)$ , shown and the illuminant spectrum  $I(\lambda)$  both in **figure 5.2**, and normalize by the area under the product of photopic curve and illuminant spectrum as in equation 5.1.

$$L = \frac{\int T(\lambda)V(\lambda)D65(\lambda)d\lambda}{\int V(\lambda)D65(\lambda)d\lambda} \quad (5.1)$$

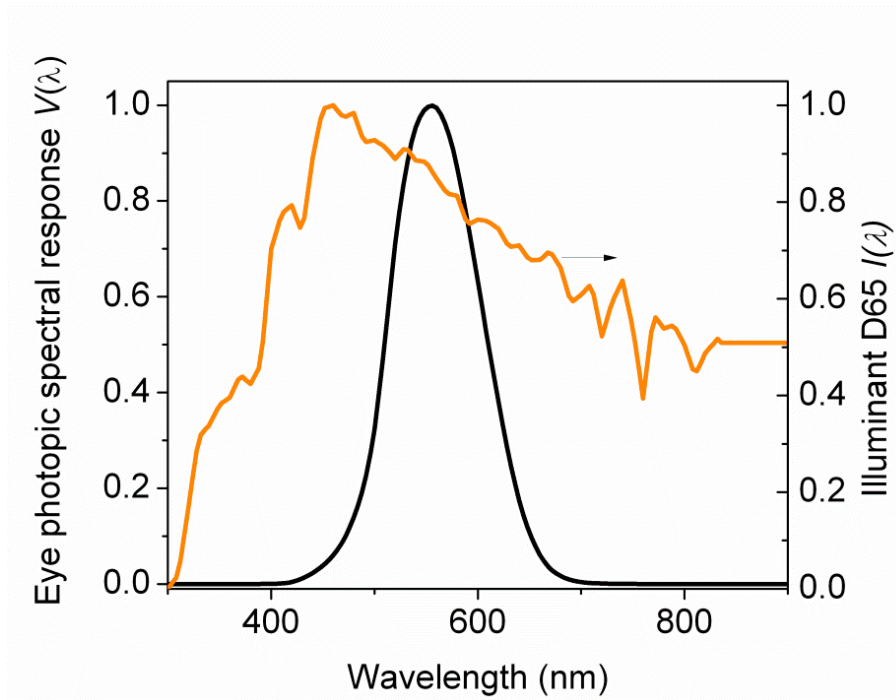


**Figure 5.2:** Human eye and illumination information for the analyzed semi-transparent devices: Illuminant D65 (solid orange line) and human photopic spectral response (black line) [5.4].

In the next paragraph we show how to enhance the solar cell performance of a semi-transparent solar cell while keeping a good visible transparency for BIPV applications.

## 5.2 Enhanced Light Harvesting in Semi-transparent Organic Solar Cells using an Optical Cavity configuration

We introduced a new solar cell design in order to fabricate transparent solar cell devices with 20% of luminosity and a power conversion efficiency near to a standard opaque solar cell. These results are obtained using the combination of different structures that contribute to the optical enhancement of the device.

### 5.2.1 Semi-transparent OPVs

Recent developments in the field of organic photovoltaics have demonstrated the enormous potential of such technology for integration into renewable energy generation elements that require a certain degree of transparency. It has been experimentally shown that 30% transparent polymer solar cells may exhibit power conversion efficiencies above 5% in single junction devices [5.5] and above 7 % for tandem ones [5.6]. Typically, in an organic cell the active material layer is sufficiently thin to present visible transparencies higher than 50%. However, semi-transparency in organic cells can only be achieved when the opaque back metal contact is replaced by a semi-transparent thin electrode [5.5-5.22]. The use of two, front and back, semi-transparent electrodes automatically leads to a decrease in the effectiveness of the light harvesting capacity of the solar cell [5.5,5.8-5.27]. Several approaches have been considered to partially recover such lost light harvesting effectiveness at those wavelengths invisible to the eye. Recently, using a non-periodic one-dimensional photonic crystal the short circuit current ( $J_{sc}$ ) of a semi-transparent cell was brought close to 97% the one from the corresponding opaque cell. The multilayer dielectric structure (MLD) was designed ad hoc to enhance the external quantum efficiency at the near IR and UV wavelengths while maintaining transparency in the visible [5.5]. The combined use of an anti-reflection coating (ARC)



on the front of the cell and a Bragg reflector on the back was also implemented to reach semi-transparent cells performing at 71% of the corresponding opaque one [5.22].

### 5.2.1 New design and fabrication for semi-transparent OPVs

In the current paragraph we propose to enclose the active material layer in between two metal electrodes that form an optical cavity designed to optimize photon trapping inside the cell. At the same time such electrodes are kept sufficiently thin to ensure a visible transparency higher than 20%. To increase near IR light trapping, while maintaining transparency in the visible, an ARC is deposited on top of the front metal contact while a non-periodic MLD is inserted in between the back metal contact and the substrate. The optimal layer configuration for such MLD was designed specifically for the cell architecture under study. With a device architecture as the one shown schematically in **Figure 5.3**, we achieved semi-transparent cells which PCE was 5.3%, corresponding to 90% the PCE of the opaque cell. The visible transparency of such cells differed little from the semi-transparent cell which did not include the MLD, a cell that achieved a PCE of only 3.0%.

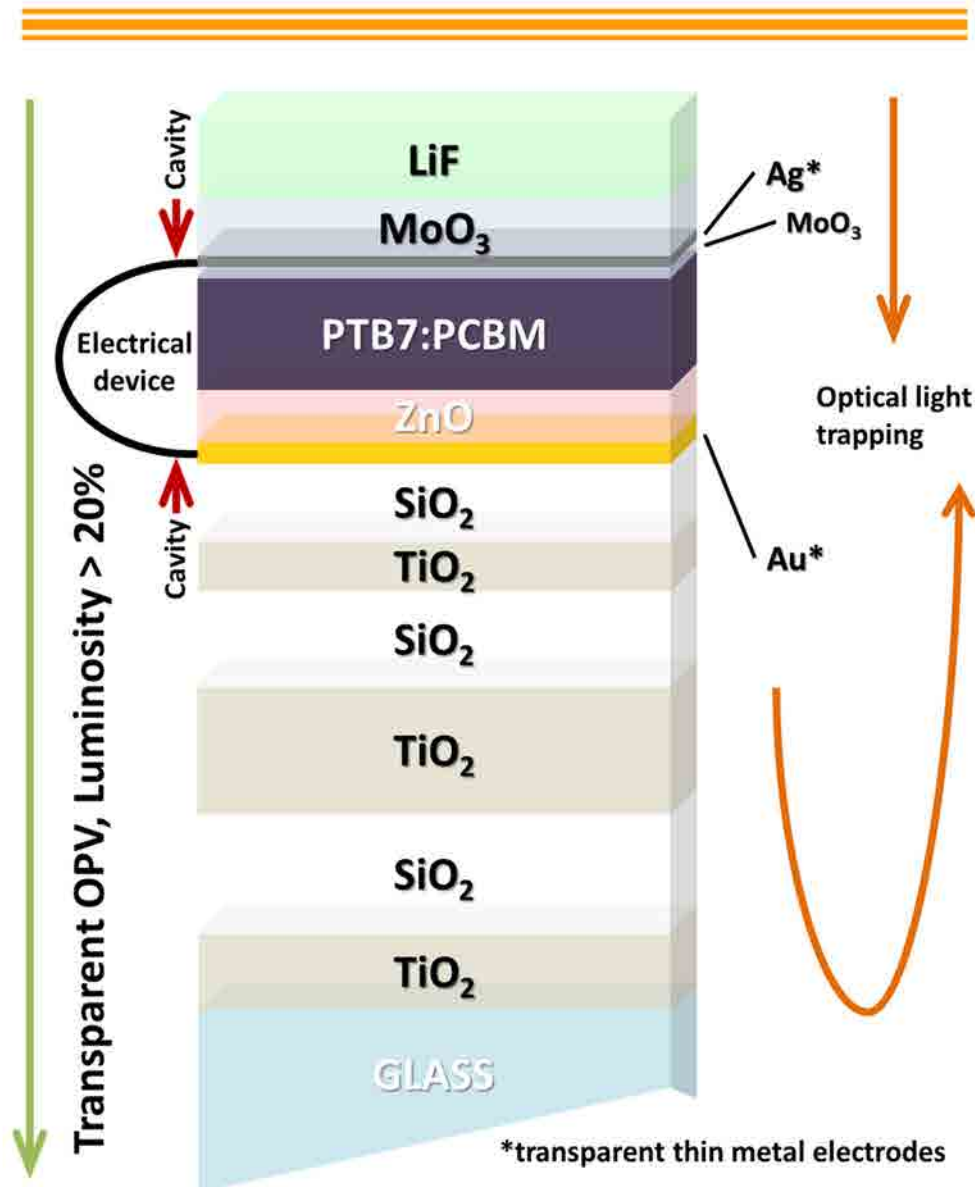


**Figure 5.3:** Schematic illustration of the semi-transparent device cell architecture incorporating the MLD between the glass and the Au thin metal electrode and ARC above the Ag thin metal electrode. Near IR light is partially confined in the active layer (PTB7:PCBM) while the luminosity or visible transparency for the device is kept above 20 %.

We fabricated two different types of semi-transparent cells (STC1 & STC2) and an opaque cell, which we used as the reference cell to evaluate the PV performance of the semi-transparent cells. The opaque cell was in an inverted configuration with the

following architecture: as active material we used 90 nm of a PTB7:PC71BM blend, the bottom electrode was an opaque layer of 120 nm of Au and the top electrode was a semi-transparent layer of 10 nm of Ag. As ETL we used a layer of ZnO and as HTL a layer of MoO<sub>3</sub>. On top of the Ag electrode we deposited a two-layer ARC made of MoO<sub>3</sub> and LiF. For the semi-transparent devices we used the exact same architecture except that the Au electrode was thinned down to 13 nm. We used the same active material and blocking layers as in the opaque cell, while we used two different configurations for the external light harvesting structure. As seen in Figure 5.3, for STC1 we incorporated in between the Au electrode and the substrate a six-layer 1-dimensional MLD made, alternatively, of TiO<sub>2</sub> and SiO<sub>2</sub>. This structure was designed to maximize the current while keeping the overall luminosity of the solar cell above 20%. STC2 did not incorporate any MLD. Both, STC1 and STC2 incorporated the same ARC on top of the Ag electrode we used for the opaque one. The metallic character of both electrodes, ensured a certain degree of light tapping for STC1 and STC2, however, as we shall see below light trapping in STC2 was rather limited.

### 5.2.2 Electro-optical characterization

As shown in **Figure 5.4**, the transparency of STC1 relative to STC2 increased in the 430 nm - 510 nm range and in the blue part of the spectrum while experiencing a slight reduction in the rest of the visible spectrum. STC1 exhibited a considerable reduction in transparency beyond 600 nm up to 770 nm. The overall luminosity was similar when comparing STC1 with STC2, however, as seen in Figure 5.4, the combination of the MLD and ARC to localize light in the near IR can also enhanced transparency in the blue part of the spectrum. Consequently STC1 exhibits two peaks in transparency around 390 nm and 475 nm.

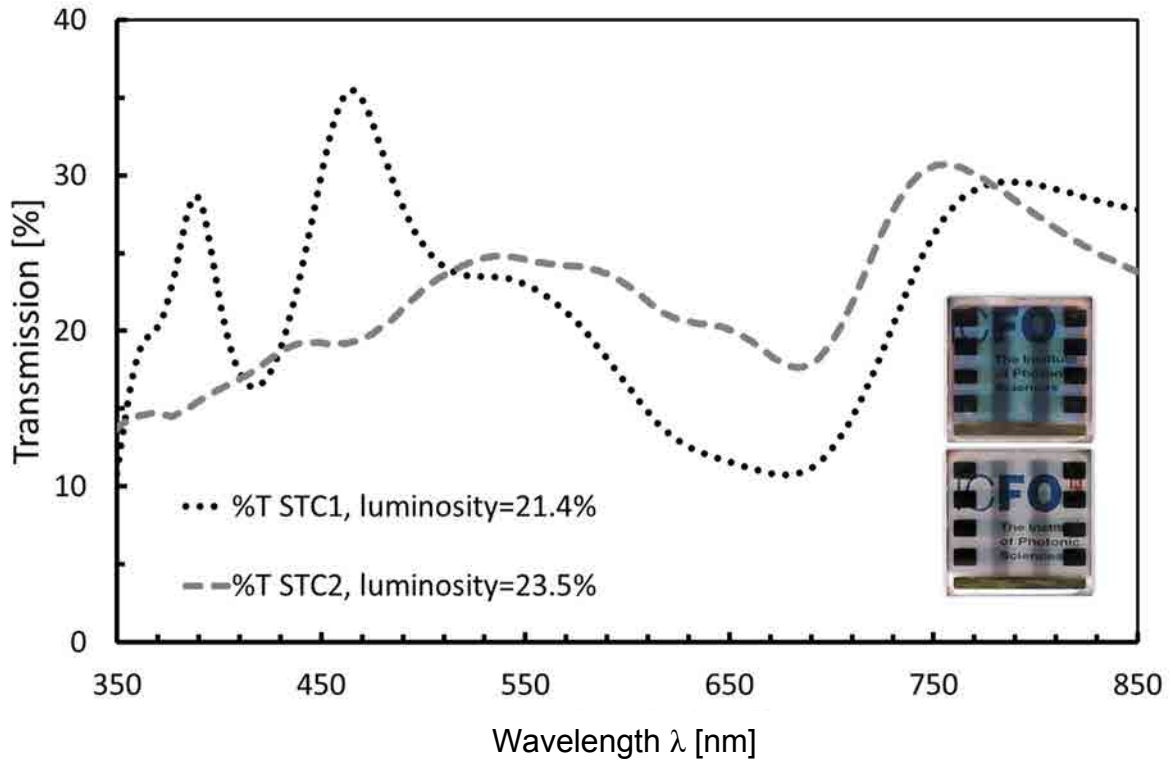


**Figure 5.4:** Light transmission for STC1 (dotted line) and for STC2 (dashed grey line). Inset: Picture of STC1 (top image) and STC2 (bottom image).

To evaluate the PV performance of the two semi-transparent devices we performed J-V measurements under  $100 \text{ mW/cm}^2$  illumination from an AM1.5G solar simulator. The corresponding J-V curves and PV parameters were compared with the corresponding measurements from the opaque cell. As may be seen in **Figure 5.5** and **Table 5.1**, the  $J_{SC}$  from the STC1 device is close to double the one from the STC2. Remarkably, as seen in Figure 5.5, the  $J_{SC}$  for STC1 is very close to the one for the opaque cell. On the contrary, the lack of an effective near IR light trapping structure for STC2 leads to a  $J_{SC}$  which is, in that latter case, only 53% the one for the opaque cell. When comparing the other PV parameters, summarized in Table 5.1, we observe a minor decrease in the  $V_{OC}$  in the amount of 2% from the opaque solar cell to both transparent ones, STC1 and STC2. Similarly, a minor decrease is observed for the FF from the opaque solar cell in the amount of 2.5% for STC2 and 5.7% for STC1. Such minor reduction observed in both parameters can be, to a large extent, attributed to the thinning down of the gold electrode. The deposition of such electrode on top of the MLD has also

a minor influence on the electrical characteristics of the solar cell provided that the observed decrease in FF is slightly larger for STC1 than for STC2. In fact, the thin gold electrode of STC2 was deposited on a polished glass, while for STC1 was deposited above the MLD comprising six sputtered dielectric thin films. In any case, since the FF and  $V_{OC}$  were affected only marginally by the MLD (cf. Table 5.1), the PCE of STC1 was 1.8 times larger than the one from STC2.

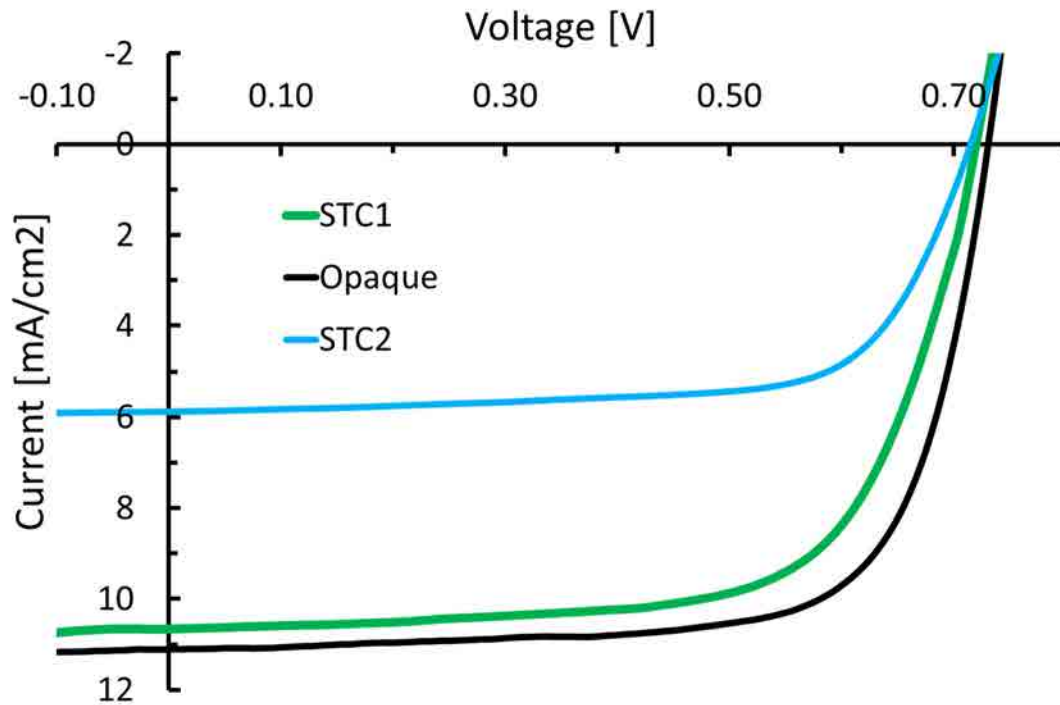


**Figure 5.5:** Measured J-V curves for the semi-transparent device (STC1) shown in Figure 5.3 (solid green) for the STC2 (solid cyan), and for the opaque solar cell (solid black).

**Table 5.1:** Solar cell J-V characteristics.

Solar cell device	$J_{sc}$ [mA cm <sup>-2</sup> ]	$J_{sc}/J_{sc}^{MAX}$ [ratio]	$V_{oc}$ [V]	FF [%]	Eff [%]	Visible Transparency [%]
STC1	10.7	0.964	0.728	67.9	5.3	21.4
Opaque	11.1	1	0.739	72.0	5.9	-
STC2	5.9	0.532	0.723	70.2	3.0	23.5

To better understand the  $J_{sc}$  behavior and its wavelength dependence we measured the EQEs for all three devices. The measured EQE for the STC1 device, shown in **Figure 5.6a**, is rather close to the one of the opaque cell, exhibiting in the 500 nm to 800 nm wavelength range a very similar behavior. In the smaller wavelength range spanning from 670 nm to 720 nm, the EQE for STC1 is even larger than the EQE for the opaque cell, indicating a more effective photon trapping by the MLD combined with a thin Au layer than the thicker Au. Such MLD enhanced EQE for STC1 is in accordance with the reduced transmission seen in Figure 5.4 for that same wavelength range. For about 100 nm, between 620 and 720 nm, such EQE exhibits a maximum value close to 65% while the EQE for STC2 is down to 25% or less. In fact, the lack of an effective photon trapping at any wavelength for STC2 leads to an EQE that remains down to about 25% in a broad wavelength range spanning from 350 nm to 700 nm.

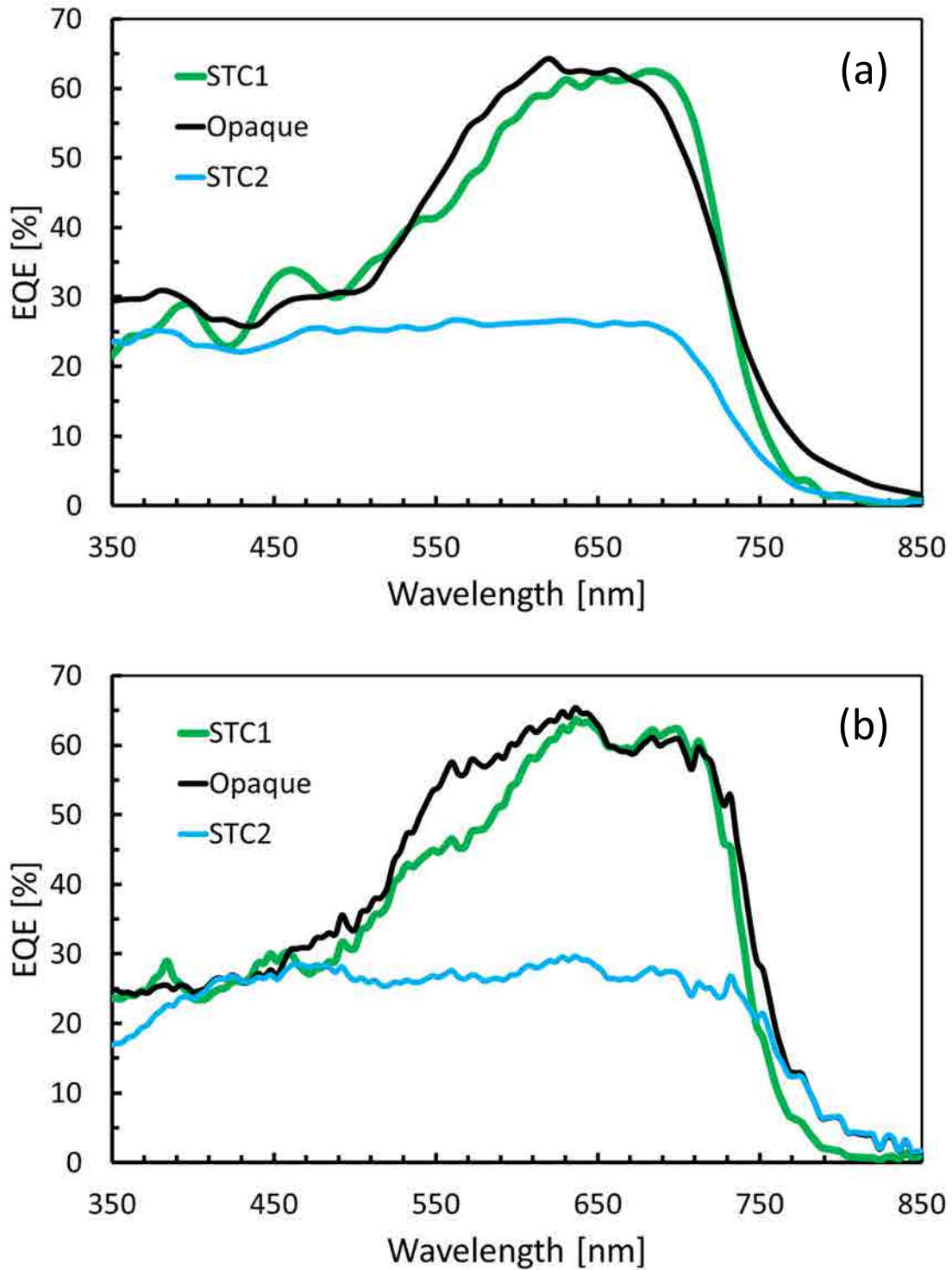


**Figure 5.6:** Experimentally measured (a) and Simulated (b) external quantum efficiencies for the semi-transparent device showed in the Figure 5.3 incorporating the MLD (in green) a semi-transparent solar cell without light trapping (in cyan) and the opaque solar cell (in black).

Such main features observed in the EQEs of the fabricated devices could be well predicted using a model [5.5, 5.28] based on the transfer matrix formalism applied to determine the EQE of thin film photovoltaic devices. We used an inverse integration procedure [5.28] to determine numerically the relative thicknesses of the six layers from the MLD. In this inverse integration to determine the configuration of the semi-transparent device including a MLD, the target solution was a device that would perform with the highest PCE with the only constraint of a visible transparency or luminosity higher than 20%. The predicted EQE can be seen in Figure 5.6b. Note that the numerically determined EQEs reproduce, in all three cases, very well the behavior of the measured EQEs.

### 5.2.3 Discussion

To conclude, we have implemented an external optical cavity configuration applied to thin film semi-transparent polymer cells that, to a large extent, avoided the loss in photon harvesting capacity exhibited by the majority of semi-transparent cells. Indeed, the  $J_{SC}$  for a cell device incorporating such cavity configuration, which exhibited a 21% visible transparency, corresponded to 96.4% the  $J_{SC}$  of the corresponding opaque cell. A small reduction in the other two PV parameters when thinning down the Au electrode led to a final PCE for the semi-transparent cell assisted with near IR light trapping of 90% the one for the opaque cell. The 21% visible transparency we demonstrated [5.33] here may find applications in PV building integration where 20% average visible transparencies are acceptable. In the event that such MLD configuration would be applied to polymers with a red shifted absorption relative to the PTB7, higher degrees of transparencies in the visible would be achievable. This would extend the areas for application of such PV technology to power up electronic devices where higher visible transparencies may be required.



## 5.2.4 Experimental

*Multilayer fabrication:* The fabricated devices were grown on soda-lime glass substrates. The SiO<sub>2</sub> and TiO<sub>2</sub> thin films of the MLD were grown using reactive magnetron sputtering in high vacuum [5.29-5.31]. Argon was used as sputter gas and oxygen as reactive gas. The SiO<sub>2</sub> films exhibited a refractive index about 1.49 at 550 nm, while the TiO<sub>2</sub> thin films exhibited a refractive index about 2.45 at 550 nm. The MLD was deposited close to normal incident to prevent any optical problem related to refractive index decrease due to an increment in the porosity of the film. As indicated below, on top of the MLD we deposited, by thermal evaporation, a thin layer of Au as electrode before proceeding with the PV device fabrication.

*Device fabrication:* A ZnO film was deposited by spin-coating on top of the gold electrode and thermally annealed on a hotplate in air (200 °C during 30 min) resulting in a 30 nm thick layer. The PTB7:PC<sub>71</sub>BM (1:1.5 wt in CB) layer was deposited by spin-coating and treated by solvent annealing during 5 min and by vacuum annealing during 30 min to obtain a 90 nm layer. Finally, a 10 nm MoO<sub>3</sub> was thermally evaporated and to finish the devices a Ag thin electrode was deposited.

*ARC and metal electrodes fabrication:* Both the transparent and the opaque gold electrodes were thermally evaporated in a high vacuum system (Mini SPECTROS™, Kurt J. Lesker Company). The speed of deposition for gold was 3 Å s<sup>-1</sup> to obtain a final thickness of 13 nm for the semi-transparent cells and 120 nm for the opaque one. Thinning down the electrode requires a lot of technical tuning and 13 nm is a good thickness that keeps an high transparency, a good electrical conductivity and an high field confinement. Thickness below 10 nm starts to have unwanted island configurations when we are searching for a functioning device with a good transparency. To complete the cell we thermally evaporated a transparent thin Ag electrode on top of the MoO<sub>3</sub> previously deposited. The deposition rate for Ag was 5.5 Å s<sup>-1</sup> while the sample was placed on a cooled holder in order to decrease Ag surface diffusion and thereby prevent 3D island growth by altering the standard nucleation process [5.32]. The Ag electrode

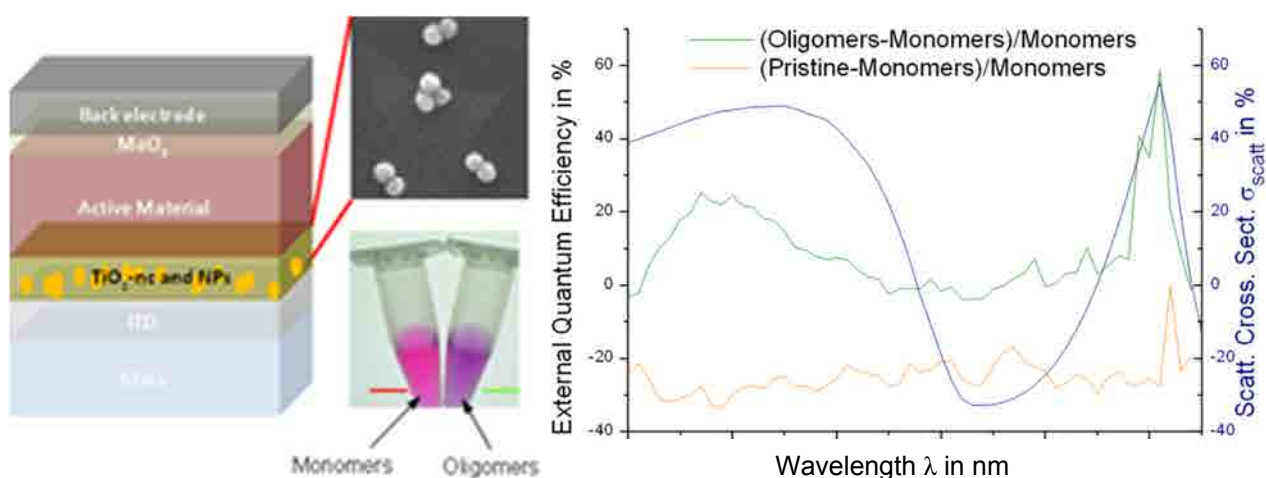
was deposited using masks made with laser beam cutting technology which yielded well-defined cell areas. Finally, on all cells, we deposited a two layer ARC comprising a layer of MoO<sub>3</sub> (n=2.17 at 550 nm) and a layer of LiF (n=1.24 at 550nm). The deposition rate for such materials were 1 Å s<sup>-1</sup>. Pellets/stones were used as material for evaporation. The residual vacuum pressure was below 10<sup>-6</sup> torr in order to prevent any contamination. The ARC was deposited close to normal incident. The thickness for all evaporated layers was monitored using a crystal oscillator during deposition and later verified from the transmission curves adjusted using the calculated electromagnetic field transmission.

*Measurement systems:* Electrical characterization (J-V measurements) was done employing an ABET technologies Sun 3000 solar simulator under AM1.5G illumination conditions and a Keithley 2420 source meter. The external quantum efficiency was measured with a solar cell spectral response measurement system from PC measurements, inc. model QEX10. The integration of the EQE spectra under the AM1.5G solar spectrum yielded J<sub>SC</sub> values that were consistent with the ones obtained from the J-V measurements (reported in Table 5.1).

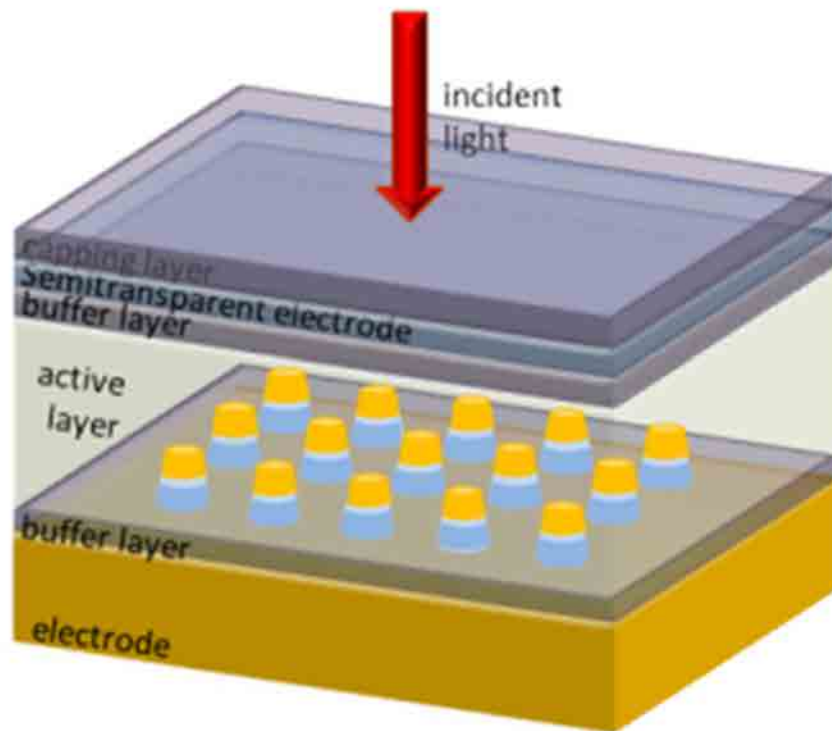
# Conclusions and Remarks

The solar energy harnessing is limited in thin film photovoltaics due to the small volume of interaction between the electromagnetic wave and the active material. Taking the extreme case of the organic solar cell, where the active layer thickness has to be smaller than 200 nm, we have shown different optical enhancement schemes.

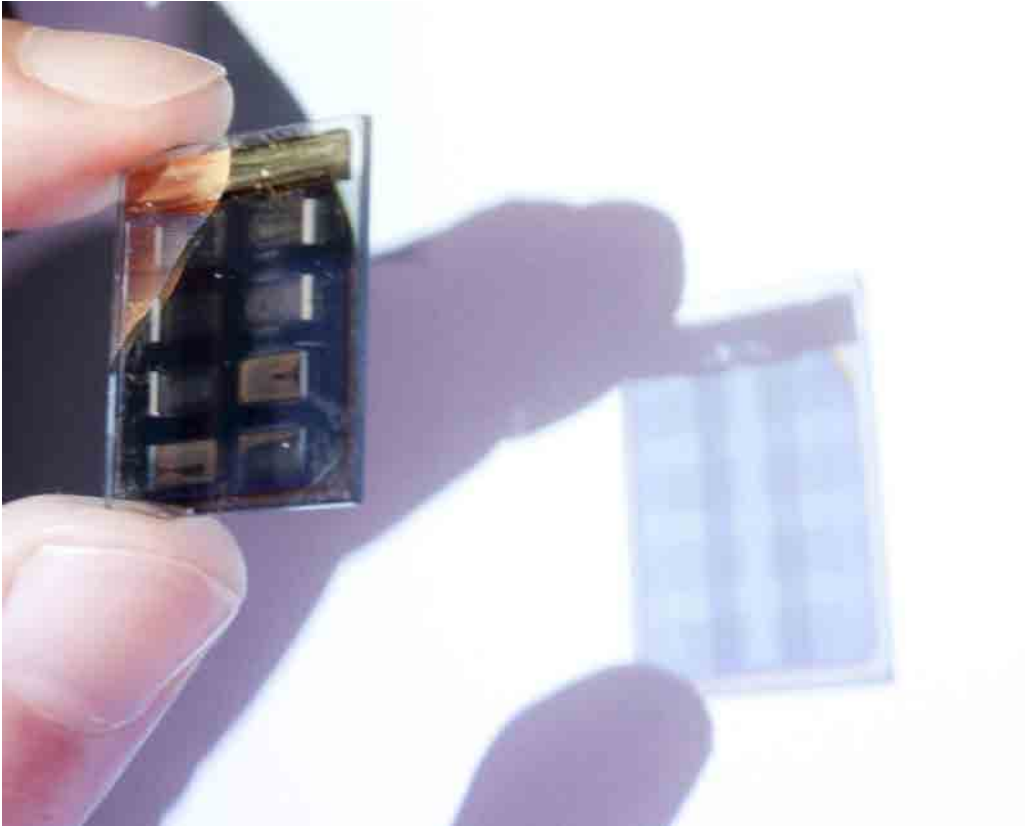
In this work, we used self-assembled randomly distributed nanogap antennas in order to maximize the light path in the device thanks to the scattering properties of such antennas. The electric field from the far field is collected by the antennas that scatter the light in a lateral and forward direction. A contribution to these phenomena are given by the presence of high refractive index  $\text{TiO}_2$  nano-crystals around the antennas, they optically help to direct the light in the wanted direction and are electrically able to transfer the electrons from the active material to the electrode. Thanks to the external quantum efficiency measurements we can compare the devices wavelength response with the nanogap antenna scattering cross section embedded in the  $\text{TiO}_2$  media. This method shows for the first time how the optical characteristics of an antenna can be retrieved when coupled in an organic solar cell device.



Additionally we used a periodic structure to exploit the near field light localization and the surface plasmon polariton effect. This has a positive effect in the photon electron conversion measurement.



In the case of semi-transparent organic photovoltaic, where the absence of a reflecting back electrode strongly reduces the amount of light absorbed in the active material, we implemented a multilayer dielectric scheme in order to enhance the light absorption without sacrificing the visible transparency. Here, we designed, fabricated and tested a transparent device that almost exhibits the same performances as an opaque one while keeping a visible transparency above 20%. This result fits correctly with our simulations, giving us a powerful tool for designing the structures that are best suited for a specific application.



Using optical enhancement techniques allows us to reduce to a minimum the consumption of material we use to fabricate photovoltaic structures. Furthermore, with optical enhancement, we can give a contribution to the achievement of the maximal theoretical efficiency opening a possible mass production scenario. Most of the emerging solar cell technologies propose a lightweight product that would allow for minimal installation costs and could be applied to consumer electronics. Finally, thanks to the versatility of the multilayer design, one could choose for a specific application, the most suitable balance between performance and visible transparency, only by changing the surrounding multilayer without changing the electrical characteristic of the device itself.



# Appendix A

---

## Materials and methods

This chapter summarizes most of the materials and deposition methods used during the present thesis. Several different materials were evaluated for their application to organic solar devices. Such evaluation concerned plasmonic materials, organic active materials, buffer layers (semiconducting hole and electron transporting films) and electrodes (not just metals but also transparent conductive oxides).

### A.1 Deposition methods

Three basic deposition methods were employed depending on the materials characteristics: spincoating, thermal evaporation and magnetron sputtering (both RF and DC).

Spincoating is the basic process for depositing organic and nanoparticle layers: a substrate rotates while a liquid solution spreads on its surface. The speed diagram of such process is shown in figure A.1(a).

Thermal evaporation is used for developing layer of metals (such as aluminium, silver, gold, calcium) or exciton blocking layers (such as Lithium fluoride (LiF) or Molybdenum oxide ( $\text{MoO}_3$ )). In this process a metal boat is heated in high vacuum conditions following the procedure presented in figure A.1(b), leading to the evaporation of the material contained in the boat. For some organic layers such as Bathocuproine (BCP) the evaporation control was done by temperature instead of power.

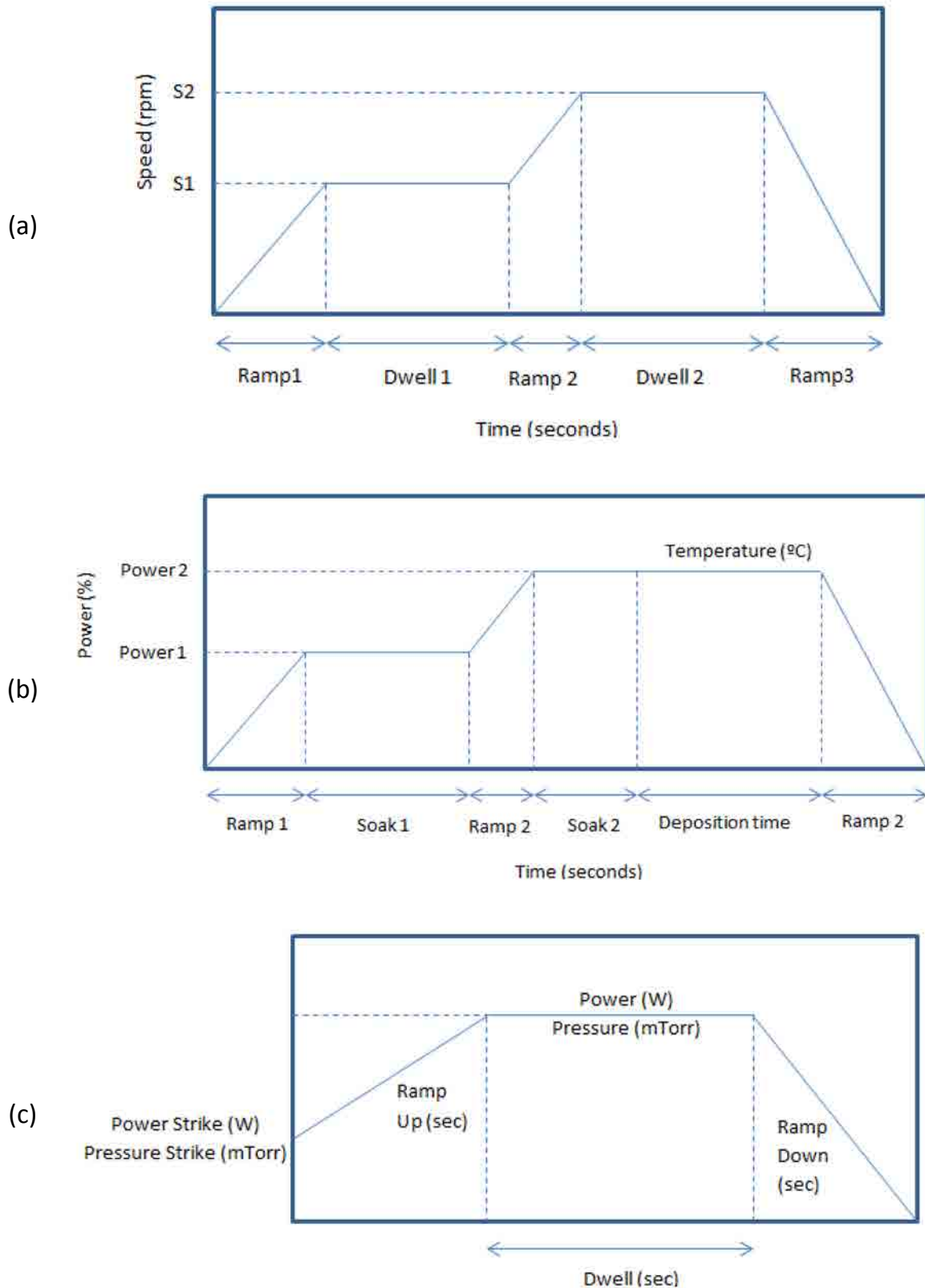


**Figure A.1:** Deposition methods diagrams employed (a) spincoating, (b) thermal evaporation and (c) sputtering [5.4].



Finally, sputtering is a method based on the bombardment of a target for depositing thin layers. Using this method several layers were deposited which include oxides ( $\text{SiO}_2$ ,  $\text{TiO}_2$ ,  $\text{NiO}$ ) or transparent conductive oxides (TCO) such as Indium tin oxide (ITO). The process involves a strike step where the plasma is started and a deposition step. Both steps are summarized in the figure A.1(c).

## A.2 Materials

Several materials were considered in the design process and then, after the simulation step, we selected the most suitable ones for the fabrication process. This section discusses the materials actually employed in the device implementation. We present the chemical structure, the relevant optical properties and some comments on the deposition methods and recipes used.

### A.2.1 Plasmonic Material

We use commercial citrate coated 40 nm AuNPs stabilized with bis(p-sulfonatophenyl) phenylphosphine (BSPP), concentrated by centrifugation and stored at 4 °C for up to one year. Then we link them with dithiothreitol (DTT), following the procedure described in [4.38].

We characterize the solutions measuring the extinction spectrum. This is the main tool we have to reveal the plasmonic behaviour of such suspensions, providing information on the material and geometry implemented.

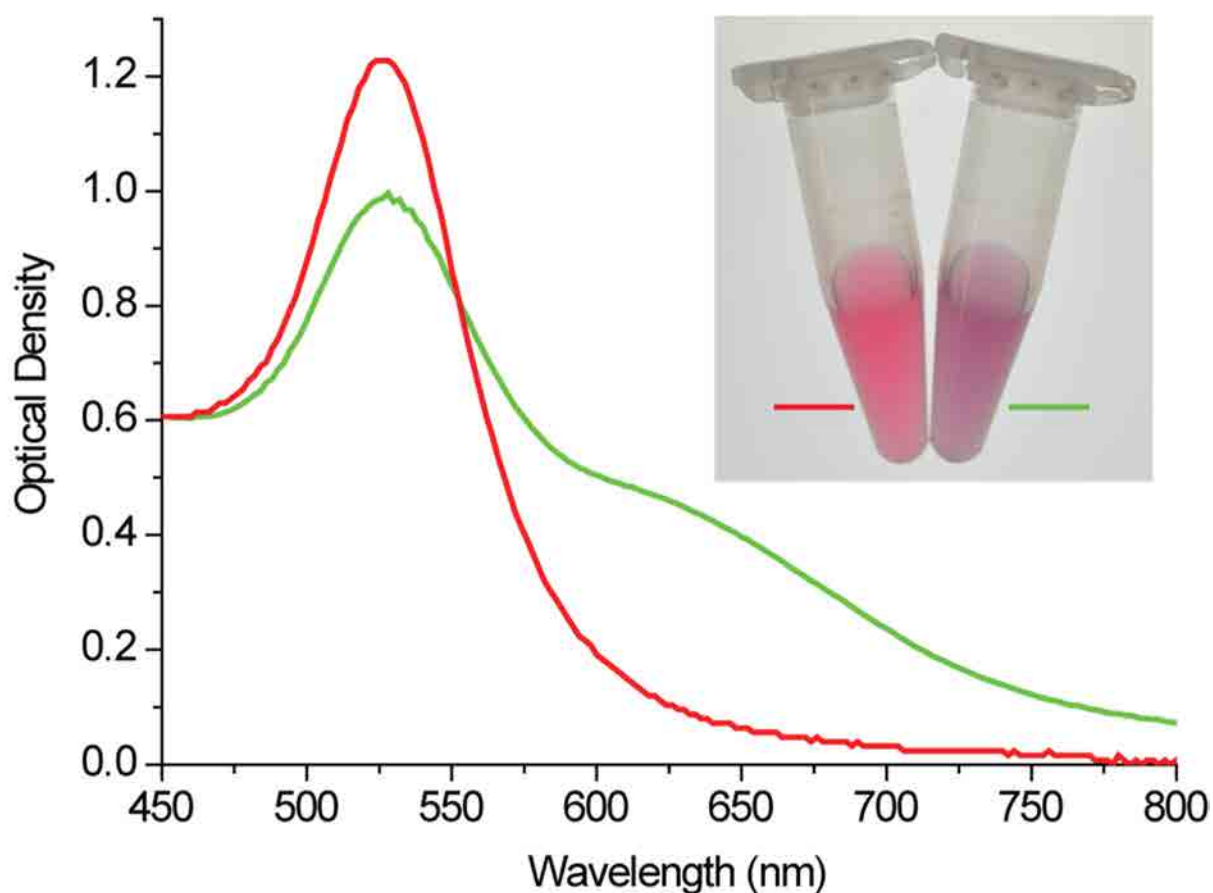


**Figure A.2:** Extinction spectra of mPEG stabilized single particles (red line) and electrophoretically optimized oligomer solution (green line) suspensions. Inset: left monomers, right oligomers.

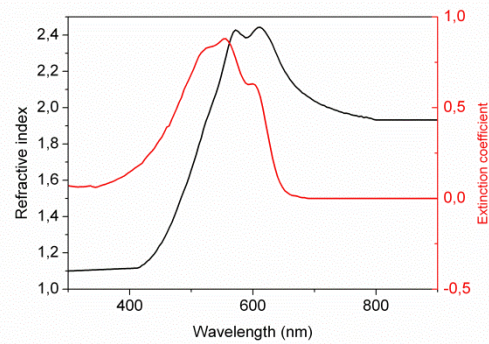
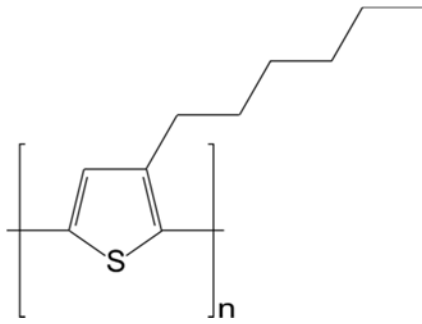
To verify that the short cross-linker allows efficient plasmon coupling necessary for high field enhancements, we measure the extinction spectrum of the oligomer suspension compared to a single-particle sample, as shown in figure A2. The single-particle sample exhibits a typical dipolar plasmon resonance at 530 nm. The oligomer sample exhibits an additional strongly red-shifted side-band that peaks at 650 nm. This band corresponds to the longitudinally coupled dipole mode for a 40 nm diameter AuNP dimer with an interparticle distance between 1 and 1.5 nm in a homogeneous dielectric environment with refractive index 1.4. The interparticle gap is consistent with the length of DTT. The 650 nm resonance induces a strong color change in the particle suspension, clearly visible in the inset: while the reference single-particle sample is red, the suspension with the larger AuNP groupings appears purple due to absorption and scattering of both green and red light. The colour difference is a strong indication that the oligomers kept their geometry before the self-assembling step on the ITO substrate. The geometry is tested afterwards with SEM imaging, see Figure 4.4 in the article.

We attach the nanoparticles on the ITO layer by UVO activation process. This process can orientate upwards the H group, that in presence of nitrogen, forms NH group. Gold can be attached on the NH group and this process can be repeated several times to allow for the optimal NPs concentration on the ITO surface.

### **A.2.2 Active materials**

The active layer in an organic photovoltaic device is based in two basic organic materials named donor and acceptor. This active layer can be structured as a planar (bilayer) or as a bulk (blend) heterojunction [5.4]. The donor is the material that mainly absorbs light and where excitons are generated. The most widely used donor material is poly(3-hexylthiophene) (P3HT). When excitons are created, they diffuse until reaching an interface with the acceptor material where they split into separated charges. The most typically used acceptor material is phenyl-C61-butyric acid methyl ester (PCBM) which is a fullerene derivative. These polymers were deposited by spincoating and the tables on the next pages present the materials employed during the development of the current thesis.

## Single donor layer: Poly(3-hexylthiophene) (P3HT)



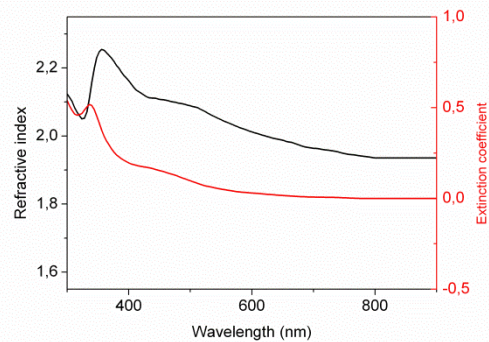
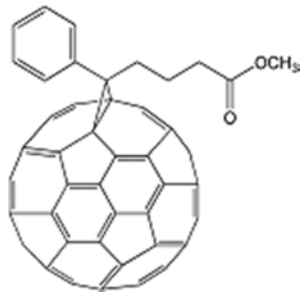
Deposition method: Spincoating

Deposition details: Chemical solution prepared a day before in Chlorobenzene or Dichlorobenzene and left stirring overnight under N<sub>2</sub> atmosphere with concentrations ranging from 5 to 30 mg/mL.

Recipe guide:

Ramp 1 (sec)	0
Speed 1 (rpm)	550
Dwell 1 (sec)	60
Ramp 2 (sec)	10
Speed 2 (rpm)	1000
Dwell 2 (sec)	70
Ramp 3 (sec)	0

For this P3HT single layer the thickness depends on the concentration according to  $T(\text{nm})=6.5[\text{P3HT}]-20$  where the [P3HT] is given in mg/mL

Single acceptor layer: Phenyl-C61-butyric acid methyl ester (PC<sub>61</sub>BM)

Deposition method: Spincoating

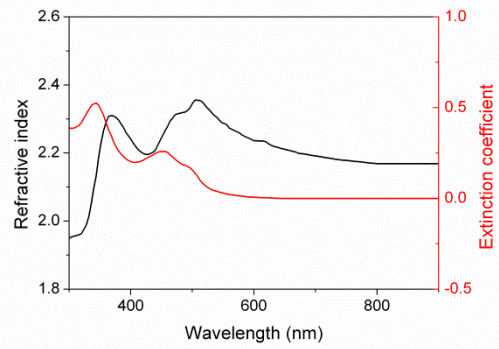
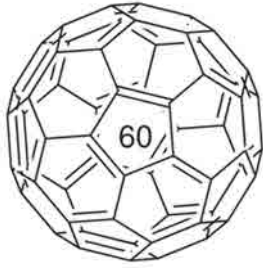
Deposition details: Chemical solution prepared a day before in Dichloromethane and left stirring overnight under N<sub>2</sub> atmosphere with concentrations 5 mg/mL.

Recipe guide:

Ramp 1 (sec)	0
Speed 1 (rpm)	4000
Dwell 1 (sec)	10
Ramp 2 (sec)	0
Speed 2 (rpm)	0
Dwell 2 (sec)	0
Ramp 3 (sec)	0

For this PC<sub>61</sub>BM single layer the thickness was around 20nm.

## Single acceptor layer: Fullerene-C60



Deposition method: Thermal evaporation

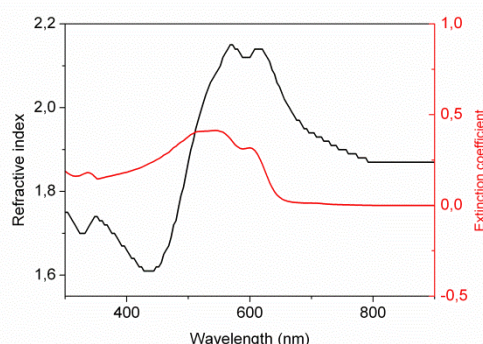
Recipe guide:

Temperature (°C)	440
Rate (Å/s)	1
Tooling factor (%)	16.2

The final thickness of the top layer was always less than 10nm.

Bulk-heterojunction:

Poly(3-hexylthiophene) (P3HT) : Phenyl-C61-butyric acid methyl ester (PC<sub>61</sub>BM)



Deposition method: Spincoating

Deposition details: Chemical solution prepared a day before in Chlorobenzene or Dichlorobenzene and left stirring overnight under N<sub>2</sub> atmosphere with proportion 1:1 (wt) and 20 mg/mL of P3HT.

Recipe guide:

Ramp 1	Speed 1	Dwell 1	Ramp 2	Speed 2	Dwell 2	Ramp 3
0	500	60	10	S2	100	0

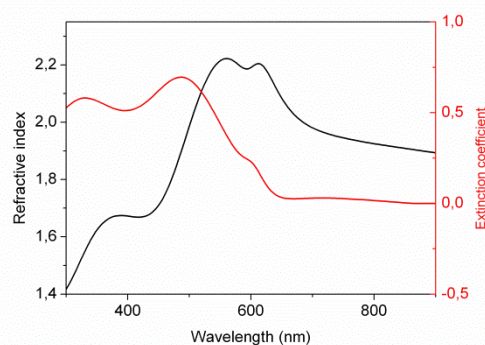
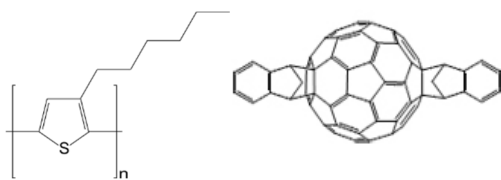
Ramp 1 (sec)	0
Speed 1 (rpm)	500
Dwell 1 (sec)	60
Ramp 2 (sec)	10
Speed 2 (rpm)	S2
Dwell 2 (sec)	100
Ramp 3 (sec)	0

Where the resulting thickness of the layer on top of PEDOT was given by  $T(nm) = 278 \cdot e^{\frac{-S2}{1416 rpm}} + 37$  and on top of TiO<sub>2</sub>-nc was given by  $T(nm) = 192 \cdot e^{\frac{-S2}{2326 rpm}}$

The devices including P3HT:PC<sub>61</sub>BM where treated with post-thermal annealing (150°C during 1 min) when the devices were finished with aluminum.

Bulk-heterojunction:

Poly(3-hexylthiophene) (P3HT) :Indene-C60 bisadduct (ICBA)



Deposition method: Spincoating

Deposition details: Chemical solution prepared a day before in Dichlorobenzene and left stirring overnight under  $N_2$  atmosphere with proportion 1:1 (wt) and 17 mg/mL of P3HT.

Recipe guide:

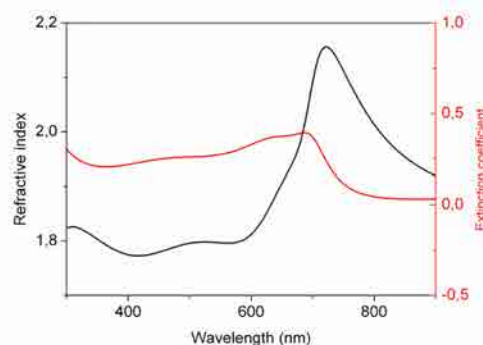
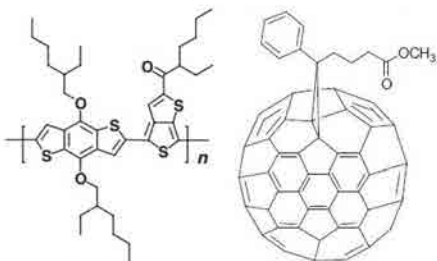
Ramp 1 (sec)	0
Speed 1 (rpm)	550
Dwell 1 (sec)	60
Ramp 2 (sec)	10
Speed 2 (rpm)	950
Dwell 2 (sec)	120
Ramp 3 (sec)	0

Where the resulting thickness of the layer on top of  $TiO_2$ -np was around 120nm and the layer included a thermal annealing of 150°C during 10 min in  $N_2$  atmosphere.



Bulk-heterojunction:

Poly[4,8-bis-substituted-benzo[1,2-b:4,5-b<sup>0</sup>]dithiophene-2,6-diyl-alt-4-substituted-thieno[3, 4-b]thiophene-2,6-diyl] (PBDTTT) : [6,6]-phenyl C71 butyric acid methyl ester (PC<sub>71</sub>BM)



Deposition method: Spincoating

Deposition details: Chemical solution prepared a day before in Dichlorobenzene (97%) + 1,8-Diiodo-octane (3%) and left stirring overnight under N<sub>2</sub> atmosphere with proportion 1:1.5 (wt) and 10 mg/mL of PBDTTT.

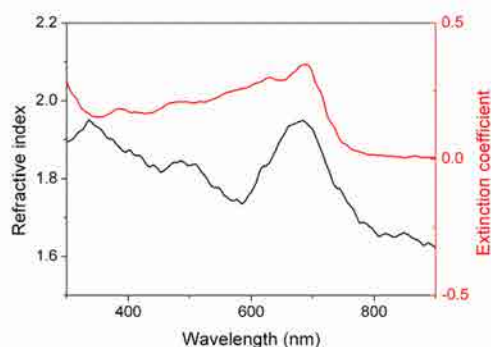
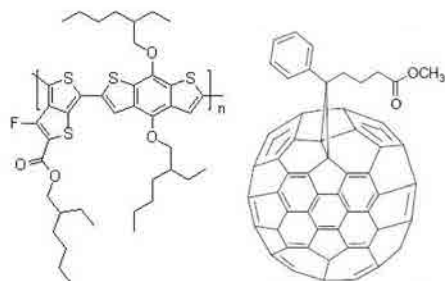
Recipe guide:

Ramp 1 (sec)	1
Speed 1 (rpm)	800
Dwell 1 (sec)	120
Ramp 2 (sec)	0
Speed 2 (rpm)	0
Dwell 2 (sec)	0
Ramp 3 (sec)	0

After the spincoating, this layer was left 5 min slow drying, 5 min under soft vacuum and 20 min under high vacuum. Its resulting thickness on top of PEDOT or ZnO was around 100nm.

Bulk-heterojunction:

Poly[[4,8-bis[(2-ethylhexyl)oxy]benzo[1,2-b:4,5-b']dithiophene-2,6-diyl][3-fluoro-2-[(2-ethylhexyl)carbonyl]thieno[3,4-b]thiophenediyl]] (PTB7) : [6,6]-phenyl C71 butyric acid methyl ester (PC<sub>71</sub>BM)



Deposition method: Spincoating

Deposition details: Chemical solution prepared a day before in chlorobenzene (97%) + 1,8-Diiodo-octane (3%) and left stirring overnight at 50°C under N<sub>2</sub> atmosphere with proportion 1:1.5 (%wt) and 10 mg/mL of PTB7.

Recipe guide:

Ramp 1 (sec)	1
Speed 1 (rpm)	1800
Dwell 1 (sec)	60
Ramp 2 (sec)	0
Speed 2 (rpm)	0
Dwell 2 (sec)	0
Ramp 3 (sec)	0

The resulting thickness of the layer on top of PEDOT or ZnO was around 90nm.

### A.2.3 Buffer layers

The electron transporting layers (ETLs) and hole transporting layers (HTLs) are placed at the interfaces of the active material and the electrodes in order to block excitons and either holes or electrons, respectively. These materials commonly [5.4] present a very high energy bandgap and the ones employed in this thesis were:

#### *Electron-transporting layers*

Titanium dioxide (TiO <sub>2</sub> ) (Anatase)	
TiO <sub>x</sub>	
Deposition method: Spincoating (nanoparticles)	
Nanoparticles synthesis:	
<p>Nanocrystalline TiO<sub>2</sub> particles were synthesized using a procedure previously reported and based on a sol-gel technique followed by growth under hydrothermal conditions [4.43]. This recipe was slightly modified in order to obtain a really fine particle size suspension (6 nm in average), which allowed forming very uniform TiO<sub>2</sub> films, and which have already been used to build highly reflectance structures in dye solar cells [4.44]. Concretely, titanium isopropoxide (20 ml, Aldrich 97%) was hydrolyzed after the addition to Milli-Q water (36 ml) and the stirring for 1 hour. Once this stage was completed, the product was filtered using 1.2 μm RTTP Millipore membranes, washed several times with distilled water and placed in a teflon reactor with 3.9 ml of 0.6 M tetramethylammonium hydroxide (~2.8M, Fluka). After homogeneizing the suspension with a stir bar, the reactor was placed in an oven preheated at 120° C, where it was kept for 3 hours. Peptization process took place during the heating in the presence of tetramethylammonium hydroxide. After this, a</p>	

bluish colloidal suspension of titanium oxide crystallites with anatase structure was obtained. Later centrifugation at 14.000 rpm for 10 minutes allowed eliminating some large aggregates from the dispersion.

Deposition details: Aqueous solutions of nanoparticles (~25% wt) were further diluted until reaching concentrations ranging from 2 to 5% (wt) and in a mixture 80:20 of methanol:water (volume). The solution was spincoated in air. The fine particle size allowed very flat surfaces and in contrast to sputtered TiO<sub>2</sub>, it did not require high temperature processing. This feature allows an optimal deposition on top of ITO and prevents indium diffusion and the consequent ITO degradation.

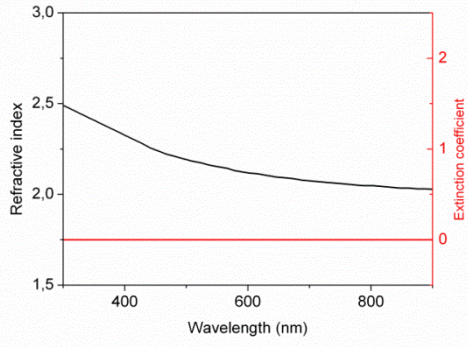
Recipe guide (3.5% wt):

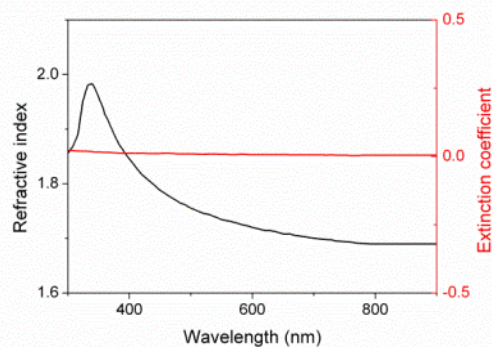
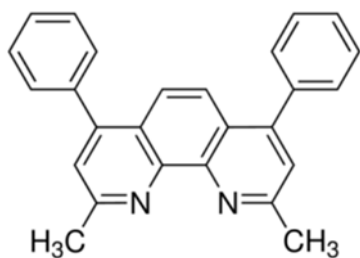
Ramp 1	Speed 1	Dwell 1	Ramp 2	Speed 2	Dwell 2	Ramp 3
S1/10.000	S1	60	0	0	0	0

Ramp 1 (sec)	S1/100 0
Speed 1 (rpm)	S1
Dwell 1 (sec)	60
Ramp 2 (sec)	0
Speed 2 (rpm)	0
Dwell 2 (sec)	0
Ramp 3 (sec)	0

The layer was treated with thermal annealing in a hotplate in air (125°C during 10 min) and the resulting thickness of the layer on top of ITO was given by  $T(nm) =$

$$97 \cdot e^{\frac{-S1}{16949 \text{ rpm}}}$$

Zinc oxide (ZnO)																													
ZnO <sub>x</sub>																													
<p>Deposition method: Spincoating (sol-gel)</p> <p>Solution preparation: The sol-gel precursor was prepared following reference [2.18]. The solution was left stirring and applied by spincoating in ambient air</p> <p>Recipe guide:</p> <table border="1" data-bbox="167 969 1206 1099"> <thead> <tr> <th>Ramp 1</th> <th>Speed 1</th> <th>Dwell 1</th> <th>Ramp 2</th> <th>Speed 2</th> <th>Dwell 2</th> <th>Ramp 3</th> </tr> </thead> <tbody> <tr> <td>0</td> <td>6000</td> <td>60</td> <td>0</td> <td>0</td> <td>0</td> <td>0</td> </tr> </tbody> </table> <table border="1" data-bbox="167 1164 512 1617"> <tbody> <tr> <td>Ramp 1 (sec)</td> <td>0</td> </tr> <tr> <td>Speed 1 (rpm)</td> <td>6000</td> </tr> <tr> <td>Dwell 1 (sec)</td> <td>60</td> </tr> <tr> <td>Ramp 2 (sec)</td> <td>0</td> </tr> <tr> <td>Speed 2 (rpm)</td> <td>0</td> </tr> <tr> <td>Dwell 2 (sec)</td> <td>0</td> </tr> <tr> <td>Ramp 3 (sec)</td> <td>0</td> </tr> </tbody> </table> <p>The layer was further thermal annealed at 200°C during 20 min in air and the resulting thickness of the layer on top of ITO was around 30nm.</p>		Ramp 1	Speed 1	Dwell 1	Ramp 2	Speed 2	Dwell 2	Ramp 3	0	6000	60	0	0	0	0	Ramp 1 (sec)	0	Speed 1 (rpm)	6000	Dwell 1 (sec)	60	Ramp 2 (sec)	0	Speed 2 (rpm)	0	Dwell 2 (sec)	0	Ramp 3 (sec)	0
Ramp 1	Speed 1	Dwell 1	Ramp 2	Speed 2	Dwell 2	Ramp 3																							
0	6000	60	0	0	0	0																							
Ramp 1 (sec)	0																												
Speed 1 (rpm)	6000																												
Dwell 1 (sec)	60																												
Ramp 2 (sec)	0																												
Speed 2 (rpm)	0																												
Dwell 2 (sec)	0																												
Ramp 3 (sec)	0																												

**Bathocuproine (BCP)**

Deposition method: Thermal evaporation

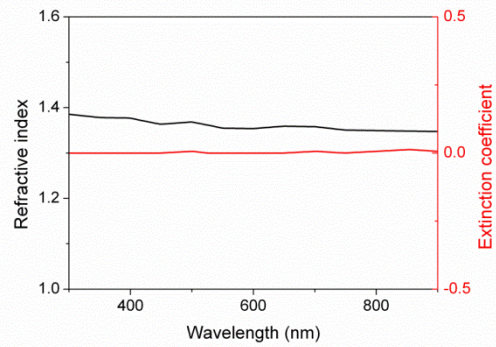
Recipe guide:

Temperature (°C)	135
Rate (Å/s)	0.5
Tooling factor (%)	12.8

The resulting thickness of the layer on top of was always less than 10nm.

## Lithium fluoride (LiF)

LiF



Deposition method: Thermal evaporation

Deposition details: Small pieces (crystals) were evaporated in alumina crucibles

Recipe guide:

Ramp 1 (sec)	140
Power 1 (%)	12
Soak time 1 (sec)	30
Ramp 2 (sec)	1
Power 2 (%)	8
Soak time 2 (sec)	100
Deposition Rate ( $\text{\AA}/\text{s}$ )	1
Ramp 3 (sec)	30
Tooling factor (%)	44.5

The resulting thickness of the layer on top of was never more than 2 nm.

**Lithium cobalt oxide (LiCoO<sub>2</sub>)**

Deposition method: Reactive sputtering

Deposition details: This layer was always developed on top of organic layers at room temperature.

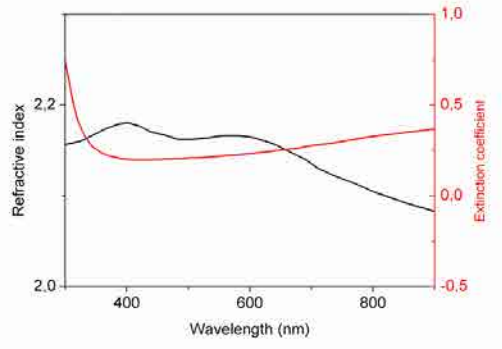
Recipe guide:

Power strike (W)	40
Pressure strike (mTorr)	40
Ramp up (sec)	18
Deposition power (W)	70 RF
Deposition Pressure (mTorr)	2.5 [20 Ar : 10 O <sub>2</sub> ]
Deposition temperature (°C)	RT
Height (cm)	30
Deposition Rate (Å/s)	0.075
Ramp down (sec)	42

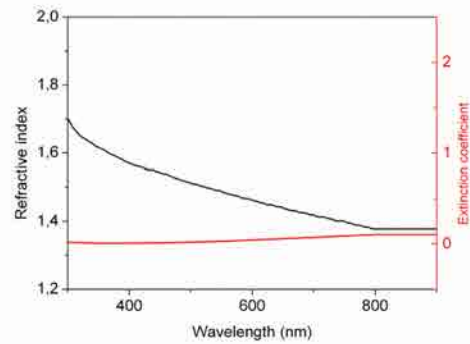
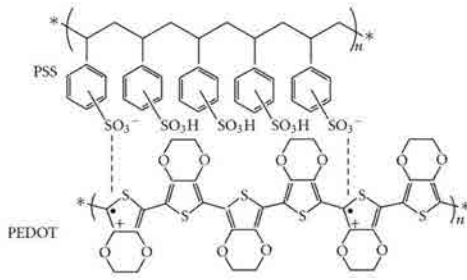
The resulting thickness of the layer on top of the organic layer was always kept below 1nm.



**Hole-transporting layers**

Molybdenum oxide ( $\text{MoO}_3$ )																			
$\text{MoO}_x$																			
<p>Deposition method: Thermal evaporation</p> <p>Deposition details: Molybdenum oxide pieces were placed in alumina crucibles and thermally evaporated</p> <p>Recipe guide:</p> <table border="1" data-bbox="167 1086 726 1668"> <tr> <td>Ramp 1 (sec)</td> <td>60</td> </tr> <tr> <td>Power 1 (%)</td> <td>8.3</td> </tr> <tr> <td>Soak time 1 (sec)</td> <td>70</td> </tr> <tr> <td>Ramp 2 (sec)</td> <td>5</td> </tr> <tr> <td>Power 2 (%)</td> <td>6.6</td> </tr> <tr> <td>Soak time 2 (sec)</td> <td>200</td> </tr> <tr> <td>Deposition Rate (<math>\text{\AA}/\text{s}</math>)</td> <td>1</td> </tr> <tr> <td>Ramp 3 (sec)</td> <td>30</td> </tr> <tr> <td>Tooling factor (%)</td> <td>53</td> </tr> </table> <p>The thickness of the deposited layer always ranged between 3 and 40 nm.</p>		Ramp 1 (sec)	60	Power 1 (%)	8.3	Soak time 1 (sec)	70	Ramp 2 (sec)	5	Power 2 (%)	6.6	Soak time 2 (sec)	200	Deposition Rate ( $\text{\AA}/\text{s}$ )	1	Ramp 3 (sec)	30	Tooling factor (%)	53
Ramp 1 (sec)	60																		
Power 1 (%)	8.3																		
Soak time 1 (sec)	70																		
Ramp 2 (sec)	5																		
Power 2 (%)	6.6																		
Soak time 2 (sec)	200																		
Deposition Rate ( $\text{\AA}/\text{s}$ )	1																		
Ramp 3 (sec)	30																		
Tooling factor (%)	53																		

## Poly(3,4-ethylenedioxythiophene) poly(styrenesulfonate) (PEDOT:PSS)



Deposition method: Spincoating

Deposition details: Solutions from Clevios (Al 4083) were filtered before deposition

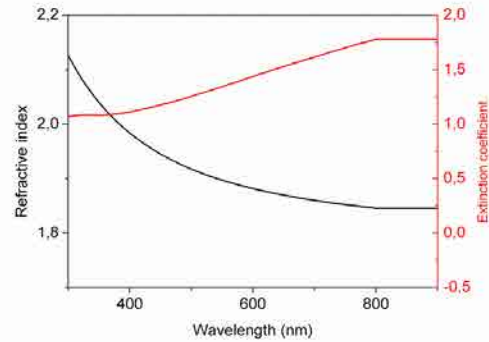
Recipe guide:

Ramp 1 (sec)	5
Speed 1 (rpm)	S1
Dwell 1 (sec)	30
Ramp 2 (sec)	0
Speed 2 (rpm)	0
Dwell 2 (sec)	0
Ramp 3 (sec)	0

The typical thermal annealing was 125°C during 10 min in a hotplate in air and the

resulting thickness of the layer on top of ITO was given by  $T(nm) = 62 \cdot e^{\frac{-S1}{13210 rpm}}$

## Nickel oxide (NiO)

NiO<sub>x</sub>

Deposition method: Sputtering

Deposition details: This hole transporting layer was always deposited on top of ITO

Recipe guide:

Power strike (W)	40
Pressure strike (mTorr)	40
Ramp up (sec)	36
Deposition power (W)	100 RF
Deposition Pressure (mTorr)	1.5 [20Ar-10O <sub>2</sub> ]
Deposition temperature (°C)	RT
Height (cm)	30
Deposition Rate (Å/s)	0.09
Ramp down (sec)	60

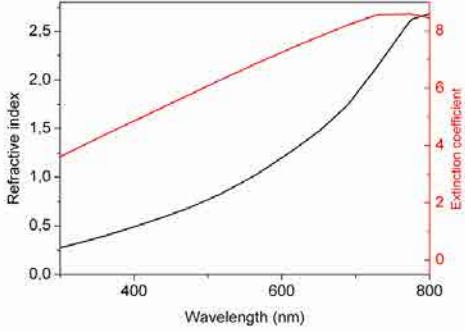
After deposition, a plasma activation step (O<sub>2</sub> plasma) was required for enhancing the final V<sub>oc</sub> of the devices. The minimum thickness of this layer on top of ITO was found to be 4.5nm.

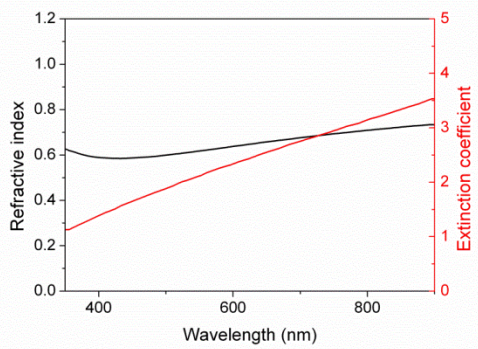
### A.2.4 Electrodes

Two different kinds of materials were used as electrodes, transparent conductive oxides (TCOs) concretely Indium tin oxide (ITO) and Aluminum doped zinc oxide (AZO) and common metal electrodes:

Indium tin oxide (ITO)	
ITO	
Deposition method: Reactive sputtering	
Recipe guide:	
Power strike (W)	40
Pressure strike (mTorr)	40
Ramp up (sec)	90
Deposition power (W)	70 DC
Deposition Pressure (mTorr)	2 [20 Ar : 10 O <sub>2</sub> ]
Deposition temperature (°C)	100
Height (cm)	30
Deposition Rate (Å/s)	0.8
Ramp down (sec)	210
<p>After the deposition, the ITO layer was thermal annealed at 300°C in a hotplate in air during 5 min. The minimum thickness in order to have a good conductivity was around 110 nm.</p>	

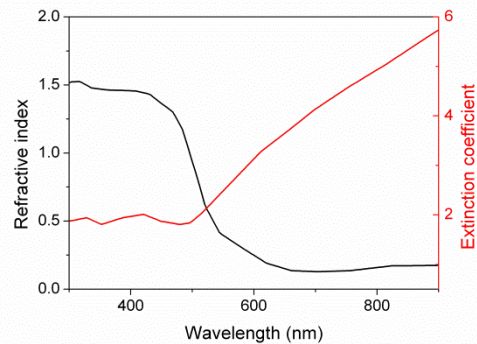
Silver (Ag)																			
Ag																			
<p>Deposition method: Thermal evaporation</p> <p>Deposition details: Silver was found to be a very good electrode where no post-thermal annealing for the device was required. As a thin electrode was also very good and involved the use of low temperature substrate (<math>\sim -5^{\circ}\text{C}</math>) to avoid diffusion [4.54].</p> <p>Recipe guide:</p> <table border="1"> <tbody> <tr> <td>Ramp 1 (sec)</td> <td>60</td> </tr> <tr> <td>Power 1 (%)</td> <td>12.8</td> </tr> <tr> <td>Soak time 1 (sec)</td> <td>190</td> </tr> <tr> <td>Ramp 2 (sec)</td> <td>33</td> </tr> <tr> <td>Power 2 (%)</td> <td>14.2</td> </tr> <tr> <td>Soak time 2 (sec)</td> <td>75</td> </tr> <tr> <td>Deposition Rate (<math>\text{\AA}/\text{s}</math>)</td> <td>1</td> </tr> <tr> <td>Ramp 3 (sec)</td> <td>30</td> </tr> <tr> <td>Tooling factor (%)</td> <td>28</td> </tr> </tbody> </table>		Ramp 1 (sec)	60	Power 1 (%)	12.8	Soak time 1 (sec)	190	Ramp 2 (sec)	33	Power 2 (%)	14.2	Soak time 2 (sec)	75	Deposition Rate ( $\text{\AA}/\text{s}$ )	1	Ramp 3 (sec)	30	Tooling factor (%)	28
Ramp 1 (sec)	60																		
Power 1 (%)	12.8																		
Soak time 1 (sec)	190																		
Ramp 2 (sec)	33																		
Power 2 (%)	14.2																		
Soak time 2 (sec)	75																		
Deposition Rate ( $\text{\AA}/\text{s}$ )	1																		
Ramp 3 (sec)	30																		
Tooling factor (%)	28																		

Aluminum (Al)																			
Al																			
<p>Deposition method: Thermal evaporation</p> <p>Deposition details: Deposition rate was always kept close to <math>1\text{\AA}/\text{s}</math> to prevent boat damage.</p> <p>Recipe guide:</p> <table border="1" data-bbox="167 969 722 1552"> <tbody> <tr> <td>Ramp 1 (sec)</td> <td>60</td> </tr> <tr> <td>Power 1 (%)</td> <td>10</td> </tr> <tr> <td>Soak time 1 (sec)</td> <td>60</td> </tr> <tr> <td>Ramp 2 (sec)</td> <td>33</td> </tr> <tr> <td>Power 2 (%)</td> <td>13</td> </tr> <tr> <td>Soak time 2 (sec)</td> <td>60</td> </tr> <tr> <td>Deposition Rate (<math>\text{\AA}/\text{s}</math>)</td> <td>1</td> </tr> <tr> <td>Ramp 3 (sec)</td> <td>30</td> </tr> <tr> <td>Tooling factor (%)</td> <td>69</td> </tr> </tbody> </table> <p>The resulting thickness of the layer was typically over 100 nm.</p>		Ramp 1 (sec)	60	Power 1 (%)	10	Soak time 1 (sec)	60	Ramp 2 (sec)	33	Power 2 (%)	13	Soak time 2 (sec)	60	Deposition Rate ( $\text{\AA}/\text{s}$ )	1	Ramp 3 (sec)	30	Tooling factor (%)	69
Ramp 1 (sec)	60																		
Power 1 (%)	10																		
Soak time 1 (sec)	60																		
Ramp 2 (sec)	33																		
Power 2 (%)	13																		
Soak time 2 (sec)	60																		
Deposition Rate ( $\text{\AA}/\text{s}$ )	1																		
Ramp 3 (sec)	30																		
Tooling factor (%)	69																		

Calcium (Ca)																			
Ca																			
<p>Deposition method: Thermal evaporation</p> <p>Deposition details: This layer was used as an electrode and was always employed in the electron transporting layer interface in combination with aluminum or silver.</p>																			
<p>Recipe guide:</p> <table border="1" data-bbox="167 974 726 1556"> <tbody> <tr> <td>Ramp 1 (sec)</td> <td>240</td> </tr> <tr> <td>Power 1 (%)</td> <td>6.5</td> </tr> <tr> <td>Soak time 1 (sec)</td> <td>160</td> </tr> <tr> <td>Ramp 2 (sec)</td> <td>60</td> </tr> <tr> <td>Power 2 (%)</td> <td>7</td> </tr> <tr> <td>Soak time 2 (sec)</td> <td>60</td> </tr> <tr> <td>Deposition Rate (Å/s)</td> <td>1</td> </tr> <tr> <td>Ramp 3 (sec)</td> <td>60</td> </tr> <tr> <td>Tooling factor (%)</td> <td>60</td> </tr> </tbody> </table>		Ramp 1 (sec)	240	Power 1 (%)	6.5	Soak time 1 (sec)	160	Ramp 2 (sec)	60	Power 2 (%)	7	Soak time 2 (sec)	60	Deposition Rate (Å/s)	1	Ramp 3 (sec)	60	Tooling factor (%)	60
Ramp 1 (sec)	240																		
Power 1 (%)	6.5																		
Soak time 1 (sec)	160																		
Ramp 2 (sec)	60																		
Power 2 (%)	7																		
Soak time 2 (sec)	60																		
Deposition Rate (Å/s)	1																		
Ramp 3 (sec)	60																		
Tooling factor (%)	60																		
<p>The resulting thickness of the layer on top of the organic was around 20 nm.</p>																			

## Gold (Au)

Au



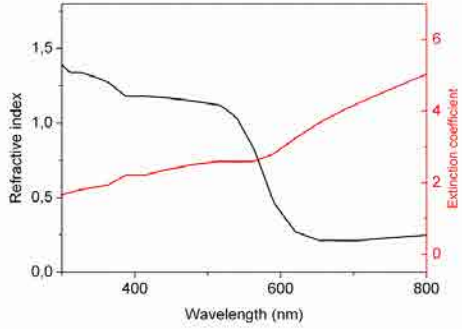
Deposition method: thermal evaporation

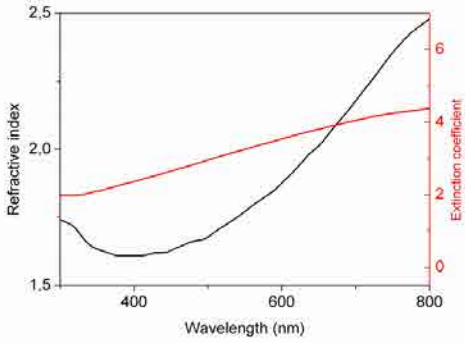
Deposition details: Gold was found to be a very good electrode where no post-thermal annealing for the device was required. As a thin electrode, it need to have a thickness above 9 nm to avoid the presence of nano islands. To be attached on a glass substrate it needs an extra layer of Titanium, typically of about 2nm, otherwise the fabrication process on it need to be extremely careful. Thanks to its high penetration depth can be 20% thicker than Silver, but the same transparency can be kept.

Recipe guide:

Ramp 1 (sec)	120
Power 1 (%)	10.5
Soak time 1 (sec)	80
Ramp 2 (sec)	120
Power 2 (%)	15
Soak time 2 (sec)	60
Deposition Rate (Å/s)	1
Ramp 3 (sec)	30
Tooling factor (%)	39



Copper (Cu)	
Cu	
Deposition method: thermal evaporation	
Recipe guide:	
Power strike (W)	40
Pressure strike (mTorr)	40
Ramp up (sec)	12
Deposition power (W)	20 DC
Deposition Pressure (mTorr)	12
Deposition temperature (°C)	RT
Height (cm)	30
Deposition Rate (Å/s)	0.131
Ramp down (sec)	12
The percolation limit was found to be around 7nm.	

Nickel (Ni)	
Ni	
Deposition method: thermal evaporation	
Recipe guide:	
Power strike (W)	40 DC
Pressure strike (mTorr)	40
Ramp up (sec)	12
Deposition power (W)	20 DC
Deposition Pressure (mTorr)	3
Deposition temperature (°C)	RT
Height (cm)	30
Deposition Rate (Å/s)	0.108
Ramp down (sec)	12
The percolation limit was found to be around 4 nm.	

### A.2.5 Other materials

SiO<sub>2</sub> was employed in combination with TiO<sub>2</sub> for growing 1-dimensional photonic crystals of few layers. The properties of TiO<sub>2</sub> and the following table summarizes the ones for SiO<sub>2</sub>

Silicon oxide (SiO <sub>2</sub> )	
SiO <sub>x</sub>	
Deposition method: sputtering	
Recipe guide:	
Power strike (W)	40 RF
Pressure strike (mTorr)	40
Ramp up (sec)	360
Deposition power (W)	100 RF
Deposition Pressure (mTorr)	2
Deposition temperature (°C)	RT
Height (cm)	30
Deposition Rate (Å/s)	0.14
Ramp down (sec)	360



# References

---

## References Chapter 1.

- [1.1] BP – British Petroleum, “BP Statistical Review of World Energy”, June 2013.
- [1.2] EPIA – European Photovoltaic Industry Association, “Photovoltaic energy, electricity from the sun”, 2013.
- [1.3] G. Edwards “Cost Disadvantages of Expanding the Nuclear Power Industry”, The Canadian Business Review, Vol. 9, Num. 1, 1982.
- [1.4] Commission staff, the European Parliament and the council “Package of implementation measures for the EU's objectives on climate change and renewable energy for 2020”, 2008.
- [1.5] [retinking2050.org](http://retinking2050.org), 2013.
- [1.6] J. Torriti “Demand Side Management for the European Supergrid”, Energy Policy vol. 44, pp. 199-206, 2012.
- [1.7] National Energy Technology Laboratory, “NETL Modern Grid Initiative — Powering Our 21st-Century Economy”, United States Department of Energy Office of Electricity Delivery and Energy Reliability. p. 17. Retrieved 2008-12-06.
- [1.8] Pacific Northwest National Laboratory, "Gridwise History: How did GridWise start?", 2007.

- [1.9] I. Pérez-Arriaga, S. Ruester, S. Schwenen, C. Batlle, J.-M Glachant, F. Lévêque, W. Mielczarski, “From Distribution Networks to Smart Distribution Systems: Rethinking the Regulation of European Electricity DSOs”, Think final report, European University Institute, 2013.
- [1.10] A. París, T. Pujol, J. Vela, “L’ordenança solar tèrmica de Barcelona, Valoració i balanç de l’aplicació”, Agència d’Energia de Barcelona, 2006.
- [1.11] Japan construction regulation M E T I -Agency for Natural Resources and Energy “feed in tariffs scheme in Japan”, July 2012.
- [1.12] EPIA - European Photovoltaic Industry Association, “Global Market Outlook for Photovoltaics 2013-2017”, 2013.
- [1.13] PV CYCLE - European photovoltaic recycle association, “Annual report 2012”, 2013.
- [1.14] T. Grigoleit, T. Rothacher, M. Ouw, “Industry overview the photovoltaic market in Germany”, Germany Trade & Invest, 2013.
- [1.15] Il ministro dello sviluppo economico, Il ministro dell’ambiente e della tutela del territorio e del mare, “Quinto conto energia”, Supplemento ordinario n. 143 alla gazzetta ufficiale, 2012.
- [1.16] C. Stagnaro, “How solar subsidies can distort the power market: the case of Italy”, European energy review, report, 2012.
- [1.17] Royal Decree law draft presented to the energy regulator CNE in July 2013.
- [1.18] “Directive on the restriction of the use of certain hazardous substances in electrical and electronic equipment (I and II)”, Official Journal of the European Union, (I) 2003 and (II) 2011.
- [1.19] National renewable energies laboratory, [www.nrel.gov](http://www.nrel.gov), USA, 2013.
- [1.20] Sharp co., Press releases, June 2013.

- [1.21] F. Pastorelli, et al. “Antireflection film, solar battery cell, method for manufacturing antireflection film, and method for manufacturing solar battery cell”, JP Patent 2,011,119,740, 2011.
- [1.22] A. Higo, F. Pastorelli, K. Watanabe, M. Sugiyama, and Y. Nakano, “Design and fabrication of broadband anti-reflection sub-wavelength periodic structure for solar cells”, Renewable energy 2010, Yokoama, O-Pv-5-5, 2010.
- [1.23] A. Luque, “Will we exceed 50% efficiency in photovoltaics?”, J. Appl. Phys. 110, 031301, 2011.

## References Chapter 2.

- [2.1] Eduardo Lorenzo, “Solar Electricity: Engineering of Photovoltaic Systems”, Progensa, ISBN 84-86505-55-0. p.80, 1994.
- [2.2] J.L. Gray, A. Luque, S. Hegedus, “The Physics of the Solar Cell, in Handbook of Photovoltaic Science and Engineering”, John Wiley and Sons, 2011.
- [2.3] W. Cai, X. Gong, Y. Cao, Solar Energy Materials and Solar Cells, 94, 114, 2010.
- [2.4] L. J. A. Koster, “Device physics of donor/acceptor-blend solar cells”, PhD thesis, University of Groningen, 2007.
- [2.5] Lawrence L. Kazmerski, 2001.
- [2.6] G. D. Scholes, G. Rumbles, Nat Mater 5, 683, 2006.
- [2.7] M. O. Scully, Physical Review Letters 104, 207701, 2010.
- [2.8] J. D. Servaites, S. Yeganeh, T. J. Marks, M. A. Ratner, Advanced Functional Materials 20, 97, 2010.

- [2.9] M.D. Irwin, D.B. Buchholz, A.W. Hains, R.P.H. Chang, T.J. Marks, PNAS, vol. 105 no. 8, 2783–2787, 2008.
- [2.10] K. Petritsch, Technische Universitat Graz Austria Doctoral Thesis, 1, 159, 2000.
- [2.11] J.-L. Wu, F.-C. Chen, Y.-S. Hsiao, F.-C. Chien, P. Chen, C.-H. Kuo, M.H. Huang, C.-S. Hsu, ACS Nano, 5, 959, 2011.
- [2.12] R.R. Lunt, N.C. Giebink, A. a. Belak, J.B. Benziger, S.R. Forrest, Journal of Applied Physics, 105, 053711, 2009.
- [2.13] Y. Yuan, J. Huang, G. Li, Green, Vol 1, pp. 65- 80, 2011.
- [2.14] D. W. Zhao et al., Solar Energy Materials and Solar Cells 95, 921, 2011.
- [2.15] J. Meiss, T. Menke, K. Leo, C. Uhrich, W.-M. Gnehr, S. Sonntag, M. Pfeiffer, M. Riede, Applied Physics Letters, 99, 043301Y, 2011.
- [2.16] K.-S. Chen, J.-F. Salinas, H.-L. Yip, L. Huo, J. Hou, A.K.-Y. Jen, Energy Environ. Sci, 5, 9551, 2012.
- [2.17] C.-C. Chueh, S.-C. Chien, H.-L. Yip, J.F. Salinas, C.-Z. Li, K.-S. Chen, F.-C. Chen, W.-C. Chen, A.K.-Y. Jen, Advanced Energy Materials, 2012.
- [2.18] Y. Sun, C. J. Takacs, S. R. Cowan, J. H. Seo, X. Gong, A. Roy, & A. J. Heeger, “Efficient, air-stable bulk heterojunction polymer solar cells using MoO(x) as the anode interfacial layer”, Advanced materials, 23(19), 2226–30, 2011.
- [2.19] C. H. Peters, I. T. Sachs-Quintana, J. P. Kastrop, S. Beaupré, M. Leclerc, & M. D. McGehee, “High Efficiency Polymer Solar Cells with Long Operating Lifetimes”, Advanced Energy Materials, 1(4), 491–494, 2011.
- [2.20] K. Li, H. Fan, C. Huang, X. Hong, X. Fang, H. Li, and H. Zhen, “Thin-film encapsulation of inverted indium-tin-oxide-free polymer solar cells by atomic layer deposition with improvement on stability and efficiency”. Applied Physics Letters, 101(23), 233902, 2012.



- [2.21] T.-Y. Chu, S.-W. Tsang, J. Zhou, P. G. Verly, J. Lu, S. Beaupré and Y. Tao, “High-efficiency inverted solar cells based on a low bandgap polymer with excellent air stability”, *Solar Energy Materials and Solar Cells*, 96, 155–159, 2012.
- [2.22] M. J. Tan, S. Zhong, J. Li, Z. Chen, & W. Chen, “Air-stable efficient inverted polymer solar cells using solution-processed nanocrystalline ZnO interfacial layer”, *ACS applied materials & interfaces*, 5(11), 4696–701, 2013.
- [2.23] M. Jørgensen, K. Norrman, S. Gevorgyan, T. Tromholt, B. Andreasen & F. C. Krebs, “Stability of polymer solar cells”, *Advanced materials (Deerfield Beach, Fla.)*, 24(5), 580–612, 2012.

### References Chapter 3.

- [3.1] J. Nelson, “The Physics of Solar Cells”, Imperial College Press, London, 2003.
- [3.2] C. Zamparelli, “Storia, Scienza e Leggenda degli specchi ustori di Archimede”, Pisa, 2005.
- [3.3] Giulio Parigi, Wall painting from the Uffizi Gallery, stanzino delle matematiche, Florence, 1600.
- [3.4] F. Pastorelli, et al. “Antireflection film, solar battery cell, method for manufacturing antireflection film, and method for manufacturing solar battery cell”, JP Patent 2,011,119,740, 2011.
- [3.5] A. Higo, F. Pastorelli, K. Watanabe, M. Sugiyama, and Y. Nakano, “Design and fabrication of broadband anti-reflection sub-wavelength periodic structure for solar cells”, *Renewable energy 2010*, Yokoama, O-Pv-5-5, 2010.

- [3.6] B. M. Damiani “Investigation of light induced degradation on promising photovoltaic grade silicon and development of porous silicon anti-reflection coatings for silicon solar cells”, Georgia Institute of Technology, April 2004.
- [3.7] M. Chen, H. Chang, A. S. P. Chang, S. Lin, J. -. Xi, and E. F. Schubert, "design of optical path for wide-angle gradient-index antireflection coatings", *Appl. Opt.* 46, 6533-6538, 2007.
- [3.8] S. A. Boden, D. M. Bagnall, “tunable reflection minima of nanostructured antireflective surfaces” *Appl. Phys. Lett.* 93, 133108, September 2008.
- [3.9] L. Zeng, “high efficiency thin film silicon solar cells with novel light trapping: principle, design and processing”, Massachusetts Institute of Technology, 2008.
- [3.10] J.E. Parrott, “Radiative recombination and photon recycling in photovoltaic solar cells”, *Solar Energy Materials and Solar Cells*, Volume 30, Issue 3, Pages 221-231, August 1993.
- [3.11] V. Badescu and P. T. Landsberg, “Theory of some effects of photon recycling in semiconductors”, *Semicond. Sci. Technol.* 8, 1267, 1993.
- [3.12] N. J. Ekins-Daukes, T. W. Schmidt “a molecular approach to the intermediate band solar cell: the symmetric case”, *Appl. Phys. Lett.* 93, August 2008.
- [3.13] G. Boyle, *Renewable Energy*, 2004
- [3.14] W. Cai, X. Gong, Y. Cao, *Solar Energy Materials and Solar Cells*, 94, 114, 2010.
- [3.15] M.K. Riede, *Universität Konstanz Doctoral Thesis*, 1, 228, 2006.
- [3.16] K. Petritsch, *Technische Universität Graz Austria Doctoral Thesis*, 1, 159, 2000.
- [3.17] K. J. Vahala, “Optical microcavities”, *Nature*, 424(6950), 839–46, 2003.
- [3.18] P. Biagioni, J.-S. Huang and B. Hecht, “Nanoantennas for visible and infrared radiation”, *Reports on Progress in Physics*, 75, 2, 024402, 2012.
- [3.19] A. Curto, “Optical antennas control light emission”, *ICFO doctoral thesis*, 2013.

## References Chapter 4.

- [4.1] H.-Y. Chen, J.Hou, S. Zhang, Y. Liang, G. Yang, Y. Yang, L. Yu, Y. Wu, G. Li, *Nat. Photon.*, 3, 649, 2009.
- [4.2] R. R. Lunt, V. Bulovic, *Appl. Phys. Lett.*, 98, 113305, 2011.
- [4.3] M. Kaltenbrunner, M. S. White, E. D. Głowacki, T. Sekitani, T. Someya, N. S. Sariciftci, S. Bauer, *Nat. Commun.*, 3, 770, 2012.
- [4.4] D.-H. Ko, J. R. Tumbleston, A. Gadisa, M. Aryal, Y. Liu, R. Lopez, E. T. J. Samulski, *Mater. Chem.*, 21, 16293, 2011.
- [4.5] S. Mokkaḡpati, K. R. Catchpole, *Journ. Appl. Phys.*, 112, 101101, 2012.
- [4.6] H. A. Atwater, A. Polman, *Nat. Mater.*, 9, 205, 2010.
- [4.7] K. R. Catchpole, S. Mokkaḡpati, F. Beck, E.-C. Wang, A. McKinley, A. Basch, J. Lee, *MRS Bulletin*, 36, 461, 2011.
- [4.8] E. Stratakis, E. Kymakis, *Mater. Today*, 16, 133, 2013.
- [4.9] J.-L. Wu, F.-C. Chen, Y.-S. Hsiao, F.-C. Chien, P. Chen, C.-H. Kuo, M. H. Huang, C.-S. Hsu, *ACS Nano*, 5, 959, 2011.
- [4.10] D. H. Wang, K. H. Park, J. H. Seo, J. Seifert, J. H. Jeon, J. K. Kim, J. H. Park, O. O. Park, A. J. Heeger, *Adv. Energy Mater.*, 1, 766, 2011.
- [4.11] X. Li, W. C. H. Choy, L. Huo, F. Xie, W. E. I. Sha, B. Ding, X. Guo, Y. Li, J. Hou, J. You, Y. Yang, *Adv. Mater.*, 24, 3046, 2012.
- [4.12] S. Shahin, P. Gangopadhyay, R. A. Norwood, *Appl. Phys. Lett.*, 101, 053109, 2012.
- [4.13] N. Kalfagiannis, P. Karagiannidis, C. Pitsalidis, N. Panagiotopoulos, C. Gravalidis, S. Kassavetis, P. Patsalas, S. Logothetidis, *Solar Energy Materials and Solar Cells*, 104, 165, 2012.

- [4.14] M. Stavytska-Barba, M. Salvador, A. Kulkarni, D. S. Ginger, A. M. Kelley, *Journ. of Phys. Chem. C*, 115, 20788, 2011.
- [4.15] B. Paci, G. D. Spyropoulos, A. Generosi, D. Bailo, V. R. Albertini, E. Stratakis, E. Kymakis, *Advanced Functional Materials*, 21, 3573, 2011.
- [4.16] F.-C. Chen, J.-L. Wu, C.-L. Lee, Y. Hong, C.-H. Kuo, M. H. Huang, *Appl. Phys. Lett.*, 95, 013305, 2009.
- [4.17] S.-W. Baek, J. Noh, C.-H. Lee, B. Kim, M.-K. Seo, J.-Y. Lee, *Scientific Rep.*, 3, 1726, 2013.
- [4.18] V. Janković, Y. M. Yang, J. You, L. Dou, Y. Liu, P. Cheung, J. P. Chang, and Y. Yang, *ACS Nano*, 7, 3815, 2013.
- [4.19] G. Kakavelakis, E. Stratakis, E. Kymakis, *RSC Adv.*, 3, 16288, 2013.
- [4.20] E. Stratakis, M. M. Stylianakis, E. Koudoumasa, E. Kymakis, *Nanoscale*, 5, 4144, 2013.
- [4.21] P. Spinelli, M. Verschuuren, A. Polman, *Nature Commun.*, 3, 692, 2012.
- [4.22] B. Rolly, B. Stout, N. Bonod, *Opt. Express*, 20, 20376, 2012.
- [4.23] H. Mertens, A. Polman, *Journ. Appl. Phys.*, 105, 044302, 2009.
- [4.24] Y. Akimov, W. Koh, K. Ostrikov, *Opt. Express*, 17, 10195, 2009.
- [4.25] E. Castanie, R. Pierrat, R. Carminati, *Intern. J. Opt.*, 2012, 452047, 2012.
- [4.26] L. Novotny, B. Hecht, *Principles of Nano-Optics*; Cambridge University Press, 2006.
- [4.27] S. Enoch, N. Bonod, "Plasmonics: From basics to more advanced topics", Springer Berlin Heidelberg, 2012.
- [4.28] M. P. Busson, B. Rolly, B. Stout, N. Bonod, S. Bidault, *Nat. Commun.*, 3, 962, 2012.
- [4.29] P. Nordlander, C. Oubre, E. Prodan, K. Li, M. Stockman, *Nano Lett.*, 4, 899, 2004.

- [4.30] B. Rolly, B. Stout, N. Bonod, *Phys. Rev. B*, 84, 125420, 2011.
- [4.31] P. Olk, J. Renger, M. T. Wenzel, L. M. Eng, *Nano Lett.* 8, 1174, 2008.
- [4.32] E. Palik, G. Ghosh, *Handbook of optical constants of solids*, Academic Press, Boston, 1998.
- [4.33] A. Aubry, D. Y. Lei, S. A. Maier, J. B. Pendry, *Phys. Rev. Lett.*, 105, 233901, 2010.
- [4.34] G. Chen, Y. Wang, L. H. Tan, M. Yang, L. S. Tan, Y. Chen, H. Chen, *J. Am. Chem. Soc.*, 131, 4218, 2009.
- [4.35] G. D. Spyropoulos, M. M. Stylianakis, E. Stratakis, E. Kymakis, *Appl. Phys. Lett.*, 100, 213904, 2012.
- [4.36] F.-X. Xie, W. C. H. Choy, C. C. D. Wang, W. E. I. Sha, D. D. S. Fung, *Appl. Phys. Lett.*, 99, 153304, 2011.
- [4.37] S.-S. Kim, S.-I. Na, J. Jo, D.-Y. Kim, Y.-C. Nah, *Appl. Phys. Lett.*, 93, 073307, 2008.
- [4.38] S. Bidault, A. Polman, *Intern. J. Opt.*, 2012, 387274, 2012.
- [4.39] B. Paci, A. Generosi, V. R. Albertini, G. D. Spyropoulos, E. Stratakis, E. Kymakis, *Nanoscale*, 4, 7452, 2012.
- [4.40] E. D. Gaspera, M. Karg, J. Baldauf, J. Jasieniak, G. Maggioni, A. Martucci, *Langmuir*, 27, 13739, 2011.
- [4.41] Z. Hu, J. Zhang, Y. Zhu, *Appl. Phys. Lett.*, 102, 043307, 2013.
- [4.42] R. Betancur, A. Martínez-Otero, X. Elias, P. Romero-Gomez, S. Colodrero, H. Miguez, J. Martorell, *Solar Energy Materials and Solar Cells*, 104, 87–91, 2012.
- [4.43] S. D. Burnside, V. Shklover, C. Barbé, P. Comte, F. Arendse, K. Brooks, M. Grätzel, *Chemistry of materials*, 10, 2419–2425, 1998.
- [4.44] S. Colodrero, A. Mihi, L. Häggman, M. Ocana, G. Boschloo, A. Hagfeldt, H. Miguez, *Adv. Mater.*, 21, 764–770, 2009.

- [4.45] P. Romero-Gomez, A. Borrás, A. Barranco, J. P. Espinos, A. R. González-Elipé, *ChemPhysChem*, 12, 191, 2011.
- [4.46] B. Stout, A. Devilez, B. Rolly, N. Bonod, *J. Opt. Soc. Am. B*, 28, 1213, 2011.
- [4.47] Atwater, H. A.; Polman, A. *Nat Mater*, 9, 205–213, 2010.
- [4.48] Catchpole, K. R.; Mokkaṭpati, S.; Beck, F.; Wang, E.-C.; McKinley, A.; Basch, A.; Lee, J. *MRS Bulletin*, 36, 461–467, 2011.
- [4.49] Stratakis, E.; Kymakis, E. *Materials Today*, 16, 133–146, 2013.
- [4.50] Cesario, J.; González, M. U.; Cheylan, S.; Barnes, W. L.; Enoch, S.; Quidant, R. *Opt. Express*, 15, 10533–10539, 2007.
- [4.51] Munday, J. N.; Callahan, D. M.; Atwater, H. A. *Appl. Phys. Lett.*, 100, 121121, 2012.
- [4.52] Yoon, S. M.; Lou, S. J.; Loser, S.; Smith, J.; Chen, L. X.; Facchetti, A.; Marks, T. *Nano Letters*, 12, 6315–6321, 2012.
- [4.53] Martínez-Otero, A.; Elias, X.; Betancur, R.; Martorell, J. *Advanced Optical Materials*, 1, 36–36, 2013.
- [4.54] N.P. Sergeant, A. Hadipour, B. Niesen, D. Cheyṅs, P. Heremans, P. Peumans, B.P. Rand, *Advanced Materials*, 24, 728, 2012.
- [4.55] F. Pastorelli, S. Bidault, J. Martorell and N. Bonod, “Self-assembled plasmonic oligomers for organic photovoltaics” submitted to *Advanced Optical Materials*, accepted, 2013.

## References Chapter 5.

- [5.1] J. Ramallo, “Statement on Silver Lake and Elysian Reservoir Bromate Issue”, Los Angeles Department of Water and Power Communications, 2007.
- [5.2] G. Quesada, D. Rousse, Y. Dutil, M. Badache, S. Hallé, “A comprehensive review of solar facades. Opaque solar facades” *Renewable and Sustainable Energy Reviews*, Volume 16, Issue 5, Pages 2820–2832, 2012.
- [5.3] G. Quesada, D. Rousse, Y. Dutil, M. Badache, S. Hallé, “A comprehensive review of solar facades. Transparent and translucent solar facades”, *Renewable and Sustainable Energy Reviews*, Volume 16, Issue 5, Pages 2643–2651, 2012.
- [5.4] R. Betancur, “Photon control in nano-structured organic photovoltaic materials”, Thesis dissertation, ICFO, 2013.
- [5.5] R. Betancur, P. Romero-Gomez, A. Martinez-Otero, X. Elias, M. Maymó and J. Martorell, accepted in *Nature Photonics*, 2013.
- [5.6] C. Chen, L. Dou, J., W. Chang, G. Li and Y. Yang, *Energy Environ. Sci.*, 6, 2714, 2013.
- [5.7] C.-C. Chueh, S.-C. Chien, H.-L. Yip, J. F. Salinas, C.-Z. Li, K.-S. Chen, F.-C. Chen, W.-C. Chen, A. K.-Y. Jen, *Advanced Energy Materials*, 3, 4, 417–423, 2013.
- [5.8] R. F. Bailey-Salzman, B. P. Rand and S. R. Forrest, *Applied Physics Letters*, 88, 233502, 2006.
- [5.9] G.-M. Ng, E. L. Kietzke, T. Kietzke, L.-W. Tan, P.-K. Liew and F. Zhu, *Applied Physics Letters*, 90, 103505, 2007.
- [5.10] F.-C. Chen, J.-L. Wu, K.-H. Hsieh, W.-C. Chen and S.-W. Lee, *Organic Electronics*, 9, 1132–1135, 2008.

- [5.11] A. Colsmann, A. Puetz, A. Bauer, J. Hanisch, E. Ahlswede, U. Lemmer, *Advanced Energy Materials*, 1, 599–603, 2011.
- [5.12] F. Guo, X. Zhu, K. Forberich, J. Krantz, T. Stubhan, M. Salinas, M. Halik, S. Spallek, B. Butz, E. Spiecker, T. Ameri, N. Li, P. Kubis, D.M. Guldi, G. J. Matt and C. J. Brabec, *Advanced Energy Materials*, 3, 8, 1062–1067, 2013.
- [5.13] Z. Tang, Z. George, Z. Ma, J. Bergqvist, K. Tvingstedt, K. Vandewal, E. Wang, L. M. Andersson, M. R. Andersson, F. Zhang, O. Inganäs, *Advanced Energy Materials*, 2, 12, 1467–1476, 2012.
- [5.14] J. Krantz, T. Stubhan, M. Richter, S. Spallek, I. Litzov, G. J. Matt, E. Spiecker and C. J. Brabec, *Advanced Functional Materials*, 23, 13, 1711–1717, 2013.
- [5.15] C. Tao, G. Xie, C. Liu, X. Zhang, W. Dong, F. Meng, X. Kong, L. Shen, S. Ruan and W. Chen, *Applied Physics Letters*, 95, 053303, 2009.
- [5.16] L. Shen, Y. Xu, F. Meng, F. Li, S. Ruan, W. Chen, *Organic Electronics*, 12, 1223–1226, 2011.
- [5.17] C. Tao, G. Xie, F. Meng, S. Ruan and W. Chen, *The Journal of Physical Chemistry C*, 115, 12611–12615, 2011.
- [5.18] T. Winkler, H. Schmidta, H. Flüggea, F. Nikolayzika, I. Baumanna, S. Schmalea, T. Weimannc, P. Hinzec, H.-H. Johannesaa, T. Rabea, S. Hamwia, T. Riedlb, W. Kowalskya, *Organic Electronics*, 12, 1612–1618, 2011.
- [5.19] Z. Liu, J. Li, Z.-H. Sun, G. Tai, S.-P. Lau and F. Yan, *ACS nano*, 6, 810–818, 2012.
- [5.20] J. Huang, G. Li, and Y. Yang, *Advanced Materials*, 20, 415–419, 2008.
- [5.21] J.-Y. Lee, S. T. Connor, Y. Cui and P. Peumans, *Nano letters*, 10, 1276–1279, 2010.
- [5.22] R. R. Lunt and V. Bulovic, *Applied Physics Letters*, 98, 113305, 2011.
- [5.23] N. P. Sergeant, A. Hadipour, B. Niesen, D. Cheyns, P. Heremans, P. Peumans and B. P. Rand, *Advanced Materials*, 24, 728-732, 2012.



- [5.24] H. Jin , C. Tao, M. Velusamy, M. Aljada, Y. Zhang, M. Hamsch, P. L. Burn and P. Meredith, *Advanced Materials*, 24, 2572–2577, 2012.
- [5.25] D.S. Ghosh, R. Betancur, T.L. Chen, V. Pruneri and J. Martorell, *Sol. Energy Mat. Sol. Cells*, 95, 4, 1228-1231, 2011.
- [5.26] N. Formica, D. S. Ghosh, T. L. Chen, C. Eickhoff, I. Bruder, V. Pruneri, *Sol. Energy Mat. Sol. Cells*, 107, 63-68, 2012.
- [5.27] F.-C. Chen, J.-L. Wu, K.-H. Hsieh, W.-C. Chen, and S.-W. Lee, *Organic Electronics*, 9, 1132–1135, 2008.
- [5.28] R. Betancur, A. Martínez-Otero, X. Elias, P. Romero-Gómez, S. Colodrero, Hernán Miguez, and J. Martorell, *Sol. Energy Mat. Sol. Cells*, 104, 87–91, 2012.
- [5.29] J. M. García-Martín, R. Alvarez, P. Romero-Gómez, A. Cebollada, and A. Palmero, *Applied Physics Letters*, 97, 173103, 2010.
- [5.30] R. Alvarez, P. Romero-Gomez, J. Gil-Rostra, J. Cotrino, F. Yubero, *J. Appl. Phys*, 108, 064316, 2010.
- [5.31] R. Alvarez, P. Romero-Gomez, J. Gil-Rostra, J. Cotrino, F. Yubero, A. R. Gonzalez-Elipe and A. Palmero, *Phys. Status Solidi*, A210, 4, 796–801, 2013.
- [5.32] N. P. Sergeant, A. Hadipour, B. Niesen, D. Cheyns, P. Heremans, P. Peumans and B.P. Rand, *Advanced Materials*, 24, 728-732, 2012.
- [5.33] F. Pastorelli, P. Romero Gomez, R. Betancur, A. Martinez-Otero, N. Bonod and J. Martorell, “Enhanced Light Harvesting in Semitransparent Organic Solar Cells Using an Optical Cavity Configuration”, in preparation, 2013.